Structure, function and mechanism of the alternative oxidases

Luke Young

September 2013

Submitted in partial fulfilment towards the requirements for the degree of Doctor of Philosophy (DPhil)

I hereby declare that this thesis has not been and will not be, submitted in whole or in part to another University for the award of any other degree.

Signature

.....

University of Sussex

Luke Young

Submitted for the degree of Doctor of philosophy

Structure function and mechanism of the alternative oxidases

Summary

The alternative oxidase (AOX) is the terminal protein in the alternative oxidation pathway found in plants, fungi and some protozoa. One of the more prominent protozoa that contain AOX within the bloodstream form is *Trypanosoma brucei*, the causative agent of human African trypanosomiasis (HAT), in which the parasite has demonstrated to be totally dependent upon the protein for continued respiration. Given the lack of AOX in mammalian cells, the protein represents an attractive chemotherapeutic target for trypanosidal activity.

Ascofuranone is a known inhibitor of AOX, but its complex synthesis precludes it from industrial production. To this end colletochlorin B, an analogue of ascofuranone, was synthesised and its inhibitory efficacy against AOX examined. IC_{50} values obtained demonstrate that removal of the problematic furanone ring does not reduce inhibitor efficacy to a large degree. Derivatives of colletochlorin B were synthesised to assess the importance of structural moieties present. The compounds were also tested against the cytochrome bc_1 complex, an important respiratory chain complex, and compared with known fungicides. Using these compounds assays against fungal species has yielded promising results for the use of colletochlorin B as a lead fungicide.

Recombinant wild type trypanosomal alternative oxidase (TAO) and *Sauromatum guttatum* alternative oxidase (SgAOX) have been expressed in *E.coli.* in addition to a number of mutants. Respiratory activities of these mutants were measured in order to assess the importance of highly conserved amino acids, with all mutants showing a decline in specific activity. Three of the mutants generated were also shown to affect the apparent affinity for oxygen, the implications of which are discussed.

Recent crystallisation of TAO has enabled a more detailed examination of the structure of all AOXs. Work is presented relating structure to the overall function of the protein, taking into account conservation throughout the entire AOX family. Comparisons to other di-iron proteins revealed a conserved His-Asp-Tryp motif that could facilitate proton coupled electron transport. A full catalytic cycle based on these findings has been postulated.

Table of Contents

Abbreviations used

Abbreviation	
AA	Antimycin A
ADP	Adenosine diphosphate
AOX	Alternative oxidase
ATP	Adenosine triphosphate
BSA	Bovine serum albumin
CCCP	Carbonyl cyanide *m*-chlorophenyl hydrazone
DBU	1,8-Diazabicycloundec-7-ene
DHAP	Dihydroxyacetone phosphate
ETC	Electron transport chain
FAD/$FADH_2$	flavin adenine dinucleotide (ox/red)
G3P	Glyceraldehyde 3-phosphate
HAT	Human African trypanasomiasis
HMPA	Hexamethylphosphoramide
IC_{50}	Half maximal inhibitory concenctration
IMS	Inter membrane space
IPTG	Isopropyl β-D-1-thiogalactopyranoside,
MMO	Methane monooxygenase
NADH/NAD+	Nicotinamide adenine dinucleotide (ox/red)
NAP(P)H	Nicotinamide adenine dinucleotide phosphate
OG	Octyl gallate
PCET	Proton coupled electron transport
QH2 / Q	Quinol/Quinone
RBR	Rubrerythrin
RNR	Ribonucleotide reductase
ROS	Reactive oxygen species
SEM	2-(Trimethylsilyl)ethoxymethyl chloride
SHAM	Salcylic hydroxamic acid
TAO	Trypanosomal alternative oxidase
TBAF	Tetra-*n*-butylammonium fluoride
tBuLi	Tert- butyllitium
TLC	Thin layer chromatography

Acknowledgements

First and foremost I would like to thank my two supervisors, Professor Anthony Moore and Dr Hans Streicher, for giving me the opportunity to undertake a PhD project. The guidance and support provided has been invaluable, and the project itself has been extremely interesting project to work on.

Many thanks are extended to Mary Albury, Catherine Elliott and Mathew Stanley for all their help in teaching me the lab techniques required for this thesis (and the reassurances that there were no stupid questions!). I would also like to thank Julia Shearman and Benjamin May for all their help (but more importantly keeping me extremely well supplied with coffee).

Thank you to Professor Kita and colleagues (University of Tokyo) for providing access to the crystal structures used within this thesis. My gratitude's are also extended to Dr. Brigitte Meunier (Centre de Génétique Moléculaire) for kindly providing samples of cytochrome bc_1 mutants, and Dr. Shane Wilkinson (Queen Mary) for assaying the inhibitor samples against the trypanosomes.

A special thank you to all of my friends and colleagues that I have made during my time at Sussex, you have made this an enjoyable experience.

Last but not least, I would like to thank Amy Saunders for all the help and support she has given me over the past 4 years.

1 Introduction

1.1 Respiration overview

The utilisation of energy from macromolecules is a necessity for all life forms. While the amount of energy released from large molecules would be excessive for cellular processes, the energy is effectively stored and quantised into smaller packets in the form of ATP, allowing for biological reactions to be modulated around a common energy source [1]. The majority of cellular ATP is generated via the breakdown of carbohydrates; under aerobic conditions glucose is broken down via the glycolytic process within the cytosol of the cell, generating 2 ATP, 2 pyruvate and 2 NADH [2].

The pyruvate generated is transported into the mitochondrial matrix to form acetyl-CoA, which feeds into the Kreb's cycle. Condensation of acetyl-CoA with oxaloacetate forms citrate, which, via a series of enzymatic reactions regenerates oxalacetate, forming 3 molecules of NADH in the process. NADH and succinate, an intermediate formed during the Krebs cycle, are used as reducing equivalents for the electron transport chain (ETC).

For each molecule of glucose present, 2 molecules of ATP are generated during the glycolytic process, alongside 10 molecules of NADH. The oxidation of NADH and succinate within the ETC gives a theoretical yield of 36 molecules of ATP from the respiratory chain per glycolytic turnover, but observable yields are ~30 per cycle [3], with losses being attributed to proton leakage across the membrane [4].

1.2 Electron transport chain

The ETC consists of enzyme complexes associated with the inner mitochondrial membrane that ultimately facilitate the transfer of electrons from reducing equivalents to oxygen via a series of thermodynamically favourable reactions. The free energy generated is used to translocate protons from the matrix into the intermembrane space (IMS), generating a proton gradient across the membrane, effectively storing the energy as a chemiosmotic potential. This potential is subsequently used to couple ADP with a phosphate group to form ATP within ATP synthase, an otherwise energetically unfavourable reaction [5].

Figure 1-1 contains the currently accepted electron transport chain and crystal structures of each complex accrued to date. While complexes I-V are ubiquitous throughout higher mitochondria, plant mitochondria also contain external and internal NADH dehydrogenases, often referred to as rotenone insensitive dehydrogenases due to their effective bypassing of inhibition of complex I as an entry point for electrons from NADH. A brief overview of the main complexes within the electron transport chain has been included to give context to the discussion with respect to AOX.

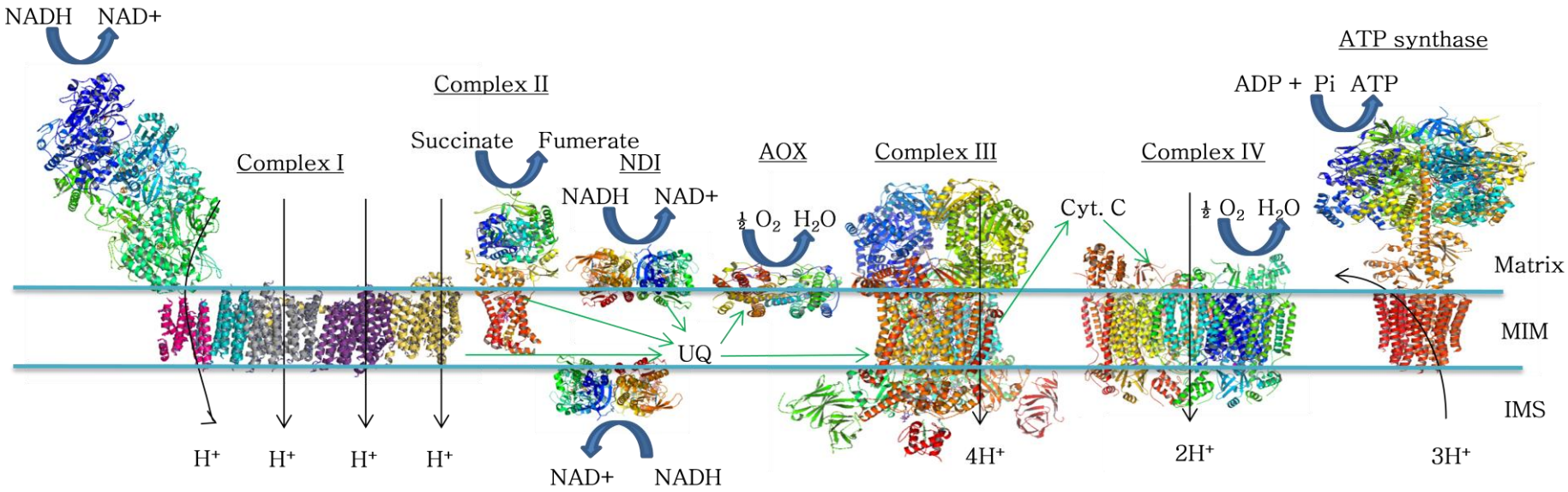

Figure 1-1:- Crystal structures of the components of the electron transport chain within plant mitochondria. internal NADH dehydrogenase (NDI), external NADH dehydrogenase (NDI structure used due to no crystal structure available to date) and AOX are not present in the mammalian ETC. Green arrows depict direction of electron flow to and from the quinone pool (UQ) and cytochrome C (Cyt.C). Black arrows represent proton pumping across the membrane. Crystal structures used are as follows : Complex I (PDB:3MPS [6]) complex II (PDB:3VRS[7]) complex III (PDB:3H1J [8]), complex IV (PDB:1OCO [9]) NDI (PDB:4GAP [10]) AOX (PDB:3VV9 [11]) ATP synthase (F_0 (PDB(1C17 [12]), F_i(PDB:1E79 [13])) The Stator has been omitted from ATP synthase, but crystal structures are available (PDB :2A7U [14]). MIM and IMS refer to the mitochondrial inner membrane and intermembrane space respectively. Adapted with permission from [15]

Complex I

$$NADH/H^+ + Q + 4H^+_{matrix} \rightarrow NAD^+ + QH_2 + 4H^+_{IMS}$$

NADH dehydrogenase (complex I) utilised the NADH formed during the Krebs cycle to reduce an equivalent of quinone to quinol. This multi-protein complex spans the inner mitochondrial membrane, allowing for the translocation of 4 protons from the mitochondrial matrix into the intermembrane space in the process, generating a proton gradient. The overall structure of the protein is L-shaped, consisting of a hydrophilic arm within the mitochondrial matrix, and a hydrophobic membrane spanning region.

Initial reaction with NADH occurs on the hydrophilic arm, with transfer of electrons and protons to flavin mononucleotide (FMN), a prosthetic group within complex I. The electrons are then transferred via a series of iron-sulphur clusters into the protein core, where they are transferred to quinone to form quinol. The electron flow from FMN to the quinol is coupled to proton translocation within the hydrophobic domain [16], with examination of the crystal structure of the hydrophobic stretch indicating that proton translocation is triggered by protein reduction, with a proton transferred through each domain sequentially from the core [17].

Extensive reviews covering facets of complex I are available [18], including high resolution crystal structures of the hydrophilic arm [19], the membrane spanning domain [17] and the mechanistic insights that have been gained from the aforementioned structures [20, 21].

Complex II

$$Succinate + Q \rightarrow Fumarate + QH_2$$

Succinate dehydrogenase (complex II) fulfils a similar role to complex I with respect to the electron transport chain (ETC), in so much as it acts as an independant entry point into the ETC. Succinate is generated during the Krebs cycle, and reduction to fumarate couples the cycle into the ETC. Unlike complex I, complex II does not

shuttle protons across the membrane, and therefore does not aid in generation of a proton gradient.

Complex II is made of 4 distinct proteins, 2 hydrophilic subunits on the matrix side (SDHA and SDHB, that contain the FAD cofactor and iron sulphur clusters respectively), and 2 hydrophobic subunits (SDHC and SDHD) that span the inner mitochondrial membrane. Succinate reacts at SDHA, transferring protons and electrons to oxidase FAD to $FADH_2$. The electrons are then transferred via a series of iron-sulphur clusters within SDHB towards the Fe_3S_4 cluster, where they are transferred sequentially onto ubiquinone bound in the cleft between SDHC and SDHD. A comprehensive review by Iverson on the catalytic mechanism of complex II is available [22].

Quinol and the quinone pool

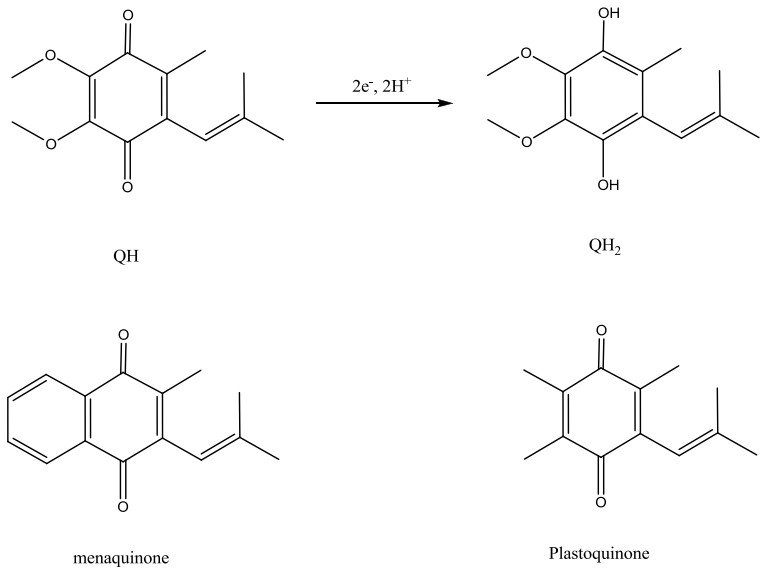

Figure 1-2:- Quinones used throughout the ETC. The length of the isoprene tail can be increased to 10 units, with Q_1H_2 depicted. Menaquinone is favoured by anerobes, and plastoquinone is the electron carrier in chloroplasts.

Quinols within the ETC act as mobile proton and electron carriers, transporting electrons from complexes I and II to complex III. The hydrophobic nature of the isoprenoid tail makes the compound extremely lipophilic, leading to an accumulation

within the phospholipid bilayer commonly referred to as the quinone pool. The identity of the quinone is dependent upon the membrane in which it is found; quinone is preferred in aerobes, with menaquinones being the preferential electron carrier under anaerobic conditions. A further example is found within chloroplasts, where plastoquinone is the preferred electron carrier.

Complex III

$$QH_2 + 2 \text{ cytochrome } c_{ox} + 2H^+_{mat} \rightarrow Q + 2 \text{ cytochrome } c_{red} + 4H^+_{IMS}$$

The overall function of complex III is facilitation of electron transfer from quinol onto cytochrome c, a mobile protein found within the IMS that shuttles electrons to complex IV. As with complex I, complex III pumps protons across the membrane, leading to an increase in proton gradient.

While the above equation for the overall reaction within complex III implies the use of only 1 molecule of quinol, there are in fact 3 separate molecules of quinol/quinone involved in the "Q" cycle originally proposed by Mitchell [5] .Reviews of the structure function relationship with respect to the Q cycle are available [23, 24]. Quinol initially binds at the Q_o site in cytochrome b, where it transfers an electron to the Fe_2S_2 cluster, losing two protons in the process (which are subsequently transferred into the IMS) leaving a semiquinone radical. This electron is subsequently shuttled into the haem within the cytochrome c_1 subunit, where it is used to reduce an equivalent of cytochrome c. The second electron from the semiquinone is transferred via a series of haem groups to a quinone molecule bound within the Q_i site, generating a semiquinone and releasing the initial quinol as a quinone. This process is then repeated, converting the semiquinone bound at the Q_i site to a quinol and generating a second equivalent of reduced cytochrome c.

Full reviews on complex III are available, alongside more specific structural modelling of the interaction between the Q_o and Q_i sites [25] and examination of the electron transfer via structural mutations [26].

Complex IV

$$4 \text{ cytochrome } c_{red} + 8H^{+}_{mat} + O_2 \rightarrow 4 \text{ cytochrome } c_{ox} + 2H_2O + 4H^{+}_{IMS}$$

Complex IV is the terminal electron acceptor in the ETC, using the electrons provided by cytochrome c to reduce oxygen through to water, while pumping protons across the membrane. The overall structure can be broken down into two distinct subunits, with subunit I containing the oxygen binding Fe-Cu centre, and subunit II containing CuA, a binuclear copper centre. Cytochrome c binds to CuA, with electron transfer towards the Fe-Cu core facilitated via a proximal haem group.

The oxygen reduction cycle is well studied [27, 28], with a resting $Fe^{2+}Cu^{+}$ state rapidly reducing oxygen via homolytic cleavage to form an Fe^{4+} =O Cu^{2+}-OH core, and the generation of a tyrosyl radical in close proximity. Subsequent transfer of electrons from cytochrome C and protons from the matrix via well defined proton channels allow the protein to return to its fully reduced state. A full review on the catalytic cycle is available [29].

Alternative pathway

The alternative oxidase (AOX) is the terminal protein in the alternative oxidation pathway within the mitochondria of a variety of plant, fungi and protozoa. The pathway is often referred to the cyanide resistant pathway, due to its early discovery of cyanide resistant respiratory activity in plant mitochondria [30]. The AOX is also resistant to nitric oxide [31], a potent inhibitor of complex IV. The latter is important for both fungi and bacteria, as it gives resistance to typical host immune responses of NO release upon cell death.

The pathway branches from the regular ETC at the ubiquinone pool [32, 33], effectively circumventing complexes III and IV to directly reduce of oxygen to water [34], oxidising 2 equivalents of quinol in the process. This pathway is less energy efficient, with no proton translocation occurring as an energy sink [35], with the excess energy generated instead dissipated as heat. The utilisation of external and

internal NADH dehydrogenase within plants [36] and succinate dehydrogenase allows the alternative pathway to be completely independent of proton pumping.

The separation of the alternative pathway from the cyctochrome c dependant pathway is made apparent from the complex association within supercomplexes. Supercomplexes are an aggregation of complexes I III and IV, arranged in close proximity to increase efficiency due to reduction of the diffusional constant for electron carriers. While supercomplexes form within plant mitochondria, it has been demonstrated that the alternative oxidase is not associated [37]. The lack of association of complex II, external NADH dehydrogenase and AOX has been attributed to a partitioning effect, creating a distinct separation between the two pathways. Further evidence can be found from 2-D gel electrophoresis experiments performed on *Arum maculatum* spadicies, where the authors were unable to locate complex I that was not part of a supercomplex [38]. Similar experiments performed revealed a smear that was attributed to AOX, believed to be indicative of an arrangement of numerous AOX proteins rather than an aggregation of monomers that had associated under electrophoretic conditions [39].

Comprehensive reviews are available of AOX covering structural considerations [15] and homeostatic roles [40] . Up-to-date reviews of the organisation and regulation of complexes within the plant ETC are also available [41] .

1.3 Functions of the alternative oxidase

1.3.1 Thermogenesis

The functions of the alternative oxidase are diverse and dependent upon the nature of the tissue in which they are found. Whilst the protein is found in all plant mitochondria [42], it is found in especially high concentrations within the spadix of plants from the Araceae family, such as *Sauromatum guttatum* and *Amorphophalus titanum*. Such tissues are thermogenic, raising the temperature of the spadix above local ambient temperatures. The heat generated is used to volatilises primary amines, with the intention of attracting flies for pollination purposes [43, 44], or alternatively to melt the surrounding ice during germination in skunk cabbage. Increased rates in mitochondrial respiration have been demonstrated to directly correlate to the increased levels of heat generated by thermogenic plant tissue [45], with AOX being responsible for 90% of respiratory flux during heating [46]. Thermogenesis has also been demonstrated to coincide with a 10-fold increase in AOX expression levels within the sacred lotus [47]. The uncoupled nature of the alternative pathway from proton translocation and hence ATP generation leads to the excess energy being used to generate heat.

1.3.2 Homeostasis

The expression of AOX from *Sauromatum guttatum* into *Schizosaccharomyces pombe* demonstrates that AOX is energy inefficient relative to the cytochrome c dependant pathway, reducing growth levels when compared to wild type [48]. One of the major proposed roles for AOX is for mitochondrial homeostasis [40], with phylogenetic analysis highlighting its position with other di-iron oxygen scavengers [49]. Expression of AOX is increased at times when the regular ETC is under stress, such as inhibition of complexes downstream of the quinone pool by fungicides [50], and during aging in potato tuber [51].

Reactive oxygen species (ROS), such as superoxides and peroxides, are detrimental to cell longevity and have been implicated in both apoptosis and senescence.A majority of ROS are generated within the mitochondria [52, 53], via single electron reduction of oxygen to a superoxide species. Complex I is a major source of ROS [54] within mitochondria during reverse electron transport caused by a highly reduced quinone pool [55-57] due to high succinate dependant respiration. A highly reduced quinone pool induces inhibition of complex I, generating a high NADH/NAD+ ratio which in turn generates high levels of reduced FMN, thought to be one of the main sources of superoxide production. Inhibition of complex I with rotenone at the quinone site generated increased levels of superoxide[58], effectively mimicking inhibition of complex I via a highly reduced quinone pool. Expression of AOX therefore reduces superoxide levels due to aiding oxidation of the quinone pool[59], allowing for more optimal throughput of the ETC by effectively acting as an energy overflow. Optimal V_{max} for partitioning into the alternative pathway has been shown to require a high redox potential with respect to the quinone pool, with the pathway not being utilised until the quinol to quinone ratio is greater than 0.4 [60, 61].

The second homestatic role for AOX is to lower the effective concentration of oxygen within the mitochondria. There is a direct correlation between $[O_2]$ and $[O_2^{\bullet-}]$ at concentrations lower than 5 µM [62], approximately the concentration found within fully functional mitochondria. AOX is able to act as an effective oxygen scavenger, with its relatively low Km for oxygen (12.3 µM [63] in mung bean and 13.2 µM in soybean [64] alternative oxidases, compared to 0.1 µM for cytochrome c oxidase [65]) allowing it to reduce the levels of oxygen at high concentrations, but not act as a preferential binding site over the regular ETC proteins under optimal conditions.

Mitochondria contain a number of mechanisms to prevent ROS becoming problematic within the cells.For example, protein based systems such as superoxide dismutase convert superoxide through to hydrogen peroxide [66], which can then safely be converted to water via glutathione peroxidases. The expression of AOX is a preventative measure, lowering the cumulative causative effects that contribute to the production of ROS. An increase in hydrogen peroxide levels have been shown to induce AOX expression [67], suggesting it plays a secondary role to regular ROS

scavengers until the peroxidases are saturated. Indeed, it has been shown that inhibition of AOX using propyl gallate or SHAM in mitochondria already expressing the protein leads to an increase in peroxide levels [68].

The plant AOX is activated by pyruvate [69], with addition of pyruvate increasing the V_{max} [70],whilst not affecting the affinity for quinol From a homeostatic perspective, an increase in pyruvate levels would indicate an increase in glycolysis over the ability for the citric acid cycle to maintain turnover, either due to inhibition of complexes further down the cycle, or a high NADH/NAD+ ratio preventing the conversion of pyruvate to actyl-CoA. Use of pyruvate as a post-translational regulatory mechanism acts as an effective feed-forward mechanism; stimulation of the AOX via pyruvate leads to a reduction of the quinone pool, which in turn allows for increased activity of complex I and a decrease in the NADH/NAD+ ratio.

1.4 Trypanosomes

Trypanosomes (specifically *T. b. rhodensiense* and *T. b. gambiense*) are the causative agent of human African trypanosomiasis (HAT), with *T. vivax* responsible for Nangana in livestock. HAT was reported in 1997 to affect 450,000 people in sub-Saharan African [71], but more recent figures have shown a decline in infection to ~30,000 [72]. The disease is fatal if left untreated.

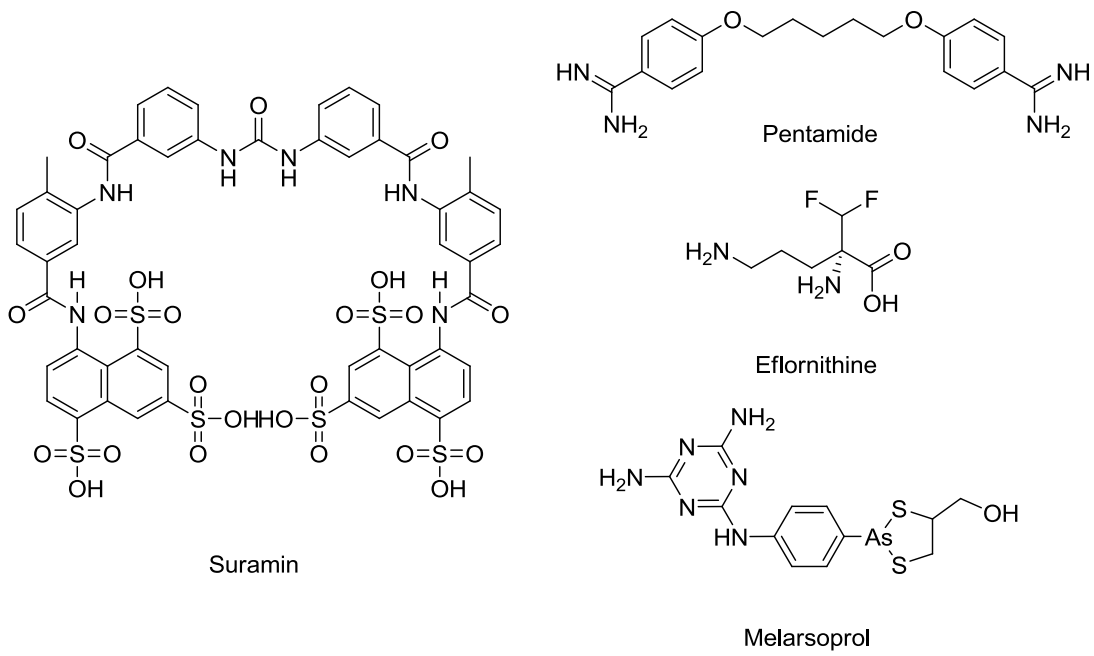

Figure 1-3:- Chemical structures of drugs used to treat HAT.

The transfer of the parasite via the tsetse fly vector makes preventative efforts ineffective, and use of variable surface glycoproteins (VSG) by trypanosomes [73] enable evasion of the hosts immune response. Current treatments for the disease result in undesirable side-effects or only prove effective during the early stages of infection. Suramin and pentamide were some of the earlier treatments developed, and are only effective in early stages of infection due to their inability to cross the blood brain barrier [74]. Melarsaprol is effective in late stages of the disease, but causes reactive encephalopathy in 19% of patients [75]. Eflornithine is the most recent to be developed [76], targeting the ornithine decaraboxylase, preventing cell division within the trypanosomes [77]. The compound is less problematic within human tissue, due to its higher rate of metabolism is mammalian cells preventing the toxic build-up that kills trypanosomes. Application of all treatments to date necessitates trained professionals, requiring intravenous therapy over the course of 12 days [78]. The most recent and effective treatment to be developed, a Nifurtimox-eflornithine combination therapy (NECT), has an improved application over previous drugs, only requiring treatment over the course of 7 days [79].

The bloodstream form of the trypanosome downregulates the cytochrome pathway [80] leaving it dependent upon glycolysis for energy production [81]. The

Trypanosomal alternative oxidase (TAO) is used to generate quinone, which in turn is utilised to convert G-3-P to DHAP, allowing for regeneration of the cytosolic NAD+ necessary for continued glycolysis [82]. Given the dependant nature of trypanosomes on TAO for ATP generation (ref), TAO has been identified as a chemotherapeutic target for treatment of HAT [83].

1.5 Inhibition of AOX

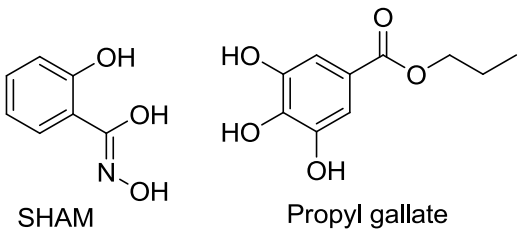

Figure 1-4 : Chemical structures of SHAM and propyl-gallate, known inhibitors of AOX.

Figure 1-4 shows the chemical structures of Salicylic hydroxamic acid (SHAM) and propyl gallate, the more studied inhibitors of AOX. SHAM is the least potent of the two, with an IC_{50} of 40µM in *Arabidopsis thaliana* [84] and a Ki value of 53 µM in purified *A. maculatum* mitochondria [85]. Initial reports of SHAM inhibition suggested that inhibition was due to chelation of the iron centre, but competitive inhibition with respect to quinol [85] would suggest this not to be the case. Assays have demonstrated that while inhibition is specific to AOX with respect to the ETC [86], it is non-specific within cellular tissues, inhibiting tyrosinase and peroxidase [87].

Attempts to treat trypanosomiasis within the mouse [88] and goat [89] models with SHAM proved unsuccessful. Addition of glycerol increased activity against trypanosomes by inhibition of the glycerol production pathway [90], but the SHAM concentrations necessary were above toxicity levels, causing a 44% mortality rate [91] . The lack of ability to remove trypanosomes from the host was largely attributed to the low solubility of the compound, lowering bioavailability in the tissues where it was required.

A number of structural analogues were tested by Grady and colleagues to find improved inhibitors. Initial screening against trypanosomes [92] revealed a number of potential scaffolds, with the paraalkyloxybenzhydroxamic acids being taken further [93]. Investigation into this system revealed that an increased chain length improves inhibitory proprieties of the compounds, likely due to an increase in lipophilic character, but was detrimental to the inhibition profile due to a decrease in solubility. It was also determined that the acidity of the hydroxamic moiety was not a contributing factor, and that addition of an electron withdrawing group para to the hydroxamic acid improved inhibition.

Esters of 3,4-dihydroxybenzoic acid also proved to be potent inhibitors of AOX, with compounds being 400 times more effective then SHAM [94], but unfortunately retained the same solubility issues. Replacement of the ester with an amide bond improved solubility of the compound while retaining efficacy at higher chain lengths; such compounds were able to cure infection in 17 out of 19 mice when used in conjunction with glycerol, with fatalities in the remaining 2 [95]. It is also worth noting that an increase in chain length also altered the mode of inhibition; a chain length up to 4 demonstrated competitive inhibition with respect to the quinol substrate, but larger than 10 resulted in non-competitive inhibition [96].Alternative attempts to improve on the issues faced by SHAM were made by introduction of both a prenyl chain and a carbohydrate to improve solubility. While these additions did improve the Ki value of the compound, they were detrimental to the overall inhibition profile [97].

Gallates, esters of 3,4,5-trihydroxybenzoic acid, are also a family of known AOX inhibitors [98] with a Ki of 2 μM [94]. A structure function study of gallate inhibition against mung bean AOX demonstrated that an increase in tail size increased the binding efficacy towards the protein, and that hydroxide functionality para to the ester was necessary for inhibition [99].

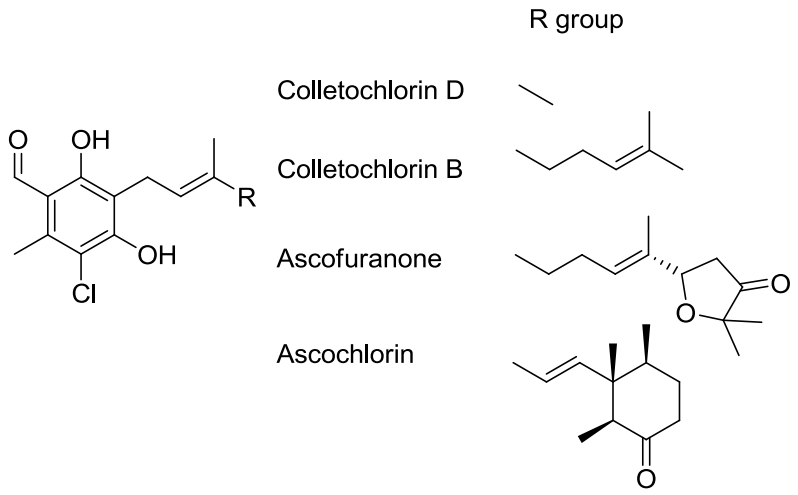

Figure1-5:- Natural products isolated from *Ascochyta viciae* and *Cylindrocarpon sp.*

Ascofuranone belongs to a family of compounds from the fungus *Ascochyta viciae* [100, 101] which includes ascochlorin (Figure1-5). Such compounds received keen interest due to their nature as antibiotics with hypolipidemic activity [102, 103] and antitumor activity [104, 105]. Derivatives of ascochlorin, specifically the AS-6 (-OCH_2COOH at the position 4), have shown improved insulin responses in obese mice [106, 107]. More recent studies have indicated that ascochlorin confers antifungal activity against *Candida albicans*, the causative agent of thrush [108]. It is thought that the colletochlorins are likely an intermediate along the biosynthetic pathway to ascochlorin [109].

Ascofuranone is one of the more potent inhibitors of AOX, with an IC_{50} of 4 nM. The compound has trypanosidal activity both *in vitro* [110] and *in vivo* [111, 112], with successful treatment within the mouse model demonstrating the specificity of the compound. In contrast, Ascochlorin has been shown to be a potent inhibitor of the bc_1 complex [113], binding at both the Qo and Qi sites.

Investigation into the structure of ascofuranone and the Ilicicolin family revealed that the furanone ring is not necessary for binding, and that removal of chlorine reduces the binding affinity to AOX [114]. One of the more interesting effects of chlorine was towards the cytochrome b_o and *bd* complexes; removal of chlorine increased inhibition towards the b_d complex, whilst reducing efficacy towards the b_o

complex. More recent structure-function analysis of ascofuranone [115] confirmed that the furanone ring is not necessary for inhibition, and that only the first isoprene unit is necessary for protein recognition.

1.5.1 Synthesis of ascofuranone and ascochlorin

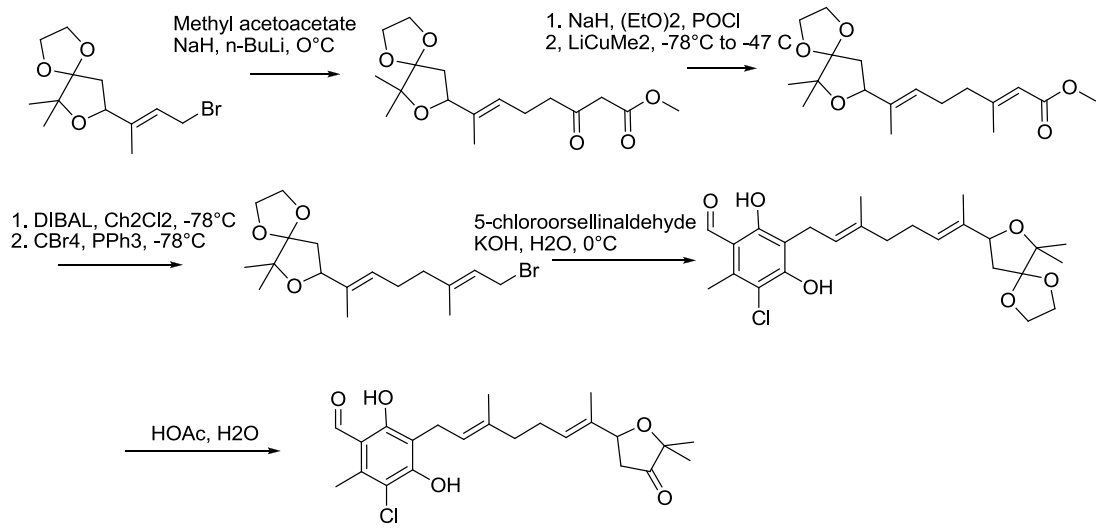

Figure 1-6:- Total synthesis of ascofuranone using the method devised by Joullie and colleagues [116].

One of the first successful total syntheses of ascofuranone was performed by Joullie and colleagues [116, 117] (Figure 1-6). Synthesis of the compound was afforded via separate synthesis of the fully substituted 5-chloroorsinaldehyde, which was coupled to the tail with 10% KOH. This method was demonstrated to be applicable to the synthesis of the colletochlorins, but ascochlorin was not attempted.

The second route published by the Mori group [118, 119] used an alternative approach, coupling the bromonated tail to 1,5-dimethoxy-3-methylcyclohexa-1,4-diene with tBuLi to obtain the intermediate in 33% yield. Successive functionalisation with 2.2 equivalents N-chlorosuccinimide followed by aromatisation with DBU and formylation using EtMeBr and $CH(OEt)_3$ obtained

ascofuranone in 2% overall yield from the coupling step. This method was also demonstrated to be applicable to the synthesis of ascochlorin, obtaining the compound in similar yields.

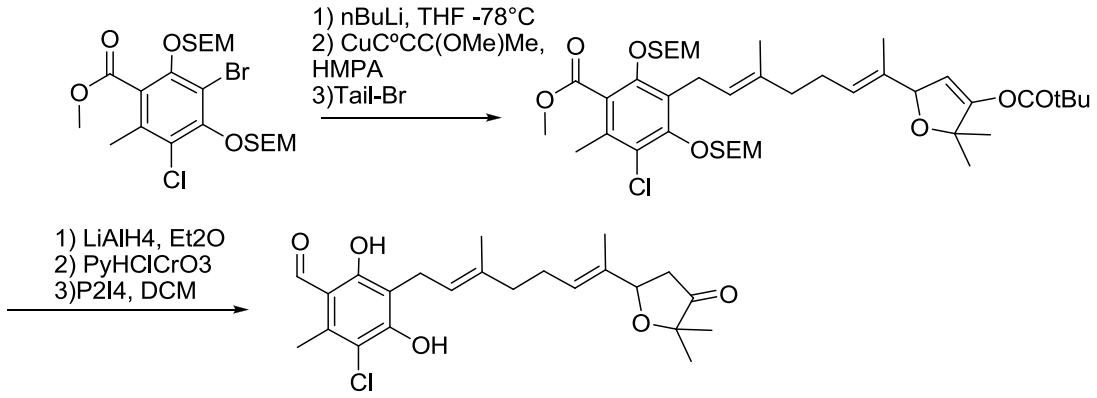

Figure 1-7: Coupling of the protected benzaldehyde and the tail group and subsequent deprotection used by Saimoto [120]

The route taken by Saimoto [120-122] is a more elegant synthesis, making use of the SEM protecting group to allow for cleaner coupling of the benzaldehyde to the tail section. The protected head and tail sections of the compound (Figure 1-7) were synthesised in 5 and 6 synthetic steps respectively, with a cuprate based cross-coupling achieving the product in 70% yield. Subsequent deprotection of the carbonyls followed by removal of the SEM group with P_2I_4 gave an overall yield of 39% with respect to the protected benzaldeyde. The author also demonstrated that removal of the SEM group was possible using TBAF in HMPA in the case of colletochlorin B, but failed to yield the deprotected compound with ascofuranone.

1.6 Fungicides

The alternative oxidase has been identified as a potential biological mechanism for resistance development [123] with evidence that inhibition of the bc_1 complex leads to an induction of the AOX expression [50]. Strobilurins are some of the most

widely used fungicides available, and have been shown to inhibit the cytochrome bc_1 complex at the Qo site [124]. *Candida albicans* has been shown to carry two AOX genes [125]; AOX1a is expressed at all times, while AOX1b is dependent on fungal growth stage while also being induced by H_2O_2 and Antimycin A (a cytochrome bc_1 Q_I inhibitor). As with the plant examples cited previously, inhibition of the ETC downstream from the quinone pool in fungal species leads to induction of AOX [126, 127]. Induction of AOX during inhibition of the regular ETC allows for continued ATP generation from glycolysis and Krebs cycle turnover plus ATP generation via proton-pumping activity of complex I.

While the effects of AOX inhibitors alone are negligible, they have been demonstrated to have a synergistic effect when used in conjunction with Qo inhibitors such as azoxystrobin [128]. Removing the ability of *Magnaporthe grisea* to express AOX demonstrated an increased susceptibility to fungicides during mycelial growth both *in vitro* and *in planta*, but not during the sporulation period [129], suggesting that the alternative pathway is only activated in later stages of fungal development. It was reasoned that due to high energy requirements during the sporulation period, expression of AOX would not rescue the fungus due to its low energy throughput [130], and is therefore not inducible during this growth stage.

Resistance to Qo fungicides largely develop due to point mutations within the Qo site. The first to arise after commercial treatment with the strobiliurins were the G143A and F129L mutants, which gave resistance factors >1000 and ~ 100 respectively [131]. Inhibition of the Qi site with antimycin A showed no alteration in EC_{50}, demonstrating that resistance was due to alterations in the Qo site alone. These mutants cause considerable reduction in ETC turnover, reducing cytochrome c reduction rates to 80% of the wild type [132]. However, this does not decrease fungal viability [133], given that cell growth is not inhibited until the rate is <20% of the full turnover capacity.

1.7 Structure

Initial modelling of AOX performed by Siedow and colleagues [134, 135] was based on sequence comparison to the di-iron carboxylate family, using multiple sequence alignment to highlight the conserved ExxH motifs that are common as non-haem

iron binding residues. The model consisted of a 4 helix bundle which acted as a scaffold for the di-iron centre, ligated by 3 glutamates, 2 histidines and an aspartate residue, based on the Methane monooxygenase (MMO) and Ribonucleotide reductase (RNR) binding motifs. The model also consisted of two transmembrane helices that spanned the membrane, with an additional hydrophobic stretch into the IMS.

A second model was later proposed by Anderson and Nordlund [136] and refined by Berthold [137]. The model replaced the aspartate with a fourth glutamate based on amino acid spacing in the primary structure, which placed iron binding ligands on all 4 of the proposed helices. The binding of the helices to the membrane was refined based on hydrophobicity plots, removing the transmembrane nature and instead associating to the inner membrane.

A number of mutational studies have been performed on AOX in order to ascertain the roles of conserved amino acids. Mutation of the proposed iron binding residues in both plant AOX [138, 139] and TAO [140, 141] completely abolished enzymatic activity, with iron supplementation being necessary for growth of AOX dependant cell lines [140]. Further confirmation that AOX was indeed a di-iron protein came in the form of EPR analysis revealing a characteristic signal at g=15 in *A. thaliana* [139], and g=16 in *S. guttatum* [142], that were comparable to other di-iron carboxylate proteins [143].

Given the apparent lack of cofactors within AOX, it was reasoned that there were likely aromatic amino acid residues that were responsible for electron transport. An extensive sequence alignment across the entire AOX family revealed three fully conserved tyrosines (Y253, Y266 and Y275 SgAOX numbering) with Y299 being semiconserved [144]. Mutation of tyrosine to phenylalanine removes the hydroxide functionality from the amino acid, while retaining the ring, allowing for examination of the importance of the alcohol to function. The location of Y253 and Y275 within the proposed hydrophobic cleft from the Anderson-Nordlund model [137] that constituted a proposed quinone binding site led to mutation of these residues to phenylalanine [138, 145], with Y275F leading to almost a complete loss of activity (~10% activity remained). The importance of this residue was confirmed in recombinant *T.Vivax* [141] whereby the haem deficient *E.coli* strain, dependent upon

successful intergration of a functional AOX for a terminal respiratory chain protein, failed to grow. Respiratory activities of the Y266 and Y299 both retained 10% of wild type activity, indicating that while they are still important residues, they are unlikely to be involved in electron transport.

Sequence alignment of a number of known quinol binding proteins revealed a number of features that were apparent within the AOX in the region of the proposed hydrophobic crevice [146], with particular focus on the HR pair (261 and 262 SgAOX numbering). Subsequent mutation of these residues [145], alongside Q242 and N246, gave activity levels of less than 10% of wild type activity, confirming that they are important to the overall function of the protein.

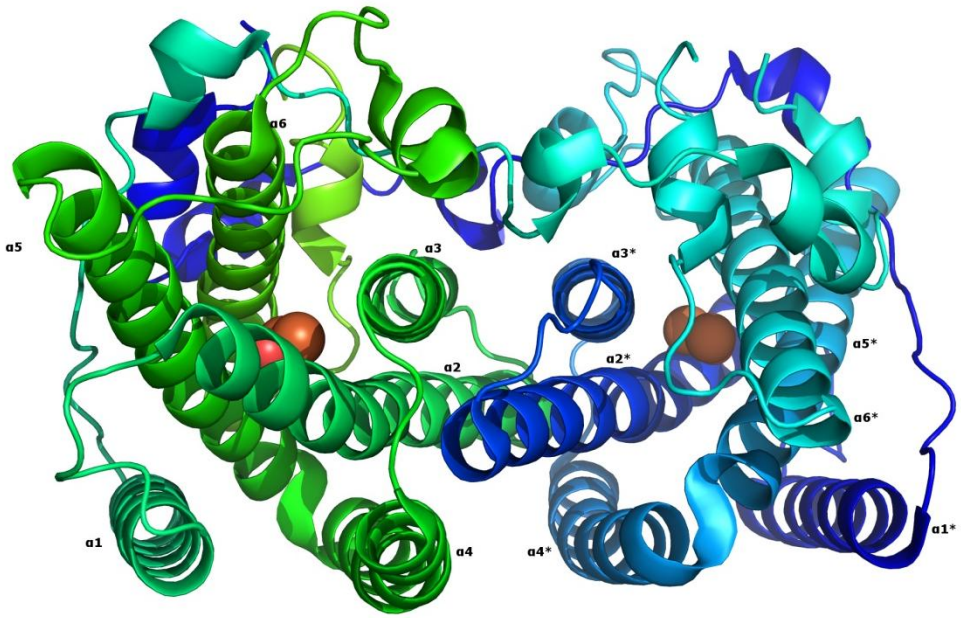

Figure 1-8:- Crystal structure of TAO dimer (PDB accession code 3VV9). Di-iron centre shown as brown spheres, with helical numbering added for reference.

A crystal structure of the TAO has recently been solved [11], confirming a number of the previously discussed structural predictions. TAO exist as a homodimer, with each monomer containing 6 helices (helical labelling depicted in Figure 1-8). The di-iron centre is located within the centre of 4 longer helices arranged in an antiparallel

fashion, conforming to the 4 helix bundle which is found within other di-iron proteins such as MMO and RNR. The remaining two helices (1 and 4) are the proposed membrane binding helices, anchoring the protein onto the membrane. The facets of the crystal structure and the implications of highly conserved regions will be discussed in detail in Chapter 3.

1.8 Structural regulation

Two interlinked post-translational regulatory mechanisms have been identified within the plant AOX that control activity of the protein; deactivation via disulfide bond formation between monomers, and regulation of activity via alpha keto acids. Two cysteine residues 50 amino acids apart are fully conserved throughout the plant species, with C122 (SgAOX numbering) the likely source of disulphide bond formation [147]. While the cause of bond formation in unknown at present, chemical reduction of the disulfide bond with DTT was shown to increase protein activity, while reoxidation by diamine rendered the enzyme inactive [148]. The authors also indicated that dimerisation was not solely due to disulfide bond formation, as cross linkers targeting lysines gave the corresponding dimer band during western blot analysis. Within the mitochondria, it is thought that NADPH [149] is able to reduce the disulphide bond via a mitochondrial thioredoxin [150].

The activity of AOX is increased by alpha keto acids, with particular emphasis on pyruvate [69]. As discussed previously, a build-up of pyruvate would indicate a malfunction of the ETC, and activation via pyruvate correlates to proteins role as a homeostatic regulator. Activation via pyruvate is believed to occur via a mechanism of thiohemiacetal generation [151, 152] through reacting with the cysteine residue responsible for disulphide bridge formation, thus preventing deactivation of the protein via covalent dimerisation [153]. Work performed on purified *A. maculatum* mitochondria confirmed that a lack of pyruvate within a sample does lead to a deactiviation of the protein [154], with subsequent addition of pyruvate failing to restore activity. The lack of activity restoration would indicate that while it does increase the activity of the protein, it is not able to reduce the disulphide bond, suggesting that its role is protein stabilisation. Conversion of this cysteine to a

glutamate residue to mimic a thiohemioacetal gave a protein that was permanently in its active form, while also demonstrated insensitivity to pyruvate [147].

A study on tomato isoforms that contained a common cysteine to serine mutation revealed that mutation to a serine alters activation to succinate [155]. This has also been confirmed independently via point mutation to serine in soybean and *Arabidopsis* AOX [153], and mutation to alanine in tobacco AOX [156] conferred activation via succinate as opposed to pyruvate. This would potentially fall into the same feedback role as pyruvate from a homeostatic standpoint, but would allow for activation to occur earlier in feedback loop.

A second region has also been identified for a potential role in pyruvate activation, with a highly conserved QDC region within SgAOX becoming an ENV motif in the more pyruvate dependant isoforms [154, 157]. This motif exchange was also found in thermogenic spadices, with isoforms expressed later in the spadix growth cycle conferring a QNT motif [158]. The reduction in regulation is likely to allow for continued heat production during thermogenesis, as regulation of activity would effectively lower heat production due to a reduced enzymatic turnover. These regulatory mechanisms are not present in the trypanosomal and fungal species [159], which is indicative to the need for constant turnover and availability within these species.

1.9 Research aims

Ascofuranone has been established as a potent inhibitor of AOX, and ascochlorin demonstrates inhibitory properties of the cytochrome bc_1 complex. Both compounds contain structural motifs that make synthesis of optically pure compounds a lengthy process. The aims of the inhibitor research are twofold; to design an analogue that retains the inhibitory efficacy of the aforementioned compounds that is either specific to AOX for treatment of HAT, or a dual mode inhibitor that could be used as a fungicide. The results of this area of research are discussed in Chapter 5.

Sequence alignment of AOX species throughout the plant, fungal and trypanosomal kingdom has revealed a large extent of conservation throughout the entire family [144], with particular focus of the conservation around the 4-helix bundle. This

information when used in conjunction with the recently published crystal structure [11] allows for determination of a wealth of information from both a structural and mechanistic perspective, and is the subject of discussion in Chapter 3.

Site-directed mutagenesis studies using a haem-deficient *E.coli* strain have been demonstrated to be an efficient method of overexpression of alternative oxidases [140, 141, 160]. A number of conserved amino acids have been mutated, and their effects with respect to respiratory activity and oxygen kinetic parameters have been examined. The use of all information gathered from these studies, alongside structural comparisons to other di-iron proteins, has allowed for the postulation of a working catalytic cycle for alternative oxidases.

2 Materials and methods

2.1 pET vector system

The pET vector system is a useful tool for expression of recombinant proteins within an *E.coli* based system. The pET-15b vector (Figure 2-1) has previously been optimised within the lab for expression of AOX[161].

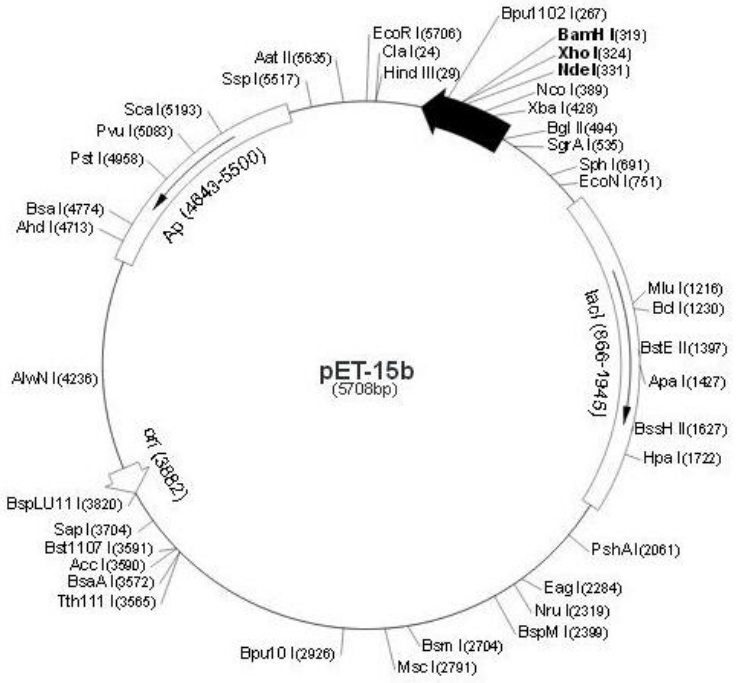

Figure 2-1:- plasmid map for the pET-15b vector.

Plasmid	Encoding	Creator
SgAOX-pET15b	*Sauromatum guttatum* AOX wild type	Dr Mary Albury, University of Sussex
TAO-pET15b	*Trypanosoma brucei brucei* wild type	Dr Mary Albury, University of Sussex
SgAOX-pET15b: mutants D163A, R159A, L177A, T179A, N216A, L269A Y299F	*Sauromatum guttatum* AOX mutants	Dr Mary Albury, University of Sussex
TAO-pET15b mutants: T124A	*Trypanosoma brucei brucei* mutant	Dr Mary Albury, University of Sussex

Table 2-1: Plasmids created by Dr. Mary Albury for the expression of wild type SgAOX and TbTAO and their corresponding mutants using the pET-15b expression system

A library of plasmids were created (Dr. Mary Albury – University of Sussex Table 2-1) for transformation into *E.coli* using the pET-15b vector system (Novagen). The pET-15b vector contains encoding for addition of an N-terminal His tag, resistance to ampicillin and allows for induction of protein expression via isopropyl β-D-1-thiogalactopyranoside (IPTG).

E.coli strain FN102 was transformed using the aforementioned plasmids. Strain FN102 is a haem deficient strain developed and kindly provided by Professor Kita (University of Tokyo). Transformation and growth of the *E.coli* was carried out using a modified protocol of that described in [160].

2.2 Culture medium

K-broth (KB)

Chemical	Concentration g/L
Trytone peptone	10
Yeast extract	5
Casamino acid	5
K_2HPO_4	10.4
KH_2PO_4	3
Trisodium citrate	0.74
Ammonium sulphate	2.5

Supplement – A

Chemical	Concentration g/L
Magnesium Sulphate	0.05
Iron Sulphate	0.025
Iron Chloride	0.025

Table 2-2:- Contents of K-broth and supplement A,

Table 2-2:- Contents of K-broth and supplement A, Table 2-2 contains the recipe for KB and supplement A, used as the growth medium for haem deficient *E.coli*. The KB was mixed and sterilised prior to culture growth via autoclave, with supplement A added 30 minutes before the addition of *E.coli.*Luria Broth and Luria Agar (Miller, Sigma Aldrich) were prepared as per manufacturer's instructions, with additives added as described in text.

2.2.1 Competent cells

E.coli (strain FN102) was plated onto Luria Agar (100µg/ml 5-Aminolevulinic acid (ALA), 50 µg/ml Kanamycin (Kan)) and incubated overnight at 37°C. A single colony of fresh *E.coli* cells were used to inoculate 5ml LB containing 100µg/ml ALA, 50µg/ml Kan and left in an orbital shaker at 37°C overnight. 1ml of this culture was used to inoculate 100ml of LB and was incubated at 37°C until OD_{650}

was 0.5. The culture was chilled on ice before centrifugation at 1000g for 5 minutes at 4°C. The pellet was resuspended in 50ml 0.1M $CaCl_2$. This was repeated twice and the final pellet chilled on ice for 30 minutes. The final pellet was resuspended in 5ml 0.1M $CaCl_2$. Competent cells can be stored at -80°C by resuspending the cells into a solution containing 10% glycerol, 0.075M $CaCl_2$, and aliqouting into 0.5ml prior to flash freezing in a dry ice industrial methylated spirit bath.

2.2.2 DNA Transformation

DNA transformation was performed as described by Mandel and Higa [162]. Two 100µl aliquots of competent cells were chilled on ice. 2µl of DNA was added to one aliquot, and 2µl of water added to the second as a control. The cells were gently mixed and left on ice for a further 30 minutes, prior to being heat shocked at 42°C for 2 minutes and returned to the ice. After 20 minutes 900µl LB was added and the cells were incubated at 37°C for 30 minutes. 100µl was plated out onto Luria Agar containing 100µg/ml ALA, 50 µg/ml Kan, 50 µg/ml ampicilin, and the remaining cells were pelleted and plated out onto a separate plate. The plates were allowed to grow overnight at 37°C in an incubator.

2.2.3 Protein expression in *E.coli*

A colony was taken from freshly transformed cells and streaked onto a Luria Agar plate containing 100µg/ml ALA, 50 µg/ml Kan, 50 µg/ml ampicilin and placed in an incubator at 37°C for 12hours overnight. A loop of cells was then used to inoculate two 50ml starter cultures of KB containing 100µg/ml ALA, 50 µg/ml Kan, 50 µg/ml ampicilin and placed in an orbital shaker at 30° for 4 hours. The starter cultures were centrifuged at 5 000g for 10 minutes, and resuspended in ~10mls fresh KB containing no additives. This was repeated twice to remove any excess ALA, and resuspended in a final volume of 5ml KB. The OD_{600} of the resuspended cells was measured, and added to the main culture flasks containing KB, supplement A and glucose to give a starting OD_{600} of 0.01. The flasks were transferred to an orbital shaker at 37°C and OD_{600} were taken hourly until a reading of 0.1 was obtained (~3hours). At OD_{600} 0.1 the cells were induced with IPTG (final concentration 25

µM for SgAOX and mutants, 100 µM for TAO) and the cultures left to grow overnight (~14hours).

2.2.4 Membrane harvest

Cells were centrifuged at 8000g and supernatant discarded before resuspension in 50mM TRIS-HCl (containing 10mM pyruvate for SgAOX) pH 7.4 at a volume of 5ml per 1g wet weight. Protease inhibitor cocktail tablets (1 tablet per 50ml volume – cOmplete - Roche) were added to the cells. The mixture was homogenised prior to being passed twice through a French press (Thermospectronic) at 10kPa. The lysate was centrifuged at 15000g for 15mins to remove the cell debris, and the supernatant spun at 200000g for 1 hour in an ultracentrifuge. The membrane pellet was resuspended in an appropriate volume of 50mM TRIS-HCl and homogenised.

Membrane samples could be stored for extended periods of time by snap freezing in liquid nitrogen and storing at -80°C.

2.3 Purification

Purification of the SgAOX was achieved using a modified protocol of the TAO purification procedure [163].

Chemical	Solubilisation buffer	Wash Buffer	Elution buffer
TRIS-HCl pH 7.4	50mM	50mM	50mM
pyruvate	10mM	10mM	10mM
DDM	1% (w/v)	0.5% (w/v)	0.5% (w/v)
C12E8	-	0.5% (w/v)	0.5% (w/v)
Glycerol	20% (v/v)	20% (v/v)	20% (v/v)
Magnesium sulphate	-	100mM	100mM
Imidazole	-	20mM	250mM

Table 2-3:- Buffer contents for protein purification. Buffers were prepared on day of purification and stored on ice until use.

2.3.1 Protein Solubilisation

E.coli membrane samples were placed on ice for 30 minutes, before being added dropwise to an equal volume of solubilisation buffer (Table 2.3 ref not working))with constant agitation to ensure adequate mixing. This was kept on ice for 30 minutes with stirring. The mixture was transferred into ultracentrifuge tubes and centrifuged at 200,000g for 1 hour**.** The supernatant containing the solubilised protein was taken forward, and the pellet resuspended in 50mM Tris-HCl to allow for protein estimation and activity measurements.

2.3.2 Protein purification

A volume of cobalt affinity chromatography resin (Sigma-Aldrich) equal to the solubilised protein volume was spun at 2300g for 1 minute and the ethanol aspirated off. The beads were resuspended in solubilisation buffer at 3 times the bed volume and equilibrated on ice for 10minutes with occasional agitation. The beads were spun at 2300g and the buffer removed. The solubilised protein was added to the beads and allowed to bind for 1 hour on a rotor spinning at 2rpm in a cold room.
For bed volumes less then 500µl a batch process was used. The beads were placed in a 1.5ml eppendorf and spun at 2300g for 1 minute, and the supernatant removed and kept as flowthrough. A volume of wash buffer equal to 5 times the bed volume was added to the eppendorf and the sample was agitated on ice for 5 minutes before being spun and the wash being removed and retained. This was repeated before a final addition of the elution buffer equal to three times the bed volume was added and spun as before.

For bed volumes greater than 500µl

The beads were then applied to a plastic column and allowed to settle before the remaining solubilised protein was run off and collected as flow-through for testing. The beads were then washed twice with 5 times bed volume of wash buffer with the

washes being collected for analysis. The protein was then eluted with 3 times bed volume Elution buffer.

2.3.3 Top loaded protein purification

An alternative method was also used whereby the equilibrated beads were applied to the column and allowed to settle. Excess equilibration buffer was run off and the solubilised protein was applied to the top of the column. The liquid level was lowered to above the top of the column and allowed to bind in the cold room for 30 minutes, before being washed twice with 5 times the bed volume with wash buffer and eluted.

2.3.4 Protein precipitation

Precipitation of the purified protein was necessary for obtaining an accurate protein estimation as it was found that the detergents were interfering with the estimation kit. The purified protein was added to 4 x volume of ice cold acetone in a 1.5ml centrifuge tube and incubated at -20°C for 1 hour. The protein was pelleted in a benchtop centrifuge (6,000g – 20minutes), and the acetone removed. Pellets were dried in a 37°C water bath for 1 hour before resuspension in 5% (w/v) SDS 0.1M NaOH prior to protein estimation.

2.4 Protein estimations

Protein estimations were carried out with Pierce BCA protein assay kit (Thermo Scientific) following manufacturer's instructions. Samples were diluted as appropriate (50:1 in water for membrane and mitochondrial samples, as precipitated for purified protein) and 100 µl added to 1ml BCA working reagent (50:1 A:B from kit), with triplicates of all samples being prepared. BSA standards were prepared at concentrations of 0, 0.1, 0.2, 0.4, 0.6, 0.8 and 1 mg/ml in duplicates using the same ratio of sample to BCA working reagent. The solutions were thoroughly mixed, and

allowed to incubate at 37°C for 30 minutes. After incubation the absorbance at 562nm of each sample and standard was measured, with BSA standards used to plot a standard curve for determination of sample protein concentration.

2.5 Mitochondrial preparations

2.5.1 *Arum maculatum* mitochondria

Approximately 100g of spadices were harvested from *Arum maculatum* and stored on ice. After cooling, the spadicies were sliced and placed into 500ml ice cold grinding buffer (0.3M mannitol, 20mM MOPS, 2mM EDTA, 7mM cysteine,2mM pyruvate, 0.2% (w/v) BSA pH 7.5) before homogenisation in a blender (waring). The homogenate was passed through muslin before centrifugation (10mins, 200g). The supernatant was then taken and recentrifuged (10mins, 17000g) and the pellet resuspended in wash buffer (0.3M mannitol, 20mM MOPS, 2mM EDTA, 2mM pyruvate, 0.2% (w/v) BSA, pH 7.5). This was respun under the same conditions and the final pellet was resuspended in ~2ml wash medium.

The mitochondria were layered onto a Percoll gradient (21% (v/v) percoll, 0.3M sucrose, 5mM MOPS, 0.1% (w/v) BSA, 2mM pyruvate) and centrifuged for 30mins at 13,000g with no deceleration to purify the mitochondria. The mitochondrial layer was transferred to new centrifuge tubes and centrifuged for 10 mins at 13,000g before resuspension in wash medium.

For storage purposes, the samples were slow frozen at -20°C for an hour before being transferred to a -80°C freezer for long-term storage.

2.5.2 Potato mitochondria

Potato mitochondria were prepared as the *A. maculatum* mitochondria described in 2.5.1. 1kg of potato tuber (purchased from Waitrose) were necessary to obtain

enough mitochondria. The mitochondria were not purified on a Percoll gradient as it was found to be detrimental to activity.

2.6 Fungal plate assays

A *S.cervisiae* cell line containing wild type cytochrome bc_1 , G143A, K228M and the double mutant were kindly provided by Brigitte Meunier (Centre de Génétique Moléculaire). Cells were plated onto yeast-extract peptone D-glucose (YPD) agar (2% yeast extract, 2% (w/v) bacteriological peptone, 2% (w/v) glucose, 2% (w/v) agar) and allowed to grow in an incubator at 37°C overnight. A loop of cells was then taken and placed into a 5ml YPD liquid culture (2% (w/v) peptone, 2% (w/v) yeast extract, 2% (w/v) glucose) and incubated at 30°C for 2 days. 1µl was transferred into 5ml yeast-extract peptone glycerol (YPG) media (2% (w/v) peptone, 2% (w/v) yeast extract, 2% (v/v) glycerol) and stirred. 5µl was then plated onto YPG plates (as media, with 2% (w/v) agar) and allowed to grow at 37°C for 3 days.

2.7 Gels

2.7.1 SDS PAGE gel

Reagent	Contents	Notes
2 x Loading dye	0.1M Tris-HCl pH 6.8 10mM EDTA 2% (w/v) SDS 5% (w/v) glycerol 0.05% (w/v) bromophenol blue	
10 x Running buffer	0.1M TRIS-HCl, pH 6.8 10mM EDTA 2% (w/v) SDS 5% (w/v) glycerol 0.05% (w/v) bromophenol blue	
10 x TBST (Tris-buffered saline tween)	140mM NaCl 20mM Tris-HCl pH 7.6 0.1% (v/v) Tween-20	Diluted to 1 x working with distilled water
10 x Transfer buffer	1.92M glycine 13mM TRIS pH 7.2	Diluted to working reagent by 8 parts distilled H_20, 1 part methanol (typical volume of 1 liter for single transfer setup)
Blot rinse	10mM TRIS pH 7.2 5mM EDTA	
Block	2 % (w/v) milk powder 3%(w/v) BSA	In 1 x TBST

Table 2-4:- Contents of Reagents used in SDS gels and Western Blots.

2.7.1.1 Sample preparation

Purified protein samples required precipitation (as described in 2.3.4) prior to SDS gels to allow for concentration of the sample. Membrane samples were diluted with

distilled water to a final concentration of 3µg/1µl. This was added to 50µl of 2 x loading dye (Table 2-4) and denatured in a hot block at 90°C for 3 minutes.

2.7.1.2 Gel preparation

Reagent	Volume/ml
H_20	**5.65**
Stacking buffer (0.5M Tris-HCl, pH 6.3)	**2.5**
10% SDS	**0.1**
30% acrylamide:bisacrylamide	**1.65**
10% APS	**0.1**
TEMED	**0.01**
Total volume	**10ml**

Table 2-5:- Contents of the stacking gel for SDS-page gels. Total volume is sufficient for 4 gels

Reagent	Volume/ml
H_20	**11.88**
Resolving buffer (1.5M Tris-HCl pH 8.8)	**7.5**
10% SDS	**0.3**
30% acrylamide:bisacrylamide	**10**
10% APS	**0.3**
TEMED	**0.02**
Total volume	**30ml**

Table 2-6:- contents of the stacking gel for SDS-page gels. Total volume sufficient for 4 gels

Gels were cast in a Biorad Mini Protean kit, giving 10cm x 8cm x 1mm gels. Two glass plates were separated by a spacer and assembled into the plate holder. The plates were filled with distilled water for 5 minutes to ensure there was no leakage, and the water was emptied from the setup. Resolving gel was prepared as in Table 2-5, with addition of components in order on the list. Upon addition of TEMED, the mixture was thoroughly mixed and used to fill the plates to 2/3rds of the plate height. This was overlaid with propanol and allowed to set for 30 minutes. Once set, the propanol was removed and the gel was overlaid with stacking gel (contents described

in Table 2-6) and a comb was inserted. The stacking gel was allowed to set, and the unit was disassembled. The gels could be stored for up to 3 weeks if soaked in running buffer (Table 2-4) in the fridge.

2.7.1.3 Gel electrophoresis

Two gels were attached to an electrophoresis rig and submerged in 1 x SDS running buffer. 10 µl of the previously prepared samples (15µg) were loaded into the gel with rainbow markers (colourplus prestained, 7-175kDa, Biolabs) and the powerpack was attached. The gels were run at 150V for 1 hour, or until the dye front reached the bottom of the gel. The gels were removed from the electrophoresis rig and rinsed with distilled water. One of the gels was then stained with GelCode Blue (ThermoScientific) following manufacturer's instructions. The gel was removed from the glass plates and the loading section removed. The gel was placed in a plastic container on an agitator and washed 3 times with distilled water for 15 minutes. GelCode Blue was added to the sample for 1 hour. This was removed and the gel destained in distilled water overnight.

2.7.2 Western Blot analysis

The second gel of the pair was used for western analysis. The gel was removed from the glass plates and washed with 1 x transfer buffer. A transfer cassette, complete with 2 sponges, 2 pieces of 3mm transfer paper and nitrocellulose membrane were also equilibrated in 1 x transfer buffer (Table 2-4). The cassette was assembled, rolling a testtube over the top of the sponges to ensure exclusion of air bubbles. This was then placed into a transfer rig with 2 ice packs in a cold room, and the tank was filled with 1 x transfer buffer. A power pack was connected to the transfer rig and was run for 1 hour at 100V, changing out the ice packs if melted to maintain a low temperature and prevent denaturing or the nitrocellulose membrane. After 1 hour, the rig was disassembled and the nitrocellulose placed into a plastic box.

To ensure transfer of protein, the nitrocellulose membrane was stained with ponceau solution, marking the lanes and markers for later reference. The solution was rinsed off with 1 x TBST (Table 2-4). The membrane was then soaked in 20ml block solution (2% (w/v) milk powder, 3% BSA (w/v) in 1x TBST) for 2 hours at room temperature on an agitator, before 10µl of primary antibody (anti-AOX[164], dilution 1:5000) was added. This was left on an agitator for 1 hour before a quick wash with 1xTBST, followed by 6 x 5 minute washes in1x TBST. A second 20ml aliquot of block solution was added to the film and 10 µl of secondary antibody (rabbit anti-mouse with HRP conjugate, Dako BioProducts, 1:20,000 dilution) was allowed to bind for 1 hour followed by another series of 1xTBST washes. This was followed by a final 15minute wash in 1 x blot rinse (Table 2-4), and the membrane was dried with blotting paper before transferring into saran wrap for detection.

2.7.3 Detection

A chemiluminescence kit (ECL Detection Kit, GE Healthcare) was used for detection purposes. The membrane was transferred to the dark room and exposed to 1ml reagent 1 for 3 minutes, followed by 1ml reagent 2 for 1 minute. Excess liquid was removed using blotting paper, and the membrane was rewrapped in saran wrap, ensuring no bubbles were trapped. The membrane was attached to the inside of an exposure cassette and the light turned off, at which point a piece of X-ray film (Fujifilm Super RX Medical X-ray film) was inserted into the cassette and exposed to the membrane for 1 minute. The film was then removed from the cassette and developed in an autorad developer (Konika SRX-101A). The positions of the lanes and markers were noted in the film. If a longer exposure was necessary, a second piece of film could be added to the cassette and exposed for the desired time.

2.8 Analytical techniques

2.8.1 General

All inhibitors were made to a stock solution of 10mM in DMSO, with serial dilutions in propanol.

Media	contents	Used for
Plant medium A	300mM manitol 1mM $MgCl_2$ 10mM KCl 5mM K_2HPO_4 20mM MOPS pH 7.2	Plant mitochondria
Tris	50mM Tris-pH 7.4 10mM Pyruvate	Recombinant membrane Purified recombinant

Table 2-7:- contents of buffers used for assays

2.8.2 Oxygen electrode

Oxygen concentration in solution was measured voltametrically using a Rank oxygen electrode. The electrode consists of a silver anode and platinum cathode, with conduction between the two achieved using saturated KCl. The electrode is polarized at ~0.6V, whereby changes in measured voltage are due to the following reactions:-

(anode) $4Ag \rightarrow 4Ag^+ + 4e^-$

(cathode) $O_2 + 4e^- + 4H^+ \rightarrow 2H_2O$

The electrode is separated from the reaction chamber via an oxygen permeable membrane, with a magnetic stirrer used to ensure even oxygen distribution between

the reaction and electrode chambers. The reaction chamber is sealed with the exception of a capillary tube that allows the addition of substrates via micro syringe. The electrode was calibrated against air saturated distilled water (250 µM at 25°C) for 100%, and addition of sodium dithionite for 0%.

2.8.3 Spectrophotometric enzyme assays

Spectrophotometric assays were run using a Cary 400 UV spectrophotometer, using the packaged software. All spectrophotometry were performed using a quartz cuvette with a 1ml path length.

Kinetic assays

Compound	**Wavelength measured(nm)**	**Extinction coefficient /$AM^{-1}cm^{-1}$**
Quinol (Q_1H_2)	278	17000
Duroquinol (H_2O)	250	7.1
NADH	339	6200
DCPIP	600	21000

Table 2-8:- Wavelengths and extinction coefficients used for the kinetic assays.

Spectrophotometric kinetic assays were run using the Kinetics package (Cary WinUV biopackage). The spectrophotometer was set to the wavelength defined in Table 2-8, and blanked against the solvent. The substrate was added and the kinetic scan started for 1 minute to allow for the collection of auto-oxidation rates. The protein was then added, and a change in absorbance over time was determined.

Scanning assays

Scanning for specific wavelengths was done using the Scan package (Cary WinUV biopackage). The sample was baselined against the solvent, and the sample could be added to the cuvette and scanned for the desired wavelengths. Scanning assays were predominantly used for determination of substrate concentration using the extinction coefficients in Table 2-8.

2.9 Crystal structures analysis

Crystal structures used

PDB accession number	Protein	Description	Reference
3VV9	TAO	No inhibitor 2.9 Å	[11]
3VVA	TAO	Contains Ascofuranone derivative 2.6 Å	[11]
3W54	TAO	Contains colletochlorin B 2.3 Å	[11]
1FYZ	MMO	Reduced structure 2.15 Å	[165]
1MTY	MMO	Oxidised structure 1.7 Å	[166]
1R65	RNR	Reduced structure 1.95 Å	[167]
1RIB	RNR	Oxidised structure 2.2 Å	[168]
1PIM	RNR-D84E	Reduced structure 2.0 Å	[169]
1PIU	RNR-D84E	Oxidised structure 2.2 Å	[169]
3H1L	Chicken bc_1	Bound Ascochlorin 3.2 Å	[113]
1SQB	Bovine bc_1	Bound azoxystrobin 2.7 Å	[170]
1LKO	Rubrerythrin	Reduced structure 1.6 Å	[171]

Table 2-9:- PDB accession codes for crystal structures used. Protein codes refer to the following proteins : Trypanosomal alternative oxidase (TAO), methane monooxygenase (MMO) ribonucleotde reductase (RNR), ribonucleotides reductase D84E mutant (RNR-D84E), Cytochrome bc_1 complex (bc_1).

Table 2-9 contains the details for the crystal structures used throughout this thesis.Crystal structures were visualized using PyMOL version 1.3 (www.pymol.org), with analysis of protein cavities was undertaken using the CAVER 3.0 plugin[172]. Docking was carried out using the VINA autodock system packaged on www.mcule.com, and visualized for clarity using PyMOL.

2.10 Chemical synthesis

General procedures

Reactions were monitored via thin layer chromatography (TLC) using precoated silica sheets with fluorescent indicator $UV_{254.}$ Compound detection was achieved by developing the plates by staining with a potassium permanganate solution (potassium permanganate (3g) + potassium carbonate (20g) + 5% (w/v) aqueous NaOH (5ml) + water (300ml)) with subsequent heating revealing the compounds as yellow spots.

Chromatographic purification was performed using silica gel 60A 'Davisil' (35-70μM particle size). Solvents for chromatography were used as received, with the exception of ethyl acetate which was distilled prior to use.

Anhydrous ether was prepared via distillation for a minimum of 72 hours over sodium potassium alloy.

^{1}H NMR, ^{13}C NMR and multidimensional spectra were recorded on a Varian VNMRS spectrometer (600MHz). Chemical shifts in ^{1}H and ^{13}C were referenced to residual proton resonance of the solvent $CDCl_3$ (7.26ppm), CD_3OD (3.31ppm) and C_3D_6O (2.05ppm).

HR-ESI-MS spectra were recorded on a Brucker Daltonics Apex III with MeOH as solvent. Mass spectroscopy was performed by Dr. Alaa Abdul-Sada (University of Sussex).

2,4-dihydroxy-6-methyl-benzaldehyde (1)

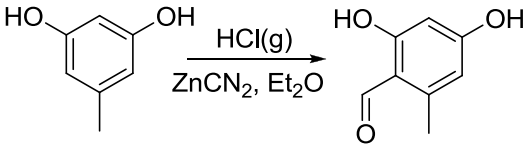

Orcinol (5g, 40mmol) and $Zn(CN)_2$ (7.1g, 60mMol) were placed into a 3 necked flask with mechanical stirrer under N_2. Anhydrous ether (50ml) was added, and the reaction was saturated with HCl gas. After 2 hours, the ether was decanted off and

water (50ml) was added to the reaction mixture. This was heated to 100°C where the product crashed out of solution. The crude product was collected via Büchner filtration, and recrystallised from water to yield the pure aldehyde (4.6g) in 76% yield.

^{1}H NMR ($CDCl_3$): 12.38 (1H, s, O**H**), 10.11 (1H, s, C**H**O) 6.23 (2H, s, C**H** signals overlap) 5.52 (1H, s, O**H**) 2.54 (3H, s, C**H**$_3$)

^{13}C NMR ($CDCl_3$): 192.6 (**C**HO) ,164.3 (**C**OH), 160.7 (**C**OH), 141.3 (**C**CH_3) 125.2 (**C**H) , 113.8 (**C**CHO) , 101.2 (**C**H), 17.86 (**C**H_3)

3-chloro-4,6-dihydroxy-2-methyl-benzaldehyde (2)

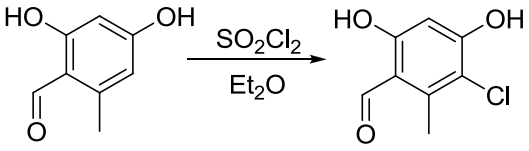

4,6-dihydroxy-2-methyl-benzaldehyde (527mg, 3.5mMol) was put under N_2 and dissolved in anhydrous ether (60ml) on an ice bath. SO_2Cl_2 (1.35ml, 4.7mmol) was diluted in ether (15ml) and then added dropwise over 15 minutes. The reaction was left to stir overnight, and quenched with the addition of water. The ether layer was washed with 0.1M $NaHCO_3$ and water, then dried over $MgSO_4$ and dried under vacuum. The crude solid was then purified via flash chromatography (toluene: ethyl acetate 2:1 → 1:1) to obtain the product (434mg) in 72% yield.

^{1}H NMR (C_3D_6O) 12.52 (1H, s, O**H)** 10.22 (1H, s, C**H**O) 6.42 (1H, s, C**H**) 2.67 (3H, s, C**H**$_3$)

^{13}C NMR (C_3D_6O) 194.2 (**C**HO), 160.5 (**C**OH), 141.7 (**C**CH_3), 114.6 (**C**Cl) 113.4 (**C**CHO), 101.3 (**C**H), 13.8 (**C**H_3)

(E)-1-bromo-3,7-dimethylocta-2,6-diene (3)

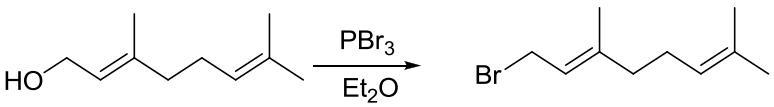

Geraniol (0.56ml, 3mMol) was added to a round bottomed flask containing anhydrous diethyl ether (10ml) on ice under a nitrogen atmosphere. After stirring for 10minutes, phosphorus tribromide (0.123ml, 1.2mM) was added dropwise via syringe. The solution was allowed to stir for one hour before quenching with aqueous sodium hydrogen carbonate. The aqueous layer was extracted twice with diethyl ether. The organic layer was dried over magnesium sulphate and the ether removed under vacuum to yield geranyl bromide in quantitative yield. The same method was used for the synthesis of 3-3-dimethylallyl bromide, with care taken during rotary evapouration due to its decreased vapour pressure. Compound identity confirmed with appearance of C-Br stretch using IR spectroscopy.

(E)-3-chloro-5-(3,7-dimethylocta-2,6-dienyl)-4,6-dihydroxy-2-methylbenzaldehyde ---Colletochlorin B (4)

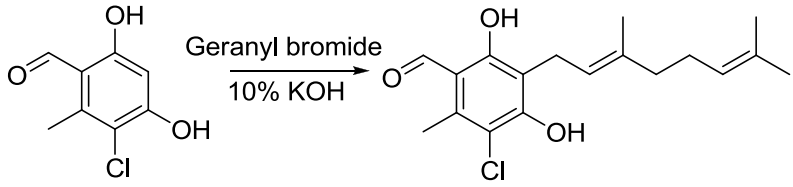

3-chloro-4,6-dihydroxy-2-methyl-benzaldehyde (150mg, 0.8mmol) was dissolved in 10% KOH (0.9ml, 0.8mmol) yielding a deep red solution. The reaction was placed on an ice bath, and geranyl bromide (0.39ml, 1.6mmol) was added. The reaction was stirred vigorously overnight, and extracted with ether. The organic layer was washed with $NaHCO_3$ and brine, before being concentrated under vacuum. The resultant oil was purified via flash chromatography (petrol ether 60-80 : ether 10:1 → 3:1) to obtain pure colletochlorin B (52mg) in 20% yield. Synthesis of colletochlorin D was afforded in the same manner, substituting geranyl bromide for 3-3-dimethylallyl bromide giving a yield of 30%.

^{1}H NMR (C_3D_6O) 12.88 (1H, s, CO**H**) 10.22 (1H, s, C**H**O) 5.24 (1H, t, J_{H-H} 7.2) 5.06 (1H, t, J_{H-H} 7.13, C**H**) 3.39 (2H, d, J_{H-H} 7.14, ar-C**H**$_2$) 2.65 (3H, s C**H**$_3$) 2.05 (m, 2H C**H**$_2$) 1.96 (t,2H, J_{H-H} 7.2 C**H**$_2$) 1.77(3H, s, C**H**$_3$) 1.60 (3H, s, C**H**$_3$) 1.55 (3H, s, C**H**$_3$)

^{13}C NMR (C_3D_6O) 194.4 (**C**HO) ,161.8 (**C**OH) ,157.4 (**C**OH), 138.3 (CH**C**(CH_3)CH_2)), 135.2 ((ar)**C**CH3), 130.7 (**C**CH_3(CH_3)), 123.1(CH_2**C**H), 121.4(CH_2CH_2**C**H), 114.5 (**C**CHO), 113.3 (**C**Cl), 109.9(ar-**C**CH_2CH), 39.5 (CH_2**C**H_2CH), 26.4 (**C**H_2CH_2CH), 24.8 (CHC**C**H_3) , 21.6(ar-**C**H_2CH), 16.7 (C**C**H_3CH_3),15.3(CCH_3**C**H_3), 13.6 (ar-**C**H_3)

Predicted m/z $C_{18}H_{23}ClO_3Na$:- 345.1233

Detected m/z $C_{18}H_{23}ClO_3Na$:- 345.1228

(E)-4-chloro-2-(3,7-dimethylocta-2,6-dienyl)-6-formyl-5-methyl-1,3-phenylene diacetate (Acetylated) (5)

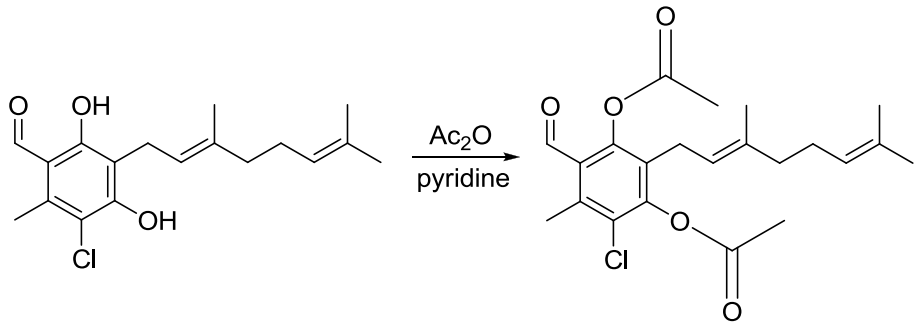

Colletochlorin B (16mg, 50µMol) was added to a flask containing pyridine (0.5ml). After stirring for 10minutes, Acetic anhydride (0.5ml) was added and the reaction was left to stir overnight. The reaction mixture was evapourated to dryness, then coevapourated with toluene followed by DCM to obtain pure actylated compound in quantitative yield.

^{1}H NMR ($CDCl_3$) 10.27 (1H,s, C**H**O), 5.06 (1H, t, J_{H-H} 6.87 C**H**) 4.98 (1H, t, J_{H-H} 6.13 C**H**) 3.21 (2H, d, 5.62 ar-C**H**$_2$) 2.67 (3H,s,ar-C**H**$_3$). 2.62

(3H, s C**H**$_3$) 2.35 (6H, s , COC**H**$_3$ x 2) 2.03 (m, 2H C**H**$_2$) 1.97 (m, 2H, C**H**$_2$) 1.72 (3H,s,C**H**$_3$)1.66 (3H,s,C**H**$_3$) 1.58 (3H,s,C**H**$_3$)

(E)-4-chloro-2-(3,7-dimethylocta-2,6-dienyl)-6-(hydroxymethyl)-5-methylbenzene-1,3-diol –reduced colletochlorin B (6)

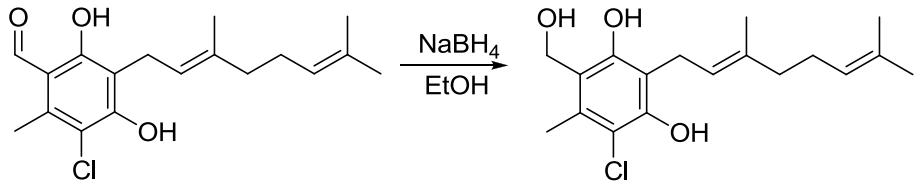

Colletochlorin B(14mg, 44µMol) in ethanol (0.5ml) was transferred into a flask containing a suspension of $NaBH_4$ (1mg in 0.5ml ethanol) and left to stir for 1 hour. The mixture was coevaporated 3 times with methanol, before purification via flash chromatography (2:1 petrol ether:ether) to obtain the reduced compound (7mg) in 50% yield.

Rf = 0.21 (4:1 petrol ether:ether)

^{1}H NMR ($CDCl_3$)	7.12 (1H, s, O**H**) 5.73 (1H, s O**H**) 5.27(1H, t, J_{H-H} 7.01 C**H**) 5.07 (1H, t, J_{H-H} 6.36 C**H**) 4.84 (2H, s C**H**$_2$OH) 3.44 (2H, d, J_{H-H} 6.95) 2.09 (2H, m C**H**$_2$) 2.04 (2H, m C**H**$_2$) 2.35 (3H, s C**H**$_3$) 1.81 (3H, s C**H**$_3$) 1.67 (3H, s C**H**$_3$) 1.60(3H, s C**H**$_3$)
^{13}C NMR ($CDCl_3$)	153.9(**C**OH), 149.3(**C**OH), 137.9 (**C**CH$_3$), 131.7(**C**CH$_3$(CH$_3$)), 131.4(CH**C**(CH$_3$)CH$_2$), 123.9 (CH$_2$**C**H), 121.4(CH$_2$CH$_2$**C**H), 117.2 (**C**Cl), 113.2 (ar-**C**CH$_2$CH$_2$), 59.8(**C**H$_2$OH), 39.7(**C**H$_2$CH$_2$CH), 29.6 (CH$_2$**C**H$_2$CH), 26.4(**C**H$_3$), 23.0(**C**H$_3$), 16.1(**C**H$_3$), 15.9 (ar-**C**H$_3$)

Predicted m/z $C_{18}H_{23}ClO_3Na$:-	347.1390
Detected m/z $C_{18}H_{23}ClO_3Na$:-	347.1378

3-chloro-4,6-dimethoxy-2-methylbenzaldehyde (7)

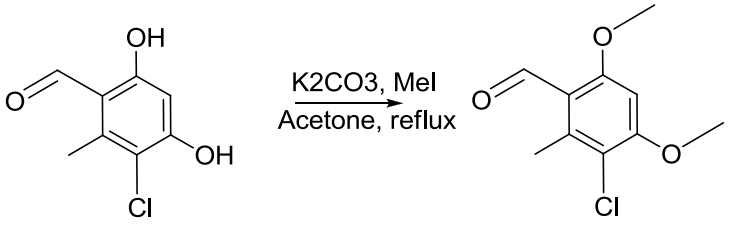

3-chloro-4,6-dihydroxy-2-methyl-benzaldehyde (150mg, 0.3mMol) and potassium carbonate (336mg, 2.6mMol, 7.2eq) were stirred in acetone (15ml) for 20minutes to form a suspension. Methyl iodide (0.288ml, 4.6 mMol, 15eq) was added and the suspension was refluxed for 24hours. The suspension was evaporated to dryness under reduced pressure and dissolved in 10ml ethyl acetate. The organic phase was washed with 3 x 5ml water, dried over magnesium sulphate and re-evapourated. The crude product was purified via flash choromatography (toluene:ethyl acetate 4:1) to obtain the product in 40% yield.

^{1}H NMR ($CDCl_3$)	10.42 (1H, s C**H**O) 6.37 (1H, s C**H**) 3.94 (3H, s OC**H**$_3$) 3.89(3H, s OC**H**$_3$) 2.63(3H, s ar-C**H**$_3$)
^{13}C NMR ($CDCl_3$)	190.1 (**C**HO), 163.3 (**C**OMe), 159.6 (**C**OMe), 140.8 (**C**CH$_3$), 117.6(**C**Cl), 116.5(**C**CHO), 93.3 (**C**H), , 56.3(O**C**H$_3$), 56.2(O**C**H$_3$), 16.8 (**C**H$_3$).

3 Structural analysis of TAO

3.1 Introduction

Recent crystallisation of TAO [11] allows for a more in-depth examination as to the role of highly conserved amino acids within the alternative oxidase family, and can defined as being either structurally or mechanistically important, with a majority of conserved residues performing both roles. TAO is a useful model system for plant AOX given its simpler nature; the lack of regulatory mechanisms [159] allow for identification of the mechanistically important regions without complications caused by the presence or absence of activators at an allosteric site.

While sequence comparison between TAO and SgAOX reveals that there is only ~30% sequence homology, homology modelling [161] demonstrates that the highly conserved residues remain spatially equivalent. Those amino acids that are conserved are predominantly located on the 4 helix bundle surrounding the di-iron core, with the unconserved region that can be seen in Figure 3.1 being part of helix 1 and the N-terminal arm. As such, the discussion around the conserved residues will be broken down into two sections; the core structure, which includes all residues that constitute the 4 helix bundle, and the predominantly unconserved regions, which consist of the N-terminal region and helix 1.

A number of crystal structures are available containing inhibitors of TAO, including colletochlorin B (PDB : 3W54) , an ascofuranone derivative (3-chloro-4,6-dihydroxy-5-[(2E,6E,8S)-8-hydroxy- 3,7-dimethylnona-2,6-dien-1-yl]-2-methylbenzaldehyde – PDB:3VVA) and ferulenol (unpublished data – kindly provided by Professor Kita, University of Tokyo). Examination of these crystal structures and comparisons to the uninhibited structure (PDB:3VV9) reveals features that are likely indicative of the effects of substrate recognition.

This chapter contains an extensive overview of the structure of the trypanosomal alternative oxidase, and examines the nature of the highly conserved regions of amino acids that can be found throughout the alternative oxidases.

3.2 AOX sequence alignment

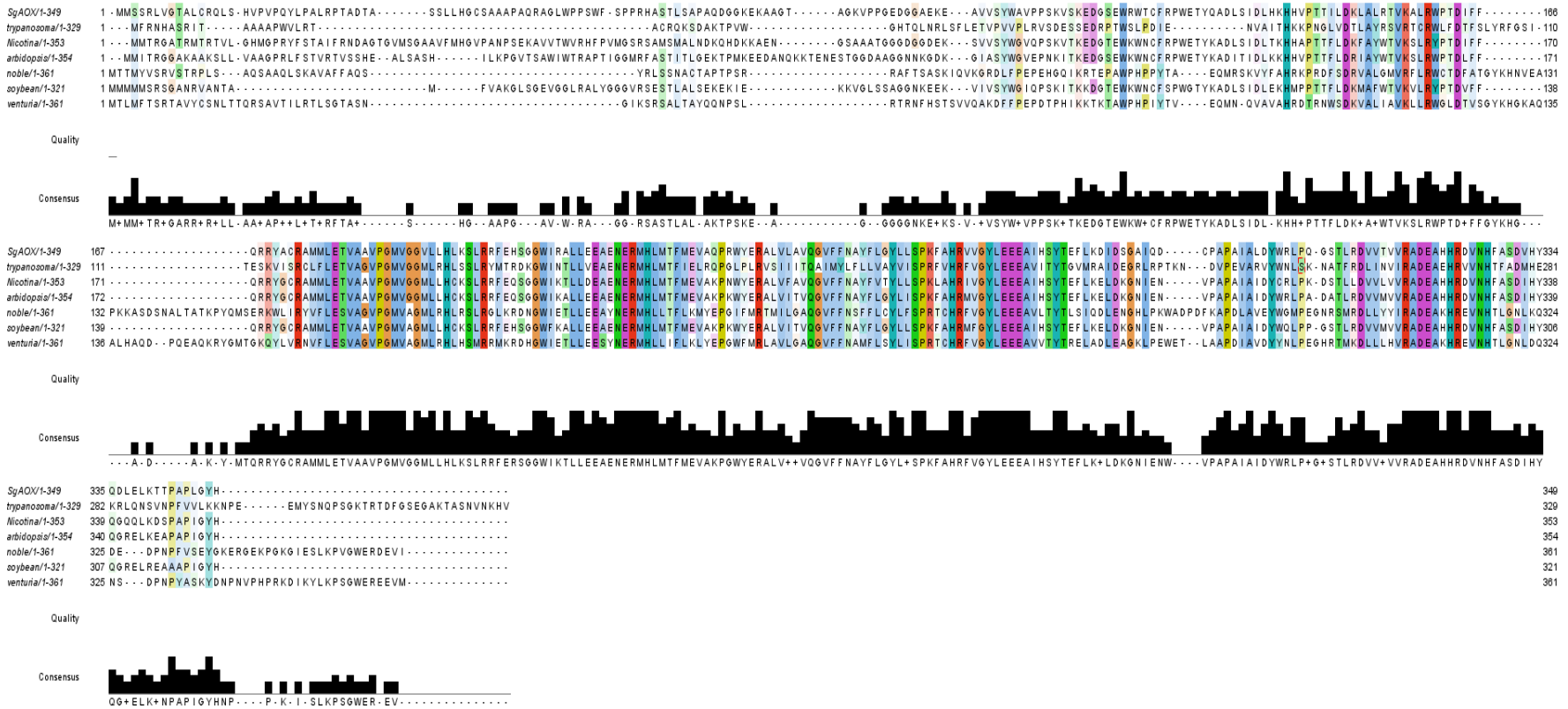

Figure 3-1:- sequence alignment of a cross section of known AOX species, including plant, trypanosomal and fungal . Sequences used in descending order: SgAOX (P22185), Trypanosoma brucei brucei (Q26710), Nicotiana tabacum (Q41224),Arabidopsis Thalina-AOX1a (Q39219),Botryontinia fucketliana-noble rot fungus (Q8NJ59),Glycine max soybean AOX1a (Q07185) Ventura inaequalis-apple scab fungus (Q9P429). Alignment performed using ClustalOWS algorithm, with colouring indicating regions of high conservation.

3.3 Roles of highly conserved residues based on crystal structure analysis

AA sequence	SgAOX numbering	TAO numbering	Region	role
W	118	65	N-terminal	
H	140	77	N-terminal	
D	148	85	Helix 1	
R	159	96	Helix 1	Substrate binding
D	163	100	Helix 1	Substrate bind
R	173	118	Helix 2	Substrate binding
LETVA	177-181	122-126	Helix 2	Varied
VPGMV	183-187	128-132	Helix 2	Varied
H	193	138	Helix 2	
SLR	196-198	141-143	Helix 2	Varied
GWI	205-207	150-152	Helix 3	Varied
L	210	155	Helix 3	
EA	213-214	158-159	Helix 3	
E	215	160	Helix 3	
NERMHL	216-221	161-166	Helix 3	
F	224	169	Helix 3	
P	230	175	Between 3 + 4	Interhelix bend
R	235	180	Helix 4	
Q	242	187	Helix 4	
Y	253	198	Helix 4	Interhelical binding
L	254	199	Between 4 and 5	
SPR	256-258	201-203	Between 4 and 5	Interhelix bend
HR	261-262	206-207	Helix 5	
GYLEEEA	265-271	210-216	Helix 5	Varied
YT	275-276	220-221	Helix 5	Redox active tyr
D	283	228	Helix 5	
G	285	230	Helix 5	
P	293	240	Between 5 and 6	
A	296	243	Between 5 and 6	
YW	299-300	246-247	Short helix	Structural
D	310	257	Helix 6	Structural
RADEA	316-320	263-267	Helix 6	Varied
HR	322-323	269-270	Helix 6	Iron ligating Histidine
VNH	325-327	272-274	Helix 6	Interhelical
P	343	290	C terminal	

Table 3-1:- Highly conserved amino acids throughout the sequence alignment, and their predicted roles within the structure based upon crystal structure analysis.

Table 3-1 contains a list of the highly conserved amino acids throughout the AOX family. One of the most prominent features from examination of the conserved residues within the structure is the lack of conservation within the membrane binding helices. Of the 71 conserved amino acids, only 6 of them are found in helix 1 and 4. (N.B. for discussion purposes, the TAO numbering will be used, with the SgAOX numbering included in the table as reference for Chapter 4. Within the discussion, residues and helices labelled with * signifies components from the neighbouring monomer)

The large groupings of conserved acids are consistent with those responsible for iron ligation, namely L**E**TVA, N**E**RM**H**L, GYL**E**EEA, RAD**E**A and the **H**R regions. Given the importance of the iron ligation system, it is unsurprising that these regions are responsible for ~40% of the conserved species.

The SLR region is found at the end of helix 2 and is a multifunctional region. S141 forms a hydrogen bond with R163 (of NE**R**MHL) to maintain the dimer formation between helices α2 and α3*. This bond is reciprocal at the other end of the protein, with identical bond formation between helices α2* and α3, effectively locking the helices together. The role of the R143 is less defined, given its location on the underside of the helix. There is potential for hydrogen bond formation to Q187 helix on α4*, but given the variability on the poses between monomers it is more likely that both amino acids are part of the membrane anchoring system for the protein. L142 is also of dual purpose, effectively capping the dimer interface with a hydrophobic residue, and locking the helix into place with the leucine at 166 from the NERMHL region.

The membrane face of helix 2 is coated with hydrophobic residues (valines 180, 183 and 187) that provide additional interaction with the mitochondrial membrane. While the conserved residues on helix 1 and 4 are mainly polar in nature and will bind directly to anchor points within the membrane, the valines are able to provide repulsion from the water layer upon the membrane, preventing the protein from dropping further into the membrane.

The conserved tyrosine towards the tail end of helix 4 is part of a hydrogen bond network spanning 4 helices. It appears that one of the main functions is for structural

stability, both maintaining the helical turn caused by P202 and stabilising the distances via hydrogen networks to H206, which is further stabilised by N273 (helix 6) and E158 (Helix 3). While a majority of amino acids have a highly conserved rotamic position, the terminal glutamate of this hydrogen binding network appears to be fixed in two positions perpendicular from one-another dependent upon monomer, and the location of the proximal crystallised water. It is tempting to speculate that this is a potential water channel away from the active site and into the water layer upon the membrane, given the flexible nature of the glutamate would allow for rotational movement to carry the water away from the di-iron centre.

H274 is the main focal point of interhelical interaction, forming hydrogen bonds the both R207 and E214, effectively locking the helices together. While Y211 is found within this region, it appears its role is to hold the histidine in place, effectively preventing movement towards helix 1.At the other end of the helix, a highly conserved H-bond is formed between T221 and R263. The high conservation of these residues tends to suggest that their role is stabilisation of the position of Y220 in the region of the active site. Given the position of this tyrosine, it is likely to be the redox active tyrosine, and will be discussed in detail in Chapter 6. The terminus of the interface is capped with the semi-conserved D228 R256 interaction, which is also interacting with E71 upon the short helix. While TAO is the only part of the AOX family to contain a carboxylate at this position, alcohol containing amino acids are used by other species that are likely to undertake the same role.

The YW pair on short helix 1 is being used to stabilise the histidines around the active site. Hydrogen bonding between Y246 and N161 orientate the helix to allow for an H-bond network to be drawn directly between W247 to the iron ligating H165 via D265. D265 is held in position by W65, a semi-conserved residue. This region is identical to that seen in RNR, where it has been identified as part of a proton coupled electron transport (PCET) network. Comparisons between the structures and their mechanistic implications are discussed in Chapter 6.

3.4 Membrane binding, dimer interface and N-terminal arm

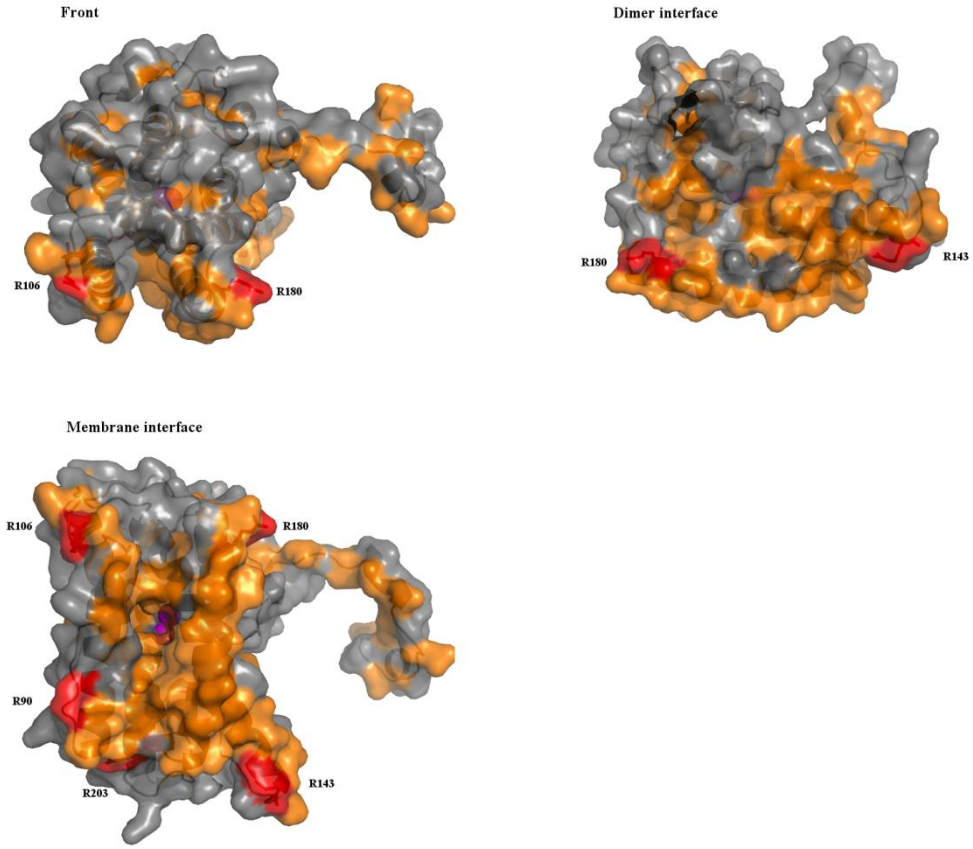

Figure 3-2:- Surface representation of a monomer from the TAO crystal structure, depicting the hydrophobic residues in orange. Membrane interface depicts the underside of the protein, and the di-iron core (magenta spheres) can be seen via the cavity. Residues coloured red are proposed to be responsible for membrane binding. N-terminal arm removed from dimer interface diagram for clarity.

The surface of the protein is largely hydrophilic, with the regions of hydrophobicity depicted as orange in Figure 3-2. As can be seen from the diagram, the underside of the protein is largely hydrophobic in nature, indicating that these residues are likely to reside under the polar headgroups of the phospholipid bi-layer.

The residues highlighted in red are proposed membrane binding residues, with an arginine on each corner of the protein anchoring the structure to the membrane. Of the residues highlighted for interacting with the phospholipid headgroups, R143,

R180 and R203 are all fully conserved. Q187 is also within the region of R180, but has a more ambiguous role. While it could potentially be used for membrane binding, it also appears to be forming a hydrogen bond to R143*, forming the corner for the dimer-interface.

The N-terminal arm precedes helix 1, and can be seen interlocking the two dimers together. This region is the least conserved among AOX's, with the sequence alignment demonstrating very few conserved residues, and coupled with the largely unstructured nature make links to amino acid function tenuous at best.

The crystal structure shows this section contains 3 short helices, with 1 helix interacting with each monomer and 1 residing in the interhelical domain. The first short helix is held in place by a hydrogen bond network formed between D228, R256 and E71. D228 can be seen hydrogen bonding to both the terminal NH_2 unit and the amine link of R256, which in turn binds to E71 on the short helix. Of these 3 residues only D228 is fully conserved, with R256 being relatively well conserved within the plant and trypanosomal species. Substitutions of E71 within other species conserve effective functionality, replacing the glutamate with serine and threonine in the plant and fungal species respectively. The retention of functionality within the side-chain and substitutions of shorter chain length is likely indicative of a requirement for tighter binding between the 4-helix bundle and N-terminal region in these species.

The second short helix can be seen in the dimer interface, and appears to be holding the position of the R163/S141 pair via a hydrogen bond to E57. Again while not fully conserved, the glutamate at this position is conserved in all plant and trypanosomal species. The more interesting feature within this area is the position of W65. As with the previously mentioned W247 it is within H-bond distance to D265, potentially allowing it to be part of the PCET network. Comparison to the homology model places W126 (SgAOX numbering) in the same region, which is fully conserved through the plant species. It is plausible that this would allow a total of 2 electrons to pass through this region into the core, but the second tryptophan is speculative given that its placement within the plant species could be incidental given the large number of tryptophans within this region (3 tryptophan residues can be found between aa118-126). The third helix is held in place by hydrogen bond

formation between S42 and D278*, and appears to be the only interaction between this region of the N-terminal arm and the second monomer.

3.5 Hydrophobic cavity

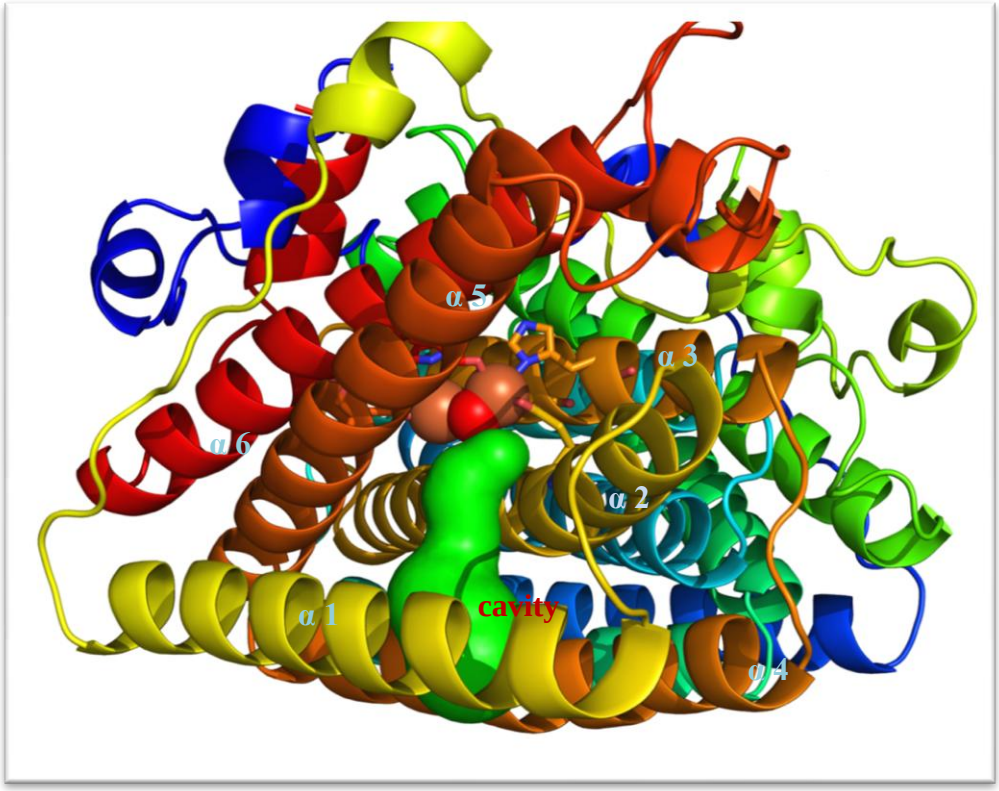

Figure 3-3:- Largest cavity generated using the CAVER software in the crystal structure of TAO (PDB code 3VV9), showing a cavity leading directly to the di-iron centre from between helices 1(yellow) and 4 (orange). Spheres in the centre represent the di-iron core.

CAVER [172] analysis revealed a number of tunnels leading through towards the di-iron centre, highlighting a number of pathways large enough for molecular travel. One of the main determinants of whether the tunnel is traversable for substrate is the size of the bottleneck within the tunnel, and the nature of residues lining the cavity. One of the more sizeable cavities is depicted in Figure 3-3. The cavity is located in underside of the protein between helices 1 and 4, with the surrounding residues being hydrophobic in nature. The cavity links the di-iron centre directly to the quinone

pool in the IMS, giving direct access to the quinol and reducing distance between substrates.

Given the lipophilic nature of the quinol tail section, a hydrophobic cavity would be necessary for substrate recognition (and indeed molecular orientation within the active site), as has been demonstrated with the cytochrome b_d and b_o quinol oxidases[173].

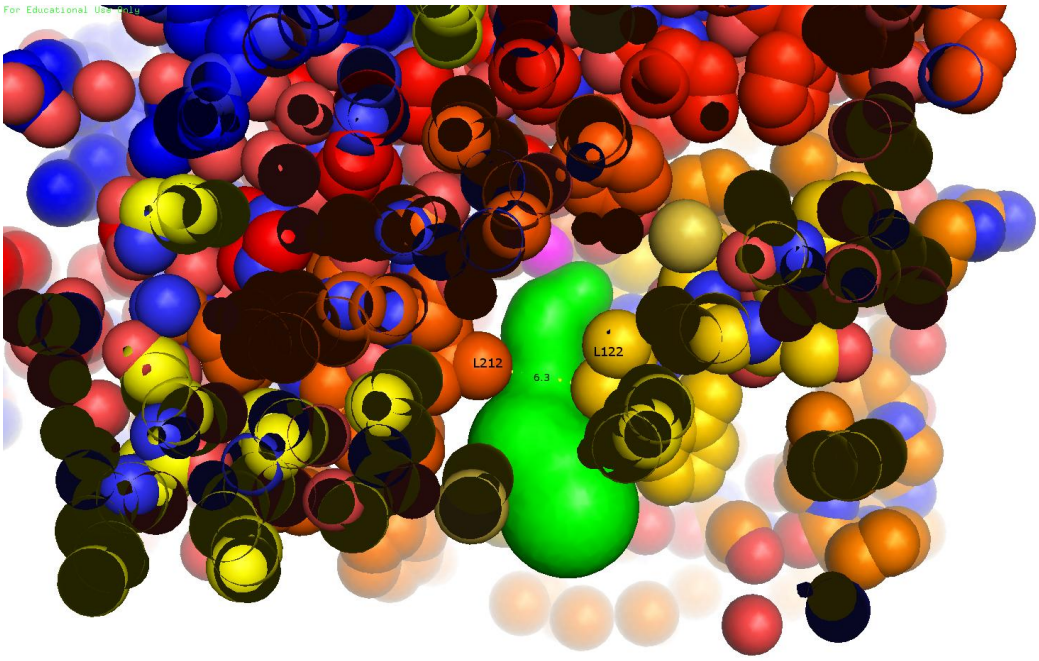

Figure 3-4:- Cross section of cavity showing the 6.3 Å bottleneck formed by the conserved residues L212 and L122 (TAO numbering). Magenta sphere in the background indicates that bridging Oxygen within the active site.

The bottleneck found between the highly conserved L122 and L212 is 6.3 Å in size (Figure 3-4), large enough to accommodate the passage of quinol (6.0 Å OH-OH diameter). While the tunnel lacks full conservation, the hydrophobic nature is still intact, with F99 being substituted by leucines and isoleucines, and F121 being replaced by methionine in the majority of cases. There is only one point of polar contact within the cavity walls at R96, which is conserved in all plant and trypanosomal species.

A crystal structure was also obtained containing Colletochlorin B within the hydrophobic cavity (PDB:3W54). While inhibitor binding within the site does not directly confirm the nature of the binding orientation as that of the substrate, the structural similarities between Colletochlorin B and quinol would suggest this is the most likely conformation. Docking studies performed demonstrated quinol is able to bind with the head group occupying the same space as that of the inhibitor within the crystal structure, with varying degrees of tail positions available with little degree of variation in the final fit score.

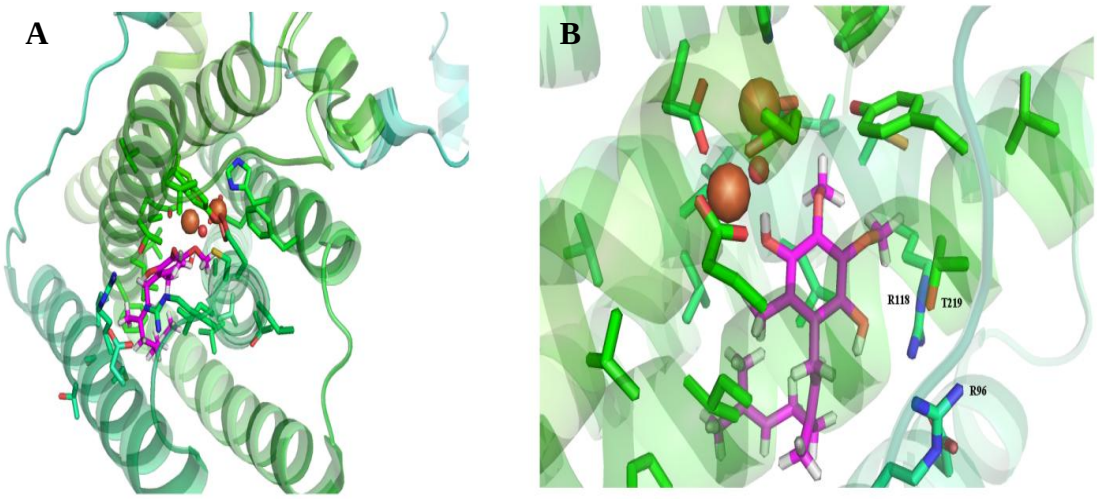

Figure 3-5:- Docking of quinol into the active site (PDB:3W54) with the highest score obtained (z=-8.6). Picture A shows position of quinol tail, conforming to the same spatial region as that of the hydrophobic pocket from CAVER analysis. B depicts the head group of the quinol, with 1-OH interacting with T219 and R118, and 4-OH interacting with the di-iron centre.

Figure 3-5 depicts quinol within the hydrophobic pocket. The key interactions with the protein occur at 1-OH, with hydrogen bond formation to T219 and R118 (heteroatom distances of 3.2 Å and 3.7 Å respectively). 4-OH is seen to be interacting with the di-iron hydroxyl bridge, with an O-O distance of 2.7 Å. The second anchor point is interesting from a reactivity standpoint, as without the di-iron

hydroxyl group the quinol would be unlikely to dwell within the active site. This would suggest that the di-iron centre has to be in the correct part of its oxidation cycle for reaction with quinol, and that quinol does not dock with the protein and wait for the oxidation cycle.

Crystal data obtained with an ascofuranone derivative within the active site (unpublished data professor Kita, University of Tokyo) indicated that there was a separate cavity orthogonal to the hydrophobic cavity, lying between helices 1 and 5. While from the internal area of the protein the cavity is still there, it lacks access to the protein exterior. While it is possible that a conformational change would accommodate the opening of the passage, membrane modelling (Dr. C. Elliott, unpublished results) would place the opening along the membrane surface, providing a non-ideal approach for quinol. This second tunnel could potentially act as an exit system for either quinol or water, providing an alternative route out of the active site.

3.5.1 Water transport

The smaller tunnels have the potential to be part of a water transport network, given that the product of enzymatic reaction is two molecules of water facilitation of their removal would allow for continued turnover. While the water may be a necessity for reaction with the quinol, facilitation of removal from the active site will be a necessity once the reaction has been completed.

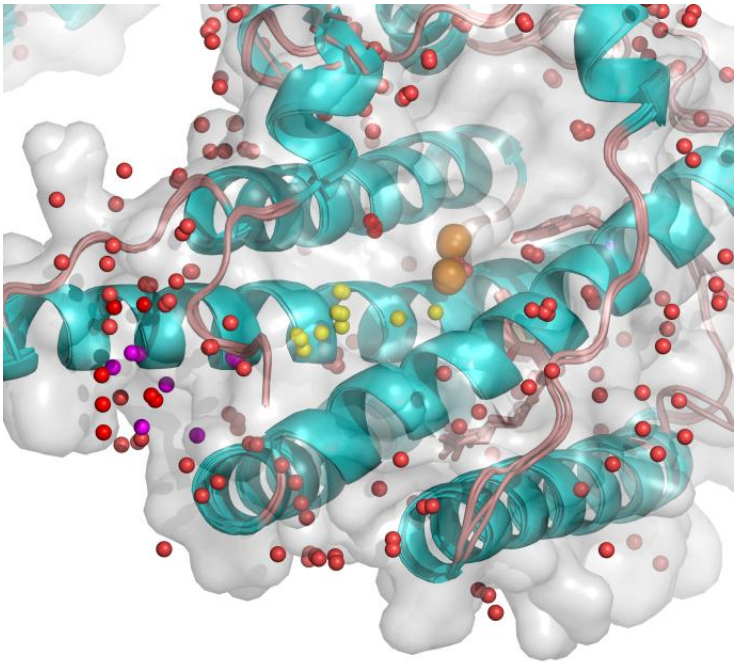

Figure 3-6:- water distribution throughout the crystal structure, shown with the 4 monomers of AOX inhibited with colletochlorin B overlaid (PDB: 3W54). Yellow spheres denote water within the structure, red spheres are water on the surface, and iron is shown as orange spheres in the centre. Helix 6 removed for clarity.

Examination of the crystal structure allows for confirmation of water channels, and when combined with the CAVER data of potential tunnels within the crystal allows verification of their purpose. While the water distribution throughout each monomer is erratic, overlaying the monomers shows highly concentrated pockets of water. A majority of the water molecules within the crystal are ligated to the surface of the protein, but a cluster of internal water molecules can be seen running alongside the interior of helix 2 (depicted as yellow spheres in Figure 3-6). A potential outlet from the protein has been highlighted as purple spheres, but given the small size cavity it is impossible to define these as water from the active site and could be a factor of crystallisation around the protein.

Of the 9 residues within ligation distance of the crystallised water, 8 are fully conserved, including a number that were not included in the section 3.3., namely I152, L155 E158,Y198 and H206. There are two possible functions for this tunnel; it could either be used to shuttle water away from the active site to allow for faster

catalytic turnover, or potentially as a proton delivery network towards the core. The former is the most likely scenario, given that each monomer only contains 2 or 3 water molecules each that would not constitute a full proton transfer network. The pKa values determined from the PropKa experiment [174] demonstrate a directional raise in pKa from the di-iron centre to Y198, from 2 to 12, which would direct protons towards the tyrosine. There is a potential second entrance to this channel from the W46 region that would facilitate proton transfer along the pKa gradient, but given the short distance between channel and solvent it could be an artefact of crystallisation and therefore cannot be given a definitive role.

3.6 Ligation around the di-iron sphere – uninhibited structure

As predicted by structural models [136], the ligation sphere around the di-iron core under oxidised conditions consists of two bridging glutamates (E162 and E266), two glutamates binding in bi-dentate fashion, with one ligating to each iron (E123 and E213), and two histidines (H165 and H269). The glutamates are arranged in such a way that each helix contains an iron binding ligand, cementing the remainder of the structure around a fully functional active site.

Monomer	**E123 (Fe2/Fe2)**	**E162 (Fe1/Fe2)**	**E213 (Fe2/Fe2)**	**E266 (Fe1/Fe2)**	**H165**	**H269**
A	2.2 / 2.0	2.3/2.1	2.2/2.0	1.8/2.2	3.3	3.8
B	1.9/2.1	1.9/1.8	2.2/1.8	2.2/2.5	3.4	3.8
C	2.2/2.0	2.5/2.3	2.3/2.5	2.0/2.1	3.3	4.4
D	2.4/1.9	2.5/1.9	2.3/2.0	1.8/2.1	4.0	4.3

Table 3-2:- distance measurements for the primary iron ligation sphere. All measurements taken in Angstroms. Measurements taken between heteroatoms and the iron. Two numbers indicate bidentate binding, with iron definition defined in the column heading. Measurements made using PyMOL.

As can be seen in Table 3-2, binding distances between glutamates and irons have modest variability, with the exception of E213 and E266 bonds to Fe2 in monomer

B. The more interesting feature of the iron ligation sphere is the lack of ligation to the histidines.

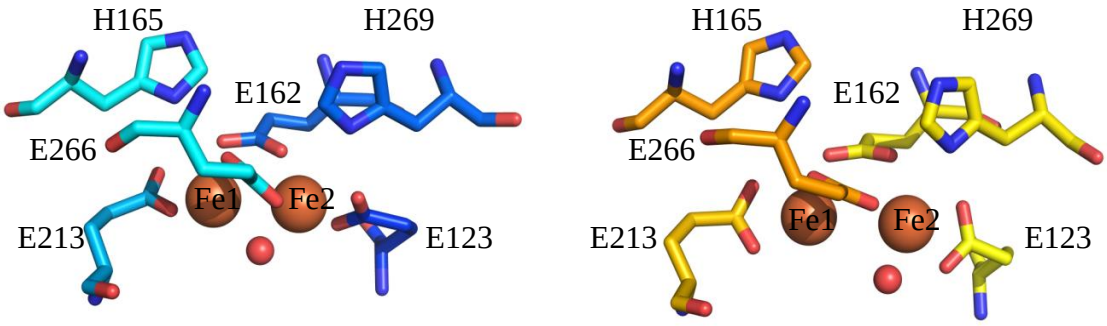

Figure 3-7:- di-iron core of TAO (PDB:3VV9) from different monomers . Cyan figure on the left is monomer A, with the yellow on the right is monomer B. Large orange sphere corresponds to iron, with the small red sphere corresponding to oxygen.

Monomer	Fe(1) – Fe(2)	Fe(1) – O	Fe(2)-O
A	3.0	2.5	2.1
B	3.0	3.1	2.2
C	3.5	3.7	2.0
D	3.4	3.2	2.1

Table 3-3:- Interatom distance measurements from TAO crystal structure (PDB:3VV9). All measurements taken in Angstoms, with Fe(1) being defined as that ligated by E213 , and Fe(2) by E123. Measurements made using PyMOL.

Figure 3.7 demonstrates the typical arrangement of the primary ligation sphere around the di-iron core. Of note is the perturbation in the iron location between monomeric units. While the position of Fe1 seems extremely well defined in space, Fe2 migrates ~0.5 Å further from Fe1 in monomers C and D, a 17% increase in inter-iron distance. The effects of this can be seen in the arrangement of the ligating hydroxyl group, conferring a mono-dentate ligation to Fe2 instead of the bridging species that can be seen on monomer A, with Fe1-OH distance of 3.7 Å large for interaction.

3.7 Comparison between inhibited and uninhibited structures

Comparisons between the inhibited and uninhibited crystal structures allows for examination of the effects of molecular binding upon the active site. Colletochlorin B has similar structural motifs to that of quinol, and therefore will give a reasonable indication of the interaction between the binding site and substrate. While a majority of the structures have been published, the structure containing ferulenol, a recently discovered competitive inhibitor of AOX, was kindly provided by Professor Kita for analysis.

3.7.1 Binding positions for inhibitors

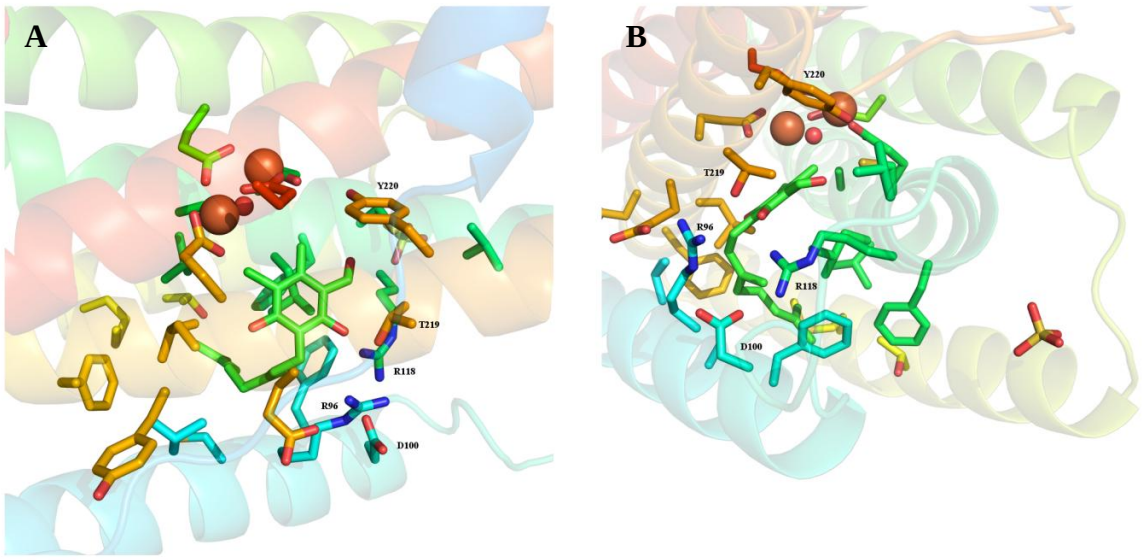

Figure 3-8:- Binding of Colletochlorin B (PDB:3w54). Amino acids shown are those within 6 Å of the inhibitor, with labelled amino acids indicating potential interaction with the inhibitor. Figure A depicts the head group interactions with the protein, with 2-OH within hydrogen bond distance to T219, R118 and R96. Figure B depicts the location of the isoprenoid tail.

Colletochlorin B has few points of contact with the protein itself, which is surprising given the highly substituted nature of the head group. The main interaction appears to be the 2-OH, within hydrogen bond distance to both T219 (2.5 Å) and R118 (2.6

Å). A potential hydrogen bond can also be seen between the aldehyde and C119. Further refinement of the crystal structure has suggested that the inhibitor is able to rotate along the axis, with 2-OH and 4-OH effectively exchanging positions. Orientation in this manner would be more in line with SAR studies performed that suggested the 4-OH position was more significant for inhibition of TAO then 2-OH [115] . This would also place the aldehyde within H-bonding distance to Fe-OH, effectively adding a second anchor point (and therefore more stable binding) for the inhibitor.

Monomer	**E123 (Fe2/Fe2)**	**E162 (Fe1/Fe2)**	**E213 (Fe2/Fe2)**	**E266 (Fe1/Fe2)**	**H165**	**H269**
A	2.1/2.1	1.9/2.0	2.1/2.3	2.3/1.9	2.4	4.1
B	2.2/2.3	2.1/2.0	2.4/2.1	2.2/2.3	2.6	3.9
C	2.2/2.2	2.1/2.9	2.3/2.2	2.0/1.8	2.3	4.5
D	2.3/2.2	2.0/2.0	2.1/2.2	2.2/2.1	2.4	4.1

Monomer	**Fe(1) – Fe(2)**	**Fe(1) – O**	**Fe(2)-O**
A	3.5	1.9	2.2
B	3.3	2.2	1.7
C	3.5	2.3	2.1
D	3.2	2.3	1.9

Table 3-4:- ligation around colletochlorin B inhibited di-iron core (PDB:3W54). All measurements taken in Angstroms. Measurements taken between heteroatoms and the iron. Two numbers indicate bidentate binding, with iron definition defined in the column heading. Measurements made using PyMOL.

One of the more prominent effects of inhibition is the rotation of a portion of helix 1. Once bound to the inhibitor, R118 also forms a new hydrogen bond with D100, causing rotation in the position of R106. Given the assignment of R106 as a potential membrane binding residue, this implies that binding of the substrate within the active site causes a conformational change that would lower the effective binding to the membrane. It is also possible that this rotation is a feature of crystal preparation, and that either position is the correct orientation. R106 is also important within the second hydrophobic cavity proposed by Shiba *et.al.* (2013)[11], as the rotation in the inhibited structure blocks entrance to the second cavity. C199 also demonstrates

independent rotation towards the inhibitor, causing modest change in the helix itself. It is worth noting that the cysteine is not a conserved residue, and that interaction does not necessarily implicate it as the main binding point within other AOX species, but the position of a potential radical carrier in close proximity to the proposed redox active tyrosine is unlikely to be coincidental.

Monomer	E123 (Fe2/Fe2)	E162 (Fe1/Fe2)	E213 (Fe2/Fe2)	E266 (Fe1/Fe2)	H165	H269
A	2.1/2.5	2.1/2.0	2.5/2.4	2.2/2.1	2.2	4.4
B	2.4/2.1	2.3/2.0	2.2/2.3	1/9/1.9	2.5	4.2
C	2.3/2.4	2.0/2.0	2.3/2.1	2.2/2.2	2.3	4.0
D	2.3/2.2	2.4/2.4	2.6/2.2	2.1/1.9	2.3	4.5

Monomer	Fe(1) – Fe(2)	Fe(1) – O	Fe(2)-O
A	3.8	1.8	2.4
B	3.1	2.3	2.1
C	3.5	2.4	1.8
D	3.7	2.4	2.1

Table 3-5:- Ligation around the 3-chloro-4,6-dihydroxy-5-[(2E,6E,8S)-8-hydroxy- 3,7-dimethylnona-2,6-dien-1-yl]-2-methylbenzaldehyde inhibited core (pdb:3VVA). Measurements made using PyMOL

The data in Table 3-4 and Table 3-5 gives the iron ligation distances in the 3W54 and 3VVA structures respectively. Given that the difference between these two inhibitors is at the extremity, it is unsurprising both active sites have similar architectures. When compared to Table 3-2 the largest difference that can be seen is the lower H165 bond distance, indicating that the presence of an inhibitor within the cavity has caused a migration of the iron.

Inhibitor binding – orthogonal cavity

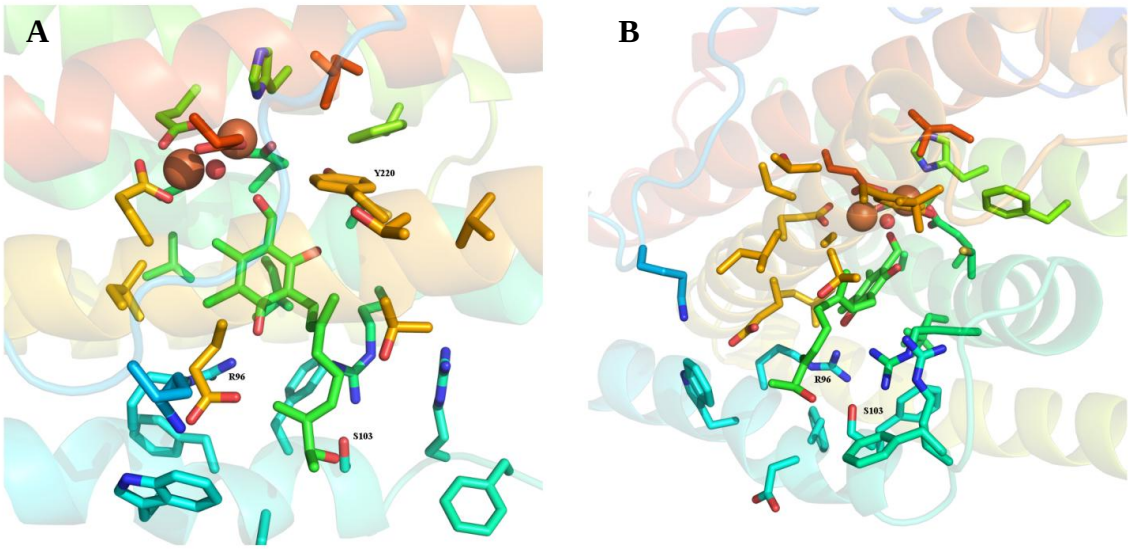

Figure 3-9:- Binding of 3-chloro-4,6-dihydroxy-5-[(2E,6E,8S)-8-hydroxy- 3,7-dimethylnona-2,6-dien-1-yl]-2-methylbenzaldehyde via the orthogonal cavity. Potential Hydrogen bond acceptors for the benzaldehyde ring R96 and Y220 marked and depicted in figure A. Figure B depicts the interaction of the terminal OH and S103. Amino acids shown all within a 6 Å radius of inhibitor.

Monomer	E123 (Fe2/Fe2)	E162 (Fe1/Fe2)	E213 (Fe2/Fe2)	E266 (Fe1/Fe2)	H165	H269
A	1.9/2.4	2.1/2.1	2.5/2.5	2.0/1.9	2.1	4.2
B	2.2/2.5	2.0/1.8	2.0/2.5	2.3/2.0	2.6	4.1

Monomer	Fe(1) – Fe(2)	Fe(1) – O	Fe(2)-O
A	3.2	1.8	1.8
B	3.1	1.8	1.8

Table 3-6: Ligation around the inhibited core where the inhibitor approaches from the orthogonal cavity.

A second crystal structure of the ascofuranone analogue from 3VVA was also made available for analysis. This structure shows the inhibitor within the second cavity between helices 1 and 5, and demonstrates different binding properties to those of the published crystal. Within this crystal, the inhibitor is forming hydrogen bonds between 4-OH and R96, and 2-OH and C119. The increase in angle caused by the

second binding point has raised the profile of the aldehyde to be placed inbetween Tyr-220 and Fe2 (distances Tyr-OH – O 3.7 Å, Fe(1)-O 3.2 Å).

The crystal structure shows more extreme rotation along helix 1, with displacement of residues constituting a full helical turn. The same cannot be seen on helix 5, with reasonable alignment shown between residues, giving credence to rotation of helix 1 being due to inhibitor binding. A necessitation for helical rolling as part of the substrate binding mechanism could potentially explain the lack of membrane binding residues in this region of the structure, given that each other corner of the protein underside is firmly fixed to the membrane.

Ferulenol

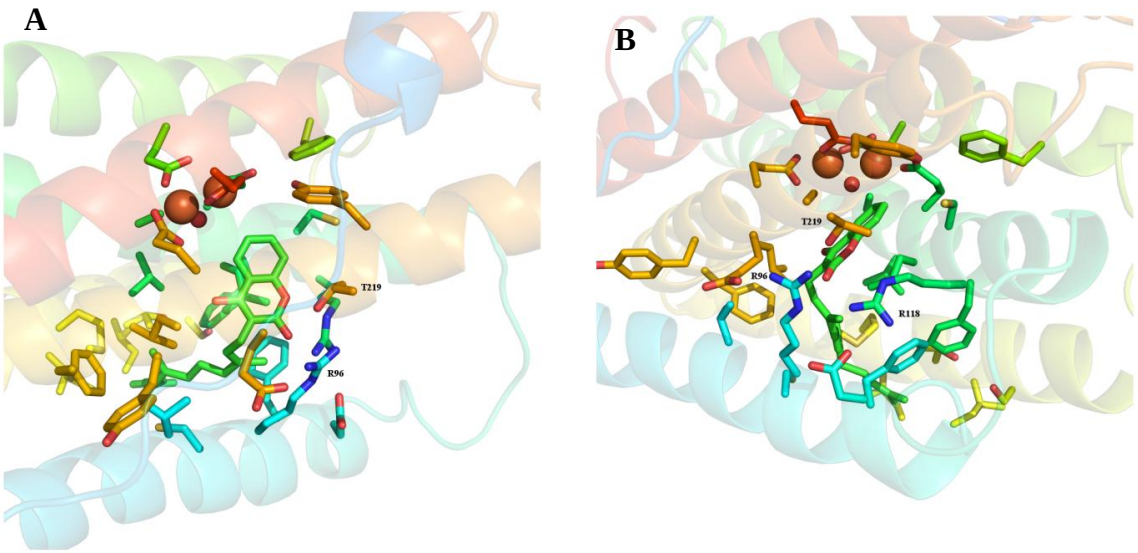

Figure 3-10:- Binding of ferulenol within TAO. Key binding residues are labelled, with the di-iron core shown as spheres. A and B give views of the pharmacophore and tail respectively.

Ferulenol is unique among the inhibitors, in that it demonstrates purely competitive inhibition with respect to ubiquinol (Dr. D. Inakoa, University of Tokyo, unpublished observations). As such it allows for direct conformation that the space in which it is residing would be that occupied by the quinol. The crystal structure shows binding similar to that seem in the quinol docking experiments in section 3.5, with the carbonyl within hydrogen bond distance of T219, R96 and R118 (3.6 Å, 3.3

Å and 2.7 Å respectively) and additional potential interaction between the ring oxygen and the R118 amine.

Monomer	E123 (Fe2/Fe2)	E162 (Fe1/Fe2)	E213 (Fe1/Fe1)	E266 (Fe1/Fe2)	H165	H269
A	2.4/2.7	2.0/2.1	2.3/2.3	2.1/2.0	2.1	3.9
B	2.2/2.3	2.0/2.4	2.1/2.4	2.3/1.9	3.1	4.2
C	2.3/2.2	1.7/2.7	2.1/2.1	2.2/2.2	2.9	4.5
D	2.7/2.0	1.8/2.6	2.2/2.4	1.9/2.0	3.4	3.6

Monomer	Fe(1) – Fe(2)	Fe(1) – O	Fe(2)-O	Fe(1) – H_2O
A	4.2	2.2	2.6	2.9
B	3.3	2.0	2.1	2.9
C	3.3	2.0	2.3	
D	3.3	2.1	2.1	

Table 3-7:- Ligation around the inhibited core with ferulenol in the active site.

Within all inhibited structures, the iron atom positions have improved definition over their uninhibited counterparts, which could demonstrate a degree of interaction with the inhibitor, or is alternatively a feature of improved crystal resolution allowing for better spatial alignment of the metal centre. The position of the ligating OH is also more conserved, adopting a consistent bridging position between the irons in all cases examined. The mode of inhibition appears to be unimportant with respect to changes within the core; both competitive and non-competitive inhibitors display the same adaption to molecular interaction within the cavity.

3.8 Summary

While this chapter has covered a fairly exhaustive list of conserved amino acids within the AOX family, it does not necessarily encompass all residues that may be responsible for functionality. This can be seen clearly in the case of C199, whereby rotation would indicate a degree of interaction with the inhibitor.

The interaction of the N-terminal arm is a region that could likely be better defined once crystal structures are available of other AOX's. While it does have a number of binding points to both monomeric units, its function appears to be solely for placement of the second tryptophan into the PCET network. It is likely to also have secondary functionality as an effective covering on the core helix bundles, with both N-terminal regions running parallel across the dimer. It is interesting to question what effect this would have on the activity of the monomer, as while the position of the typtophan is fixed by first two shorter helices to the monomer, the rest of the N-terminal region could potentially add kinetic strain onto this coupling if it is not stabilised by the second TAO unit. The hydrophobic nature of the dimer interface would suggest that the protein would be highly unstable in its monomeric form. It has been demonstrated within the lab that the N-terminal region is vital for activity, as truncation of this region confirming that it does indeed play an important role within the protein (Dr. M. Albury, unpublished observations).

Comparisons of the inhibited and the uninhibited structures have revealed a number of facets that are indicative changes upon substrate binding. The alterations to the di-iron core structure could indicate changes that would occur upon the approach of quinol, or it could also be an indication of an intermediate if a proton or electron has been transferred from the inhibitor to the protein. The movement of helix 1 could also indicate a co-operative binding mode for the quinols, with a second cavity opening once the first is in place. As was previously discussed, this second cavity is debateable, with it only being accessible in a select few monomeric units, and the placement of the opening outside of the intermembrane space would make access to the quinone pool difficult.

4 Expression of recombinant AOX and mutants in haem-deficient *E.coli*

4.1 Introduction

Site directed mutants have been a key facet in understanding the structure function relationship of highly conserved amino acids within proteins. A number of mutants of both SgAOX [138, 157, 175] and TAO [140, 141] have been expressed in both *S. pombe* and *E. coli*, confirming that structural features such as the iron binding motifs and tyrosines that are important for enzymatic activity.

The electron transport chain of *E. coli* differs from those previously discussed in Chapter 1. While the overall function still produces a proton gradient for driving ATP synthesis, *E. coli* lacks complexes III and IV, instead using the terminal cytochrome oxidases b_d and b_o. Like AOX, both cytochromes catalyse the reduction of oxygen via the oxidation of two equivalents of quinol, with cytochrome b_o being expressed at times of high oxygen concentration [176] and cytochrome b_d under anoxic conditions and lag phase growth [177].

FN102 has previously been used to express TAO from *T.vivax* [178] and *T.b.brucei* [160]. The strain lacks glutamyl-tRNA reductase [160], removing its ability to synthesise haem for use in the cyctochrome b_d and b_o complexes, therefore lacking terminal oxidases. Growth of the *E. coli* consequently relies on the successful integration of AOX into the membrane for the survival of the cell. The use of the FN102 strain allows for a greater degree of overexpression relative to more conventional strains for expression of membrane bound protein (such as strain C41) due to the dependency on the *E. coli* on AOX for continued respiration.

The use of an *E. coli* based system proves advantageous over expression within *S.pombe* as it allows for more facile membrane isolation and protein purification. Isolation of the membrane removes cytosolic proteins, reducing the number of contaminants for potential unwanted substrate interaction while simultaneously

increasing the accuracy of protein estimations, and therefore calculated specific activities.

4.1.1 Mutants

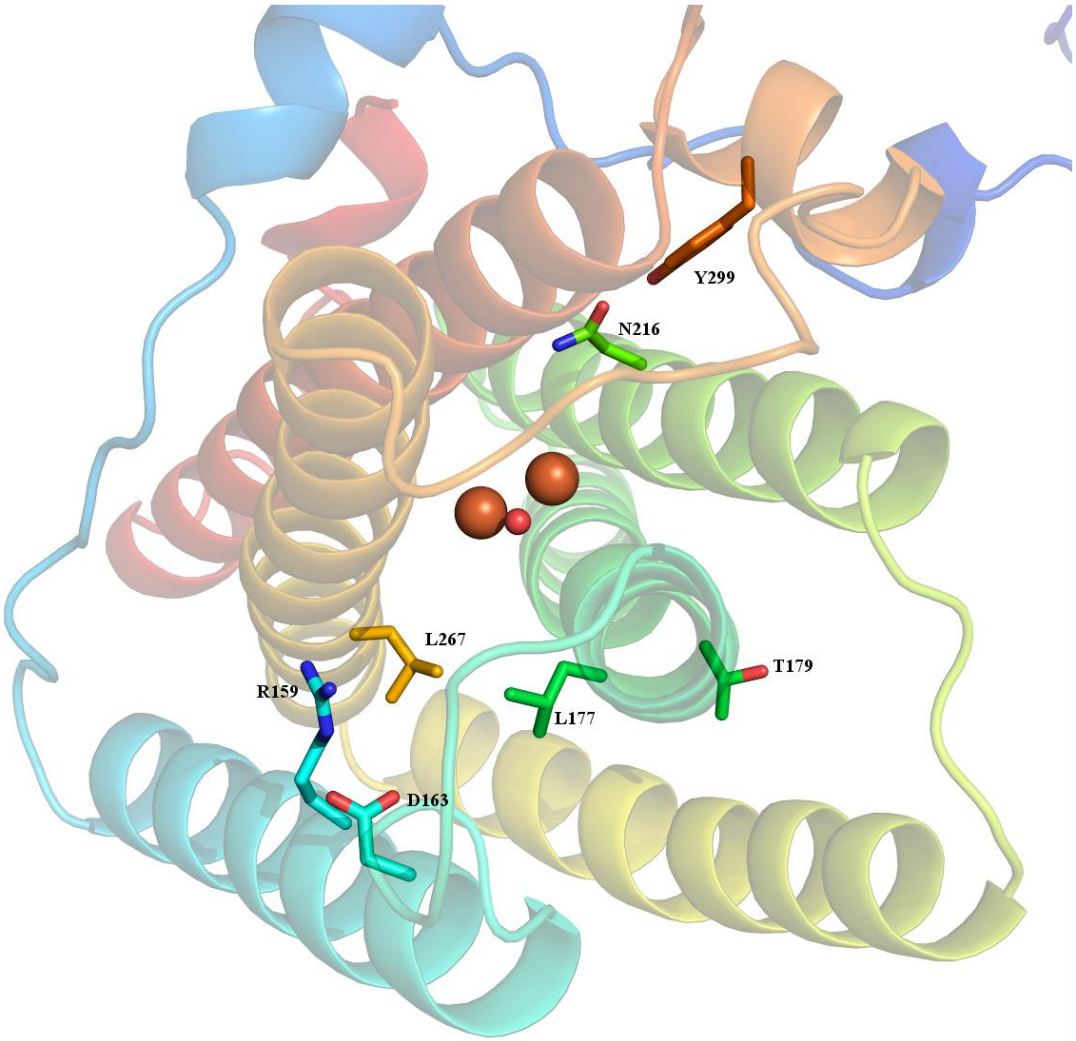

Figure 4-1:- Positions of the mutants studied within the TAO structure. SgAOX numbering used for reference, with the di-iron core shown in the centre as spheres.

The conserved amino acids that were mutated and are subsequently discussed within this chapter are depicted in Figure 4-1. L177A and T179A flank the iron ligating glutamate, and while the side chains both perform different roles, alteration of this highly conserved region is likely to cause perturbation within the di-iron core. T179A has been proposed to be part of the dimer interface, forming hydrogen bond

to the carbonyl within the backbone of L142. While not fully conserved, its only substitution is by serine in the fungal species. Given the retention of the alcohol moiety, the addition of the methyl group of threonine is unlikely to affect interactions with the dimer interface. It is more likely that the addition of steric bulk adds a directional component to the alcohol, preventing rotation toward the helix. L177 is part of the bottleneck within the hydrophobic cavity alongside L267, and mutation to alanine removes the bulky isobutyl side chains, potentially widening the channel while retaining hydrophobic character.

Y299 and N216 are part of the highly conserved hydrogen bonding network that was proposed in chapter 3 to maintain the position of W300. Conversion of the tyrosine to phenylalanine removes the phenolic hydroxyl group, while retaining the phenol ring, allowing for assessment as to whether the hydroxyl or phenol section of the amino acid are important for enzymatic function. N216 is the other end of the pair, forming a hydrogen bond with Y299 in order to hold W300 in place. As with L177, N216 is adjacent to an iron binding glutamate, therefore could also influence the di-iron core.

D163 and R159 are part of the proton bonding network between helicies 1, 2 and 5 that were highlighted in chapter 3 for their role in the proposed quinol binding site. R159 forms hydrogen bonds with E220 and S274 (2.5 Å and 3.1 Å respectively), whereas D163 bonds to R173 with a distance of 2.4 Å.

4.2 Growth and harvest of the *E. coli* membrane

Transformation and growth of the *E. coli* was performed as described in Chapter 2. Growth curve analysis using OD_{600} measurements prior to induction with IPTG indicated that there was no dependence on AOX mutation, with an average doubling time of 0.9 hours found across all mutations indicating that the cells were able to grow sufficiently prior to being rescued via AOX expression.

Association of mutant and wild type AOX to the membrane was confirmed via western blot analysis (Figure 4-2). There appears to be no visible preference between monomer (32kDa band) or dimer formation (~64kDa) for wild types or mutants. It is

worth noting that while dimers are visible, it does not necessarily mean they are in the deactivated dimer form (i.e. dimerisation *via* the cysteines), with dimerisation possible *via* ionic interaction along the dimer interface discussed in chapter 3.

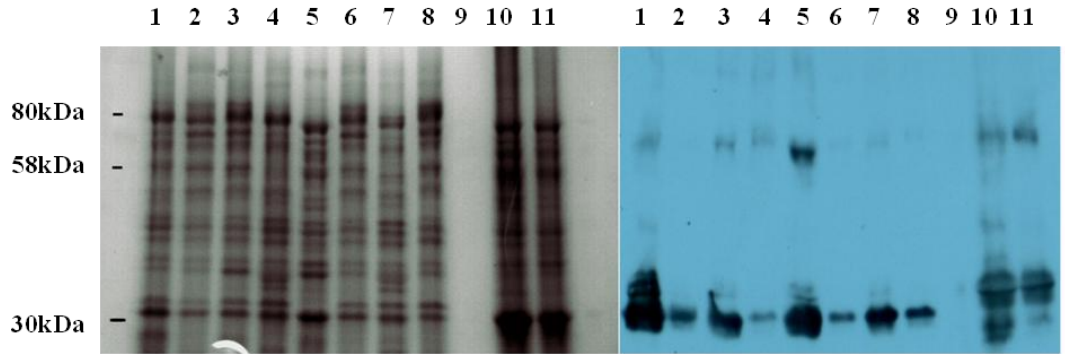

Figure 4-2: SDS-page (left) and western blot (right) analysis of mutants of AOX and TAO. All lanes loaded with 15ug of protein from membrane fractions, with gels run as described in Chapter 2, with western analysis performed using an antibody raised against AOX. Tracks from left to right show :- 1-SgAOX wild type, 2-R159A, 3-D163A, 4-L177A, 5-T179A, 6-N216A, 7- L267A 8-Y299F,9-blank, 10-TAO, 11-T124a (TAO mutant)

Figure 4-2 are representative SDS-page and western gels of each mutant generated. Each membrane bound sample contains a band in the western at ~32kDa, corresponding to AOX monomer. Each lane was loaded with 15ug of protein; therefore the difference in band luminescence correlates to the concentration of AOX within the membrane sample. The bands visible at ~64kDA correlates to AOX dimer formation, with oligomers visible at higher molecular weights in lanes 1,3,4 and 5. While the darker bands visible for the TAO preparations would suggest that they have improved expression over the plant variant, they are not directly comparable due to differences in concentration of IPTG used for induction. It was found that while 25 µM IPTG was sufficient for growth of rSgAOX and mutants, rTAO was unable to sustain *E. coli* growth at concentrations less than 100 µM IPTG.

Efficacy of the membrane preparation was confirmed via western blot analysis, with the French Press cell debris pellet containing low levels of AOX, and undetectable levels remaining within the ultracentrifugation supernatant (data not shown). The low levels remaining within the cell debris can be attributed to unbroken cells. While this could be remedied by increasing the number of passes through the French Press,

it would be detrimental to the overall membrane quality due to the increased time that the protein would be in contact with proteases within the cell lysate.

4.3 Membrane bound respiratory measurements using NADH

Mutation	Specific activity nmols O_2 min^{-1} mg^{-1}	Relative activity %	Number of isolations
rSgAOX	230 ± 56	100	6
T179A	66 ± 36	28	3
D163A	72 ± 12	31	3
R159A	56 ± 19	24	3
Y299F	74 ± 40	32	3
N216A	54 ± 4	23	3
L177A	118 ± 32	51	2
L267A	94 ± 3	41	2

Table 4-1:- Mean specific activity values ± standard deviations of rSgAOX mutants in membrane form from replica assays. Assays were carried out using an oxygen electrode containing 400 µL 50mM TRIS-HCl pH 7.4, 10mM pyruvate, 4 µM antimycin A with 1.25mM NADH as the substrate. Activities were compared and expressed as a percentage of wild type activity, with the number of samples run given.

NADH dependant oxygen uptake for membrane bound wild type (rSgAOX) and mutants are presented in Table 4-1. All samples were preincubated with antimycin A in order to inhibit any potential cytochrome contaminants within the ETC, ensuring that data collected is a direct result of AOX activity. Measurements were collected using an oxygen electrode to determine oxygen uptake of the *E. coli*, with an excess of NADH added to maximise reduction rates of the quinone pool and addition of pyruvate to ensure the protein was in its active form. All mutants demonstrated significant decreases in activity when compared to that of the wild-type activity.

The Y299F and T179A mutants allow for internal controls for comparison between this study and those performed on *S. pombe* mitochondria, with similar activity percentages for each, giving values of 44% and 40% reduction in specific activity

levels respectively [175]. While the data agrees statistically, this is likely indicative of the large standard deviation around the mean in this study.

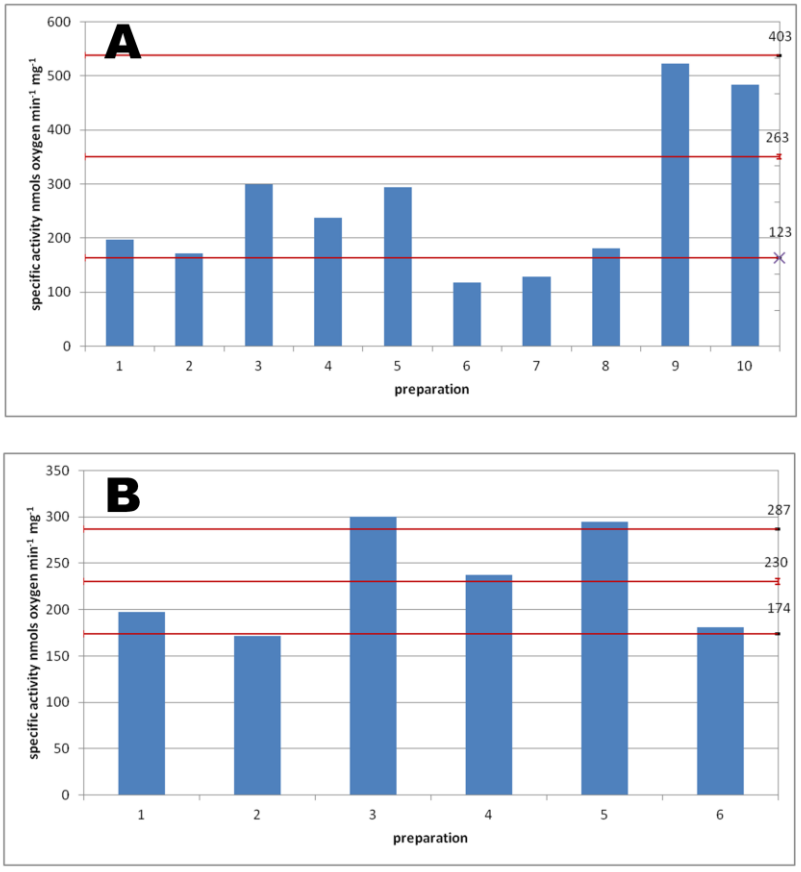

Figure 4-3- graphical representation of the variability in membrane bound specific activity. Bars represent specific activity of rSgAOX membrane samples, with horizontal lines representing mean average +/- standard deviation respectively. Graph A contains all preparations, whereas graph B shows the data with the outliers removed (preparations 6,7,9 and 10 from graph A). Averages and standard deviations are 263 ± 140 and 230 ± 56 respectively.

The large variation found with oxygen uptake is demonstrated in Figure 4-3. While the averages of 263 and 230 nmols O_2 min^{-1} mg^{-1} do not vary wildly between the 10 sample and the 6 sample mean averages, the lower standard deviation in the latter gives a more accurate value. There are a number of factors that could contribute to sample variability, not limited to the overexpression of the protein being independent of the existing electron transport chain (i.e. the expression of alternative oxidase is dependent on available sources of iron and amino acids rather then stochiometrically linked to the NADH dehydrogenase). If AOX is expressed to a level where the

reduction level of the quinone pool cannot reach optimal conditions for AOX activity then activity measured will be not be representative of the true V_{max}.

It was found that an addition of duroquinol increased activity of the protein, indicating that the quinone pool is the cause of deviation. Disruption of the membrane via French Press during the harvesting procedure could lead to a loss in internal quinol, making quinol concentration the limiting factor. To mediate this initial rates were taken as opposed to steady state measurements, as measurements taken at a constant rate would be dependent upon both the quinone pool redox poise and the total concentration of quinols. It is also possible that the quinone pool within the *E.coli* membrane was problematic for AOX; the quinone pool for *E. coli* favours a mixture of menaquinones and demethylmenaquinones once cytochrome b_d is expressed [179], and given the overnight growth it is likely that this had occurred.

While this is the case with the wild type expression, it can be seen (with the exception of Y299F) that introduction of a mutation into the protein structure reduces variability within the respiration rates. This would suggest that alternative oxidase turnover for the mutants have become rate limiting, allowing for more accurate determination of specific activity under otherwise non-ideal conditions.

4.4 TAO and SgAOX comparison

Mutation	Specific activity nmols O_2 min^{-1} mg^{-1}	Relative activity %	Number of isolations
rTAO	309 ± 45	100	4
T124A	244 ± 75	79	3
rSgAOX	230±56	100	6
T179A	66 ± 36	28	3

Table 4-2:- Specific acitivities for recombination TAO and T124A mutation. Activities of rSgAOX and T179A (equivalent mutation within the plant species) included for reference. Data collected under same conditions as those listed in Table 4-1

The examination of the equivalent mutation in plant AOX and TAO reveals dissimilar results with respect to the percentage of remaining activity. T124A and

T179A flank the iron binding glutamate within their respective proteins, with the crystal structure of TAO revealing that the amino acid side chain is directed away from the active site, playing a dual role of helical maintenance within the active site and participating in the dimer interface. The differences between effects on activity are likely due to increased dependence of SgAOX on dimer formation, as trypanosomal AOX has been shown to be a monomer in its native form [180].

4.4.1 Membrane bound respiratory measurements using quinol

Mutation	Specific activity µmol Q_1H_2 min^{-1} mg^{-1}	Relative activity %	Number of isolations
rSgAOX	1.5 ± 0.6	100	4
T179A	0.51 ± 0.3	34	3
D163A	0.29 ± 0.01	19	2
R159A	0.81 ± 0.1	54	4
Y299F	0.63 ± 0.1	42	3
N216A	0.56 ± 0.04	37	3
L177A	0.21± 0.00	14	2
L267A	0.36 ± 0.1	24	2

Table 4-3: Specific activity of membrane bound rSgAOX and mutants measured spectrophotometrically. Assays were performed in 1ml Tris-HCl pH 7.4, 10mM pyruvate,with 150µM Q1H2 as substrate, with the change in absorbance at 278nm measured to determine rate of quinol conversion.

Respiratory activity of membrane bound AOX was also determined using quinol as a substrate. The conversion of quinol to quinone was measured spectrophotometrically at 278nm, with initial rate data collected. In a majority of cases, the data presented in Table 4-3 demonstrates a marked reduction in deviation when compared to the data collected from the oxygen electrode.

When compared to the data in Table 4-1, two major factors are apparent; the percentage activity of the mutants does not correlate completely to measurements made on the oxygen electrode, and the quinol activity is larger than the oxygen uptake measurements. While stochiometrically the Q_1H_2 depletion rate should be

double the rate of oxygen uptake, rates for quinol oxidation are ~10-fold of oxygen uptake. With both of these factors taken into account, it would suggest that the use of quinol as a substrate gives a true V_{max} for the protein in the membrane bound form, with the data collected using the oxygen electrode representing typical physiological conditions.

4.5 Purification

Purification of the plant alternative oxidase was afforded by a modified protocol of that used for the TAO purification procedure [163], as per the method described in Chapter 2. The pET-15b vector system encodes for an N-terminal His-tag, allowing for purification via cobalt affinity chromatography. Detergent screens revealed that 1% n-dodecyl-β-d-maltopyranoside (DDM) gave improved solubilisation of plant AOX, and as such subsequent wash and elution buffers were adjusted to a 0.5% (w/v) octaethylene glycol monododecyl ether (C12E8) / 0.5% (w/v) DDM mix.

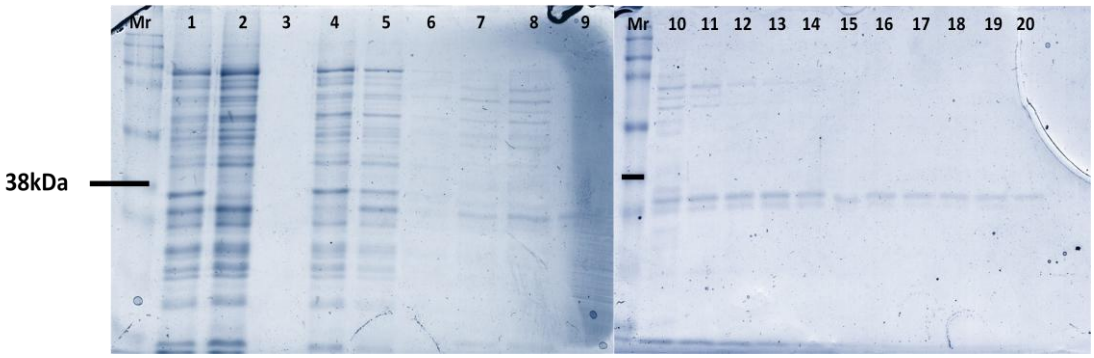

Figure 4-4: SDS-page gels showing the use of stepwise purification of rSgAOX from membrane fractions. Tracks from left to right:- Mr - markers, 1 - membrane, 2 - solubilised membrane, 3 - insoluble fraction, 4 - flow through, 5 - wash, 6-20 – eluate fractions. The visible band in from fraction 8 onwards was confirmed as alternative oxidase via western blot anaylsis.

Figure 4.3 demonstrates that we were able to obtain extremely pure samples using a graduated (100-250mM in 50mM increments) increase in imidazole concentration within the elution buffer. The visible bands in lanes 10-20 at ~32kDa correspond to

AOX, with confirmation of protein identity via western blot analysis. While pure, the samples were dilute and not suitable for assay purposes so a simpler technique was used whereby a second wash was used to ensure removal of non-specifically bound matter and a single elution of 250mM imidazole presented a useable protein concentration.

Fraction	**Total activity** **µmol Q_1H_2 min^{-1}**	**Total protein** **mg**	**Specific activity** **Q_1H_2 min^{-1} mg^{-1}**
Membrane	7.3	9.2	0.8
Pellet	3.7	3.1	1.5
Soluble	7.8	5.2	1.2
Flow through	3.5	3.1	1.13
Wash	2.6	1.4	1.9
Elution	0.65	0.36	1.8

Table 4-4:- typical purification table for mutant rSgAOX purification (data presented from Y299F). Fractions refer to stages of protein purification. Activities measured spectroscopically using 150 µM Q_1H_2 in 1ml Tris-HCl pH 7.4 with 10mM pyruvate.

Summation of the total activity flow through, wash and elution fractions from the data in Table 4-4 gives a value of 6.75 µmol Q_1H_2 min^{-1}, showing that 86% of the total activity of the soluble protein is retained through the purification process. The same process with the total protein confers a value of 94% indicating that modest protein was retained by the column and that statistical variability in the protein estimation performed could account for the loss of protein.

The flow through and wash fractions contain protein that was either unable to bind to the resin, or weakly bound protein that was eluted with 50mM imidazole. While western blot analysis of the flow through fraction was shown to contain AOX, further attempts to purify this fraction proved unsuccessful, suggesting that either the His-tag had been cleaved from the protein prior to binding to the column, or the tag itself was inaccessible. Given the wrap-around nature of the N-terminal region, the later seems more likely.

High levels of activity within the wash are indicative of improper His-tag binding to the column. Attempts were made to increase the binding to the column via increasing binding time, increasing the resin to solubilised protein ratio, and altering the temperature, but proved unsuccessful. While it did appear that decreasing the volume of wash buffer to 1 times the bed volume increased protein content within the elution, analysis of the fraction revealed that this reduced the purity of the protein and as such was not a viable method.

Sample	Specific activity membrane µmol Q_1H_2 min^{-1} mg^{-1}	Specific activity elution fraction µmol Q_1H_2 min^{-1} mg^{-1}	Purification factor	Percentage of wild type	Isolations
rSgAOX	1.5 ± 0.6	16 ± 3.1	10.6	100	4
T179A	0.51 ± 0.3	1.16 ± 0.2	2.3	7.3	3
D163A	0.29 ± 0.01	0.29 ± 0.03	1	2.9	2
R159A	0.81 ± 0.1	0.2 ± 0.1	0.25	1.3	3
Y299F	0.63 ± 0.1	1.47 ± 0.3	2.3	9.2	3
N216A	0.56 ±0.04	1.26 ± 0.3	2.3	7.9	3
L177A	0.21±0.00	0.24 ± 0.01	1.1	1.5	2
L267A	0.36 ± 0.1	0.23 ± 0.00	0.63	2.3	2

Table 4-5:- Specific activities of the elution fractions from cobalt affinity purification of rSgAOX and associated mutants. Activities measured spectroscopically using 150 µM Q_1H_2 in 1ml Tris-HCl pH 7.4 with 10mM pyruvate. Specific activity of the membrane fraction is from Table 4-3, and purification factor refers to the ratio of elution specific activity to membrane specific activity.

The specific activities determined for the pure AOX fractions are shown in Table 4-5. The purification factor gives an indication as to the relative increase in specific activity from the membrane bound form, and the values obtained indicate that all mutants demonstrate a significant loss in purification relative to the wild type. While it would be tempting to speculate that the mutations have affected the stability of the protein to an extent whereby removing them from the membrane and passing them

down a column leads to widespread destabilisation and potential unfolding of the protein, the retention of activity within the flow through, wash and elution fractions relative to the soluble would suggest that this is not the case. However, it is likely that R159A and L267A suffered from destabilisation, as upon solubilisation they were the only mutants tested that demonstrated a reduction in specific activity.

One of the more apparent factors is that purification of the mutants induces a much larger reduction in specific activity when compared to the wild type. All mutants have specific activities less than 10% of wild type levels, significantly lower values then those determined in the membrane bound form.

There appears to be an inverse correlation between the purification factor and specific activities of all samples, which could be indicative of a requirement for increased protein expression for survival of the cell due to low rate of turnover. A low purification factor would suggest that a larger proportion of protein within the membrane bound sample is AOX, although it is a combination of factors such as mutant stability and how robust it is to solubilisation and purification conditions.

4.6 Effectors of AOX

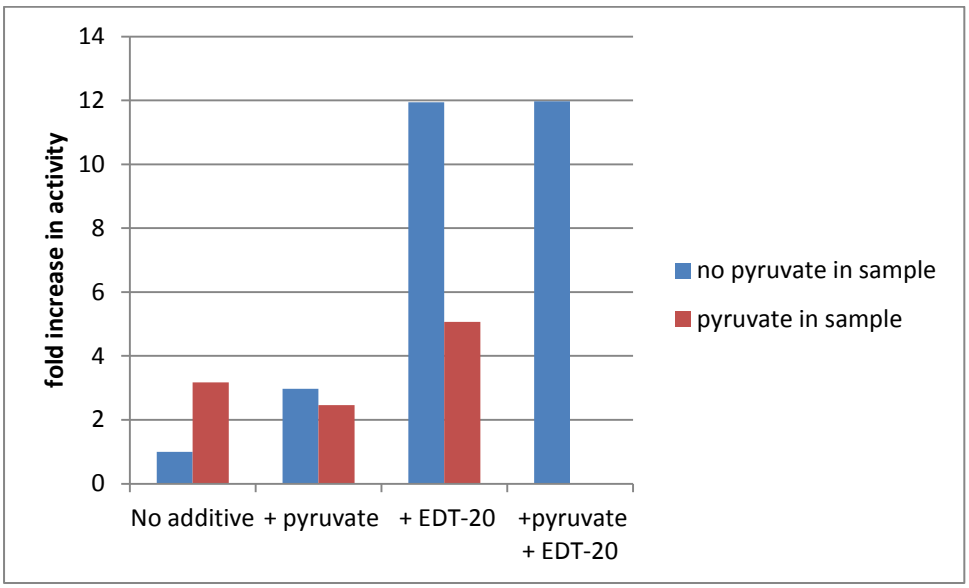

Figure 4-5: Data to show the increase in specific activities of purified rSgAOX upon the addition of effectors. Blue bars indicate purification using buffers that did not contain pyruvate, and red contained pyruvate in the buffer. Effector concentrations were 10mM pyruvate, and 0.25% (v/v) EDT-20. Activity measurements performed using the same conditions described in Table 4-3.

While pyruvate is well documented in increasing the catalytic activity of AOX [69, 154, 158], a response that can be mimicked in micochondria isolated from *A. italicum* using EDT-20 [70], and purified TAO [163]. As such, both compounds were tested against the purified sample to allow for assessment of their impact on SgAOX. As can be seen in Figure 4-5, the further addition of pyruvate to sample containing pyruvate within the purification buffers did not further increase the respiratory activity, while addition of pyruvate to a sample lacking pyruvate increased activity by a factor of 3. The more interesting effects were seen upon addition of EDT-20, whereby the pyruvate-free sample demonstrated a marked increase in activity over its counterpart. Further addition of pyruvate to this sample did not increase activity, suggesting that stimulation of activity is competitive between the two effectors.

4.7 Oxygen Kinetics

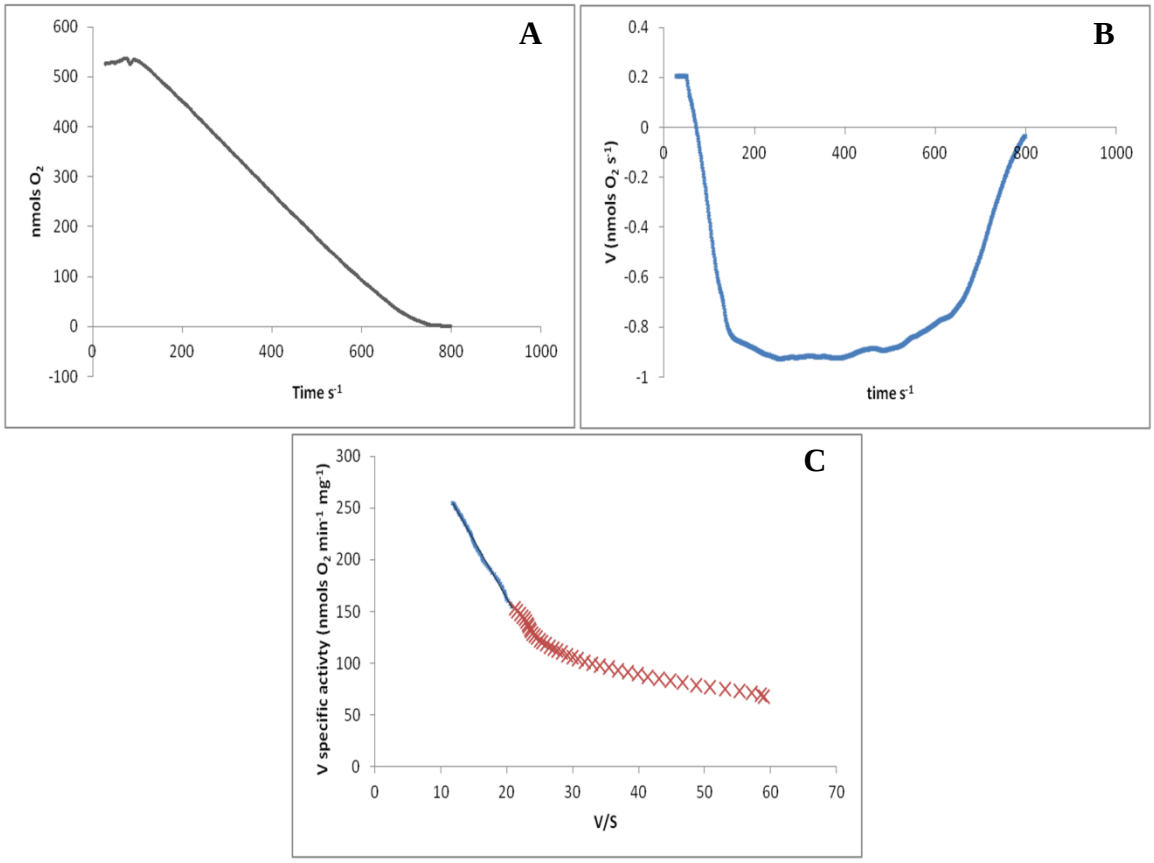

Figure 4-6:- Method for determination of oxygen Km values. Graph A shows the trace obtained from the oxygen electrode. Graph B is the derivative graph, displaying Michalis-Menten kinetic dependance upon the oxygen concentration. Graph C is the Eadie-Hoffstee for the data within the oxygen dependant region. Blue data indicates the data used for oxygen Km values, and red data indicates the region of data below the 10 nmol O_2 cutoff set, whereby the sensitivity of the electrode became a contributing factor.

Oxygen kinetics were measured via the method described by Crichton [175]. 2ml of TRIS was used to ensure enough dissolved oxygen was within the cell for the reaction to reach a steady state, which can be seen in graph B of Figure 4-6. The graph clearly demonstrates a kinetic dependency upon the substrate prior to 200seconds, followed by a steady rate and reduction due to limiting oxygen concentrations within the system.

Sample	Oxygen K_M / µM	Isolations
rSgAOX	13.1 ± 0.3	3
L177A	8.9 ± 0.6	2
T179A	6.1 ± 0.4	3
L267A	16.5 ± 1.2	2
Y299F	13.1 ± 0.1	3
D163A	5.9 ± 0.4	2
R159A	10.8 ± 0.2	3
N216A	6.0 ± 0.4	2
rTAO	12.6 ± 0.4	3
T124A	5.6 ± 0.7	3

Table 4-6:- Oxygen Km's for membrane bound rSgAOX and mutant samples. Data obtained using the method described in Figure 4-6. Samples were run in 2ml Tris-HCl pH 7.4 with 50mM pyruvate and 1.25mM NADH on an oxygen electrode. rTAO and T124A mutation are from the trypanosomal species and added for comparison.

One of the interesting features of graph C (Figure 4-6) is the area highlighted in red. While it is below the 10nmols O_2 cutoff for reliable results on the electrode, it appears to be linear in character and could potentially be a second K_M. It is worth noting that while it can clearly be seen as linear in the graphs used here, this section does not always present a linear correlation. Given that decrease in turnover would increase the quinol:quinone ratio, this could potentially indicate an increased affinity for oxygen at a high quinone pool redox poise. The red region presents a K_M of 1.4 µM, much closer to the 1.3 µM determined spectrophotometrically [65], which could potentially explain the discrepancies between the reported results. It is also possible that this region is due to residual cytochrome b_d or b_o, given their lower K_M for oxygen. Km's of this magnitude have been detected in soybean mitochondria, where the altered value was attributed to AOX isozymes present within the system [181].

Apparent oxygen Km data for plant wild type demonstrates similar values to those collected from mungbean (12.3 µM [63]) and soybean (13.2 µM [64]) collected polarographically, and is comparable to data collected previously from this group with the recombinant system in *S. pombe* (20 µM [175]). While it is possible that a change in medium and cell type could alter the ability for oxygen to diffuse into the

active site, it is unlikely that this can contribute to the differences in results due to the similarities of the T179A values obtained in this study relative to those determined previously.

The data inTable 4-6 demonstrates that those mutations which are close to the di-iron core all reduce the Km for oxygen. What is useful is that the data discriminates between iron atoms; L177A and T179A both demonstrate Km's lower than the wild type value and flank the glutamate binding to Fe2, and N216A neighbours the bridging glutamate, also giving a lower O_2 Km. While the latter would imply that there is no discrimination between the irons, the addition of the lack of change with the L267A Km would suggest this mutation is having a larger effect on Fe2 then Fe1. The similarity between the Y299F value and that of the wild type would also suggest that the change in N216A is likely to be due to interactions with the iron core rather than perturbation of the PCET network. The lack of change to the oxygen Km for Y299F is surprising; given the conclusion drawn in Chapter 3 with its part in stabilising the PCET network, and this networks role in the initial binding stages of oxygen, it was expected to lower the Km for oxygen considerably.

While the oxygen Km for R159A does not appear statistically significant when compared to the wild type, when combined with D163A it would suggest otherwise. What is interesting about this pair is that if the placement of these residues within TAO is indeed the same as in plant AOX, R159 is closer to the core then D163, indicating that it is unlikely due to direct effects upon the iron core. One theory that could potentially fit the data would be the destabilisation of the hydrogen bond formed between D163 and R173 causing movement in the helix. It has previously been shown that C172A also leads a reduction in oxygen Km [175], and a similar value was obtained with T179A. This would explain the lower value detected in R159A as secondary effects upon D163A, removing the second stabilisation point for the aspartic acid. If a mutation of R173 is active, it would be interesting to see whether the same result is obtained.

One of the more important results for this study is that both wild-types and their respective mutations of the threonine demonstrate similar affinities for oxygen, demonstrating that the immediate active site and electronic effects of amino acids that will affect the reactivity towards oxygen around the iron are equivalent.

Sample	Oxygen K_M
rSgAOX	14 ± 1
rTAO	8.9 ± 2
T179A	6.7 ± 2
T124A	11 ± 4

Table 4-7:- Oxygen Km data for samples taken without the addition of pyruvate to the sample. All measurements and standard deviations taken as mean averages from 3 replicants.

Membrane samples were prepared without pyruvate to allow for assessing the effects upon oxygen kinetics. As discussed in Chapter 1, pyruvate has been demonstrated to have regulatory effects on the plant AOX , whereas TAO shows no activity dependence upon pyruvate [182].

The data in Table 4-7 demonstrates that while lack of pyruvate within the plant sample does not alter the Km to oxygen by a significant degree, it increases the standard deviation around the mean. The increase in variance would suggest that activation by pyruvate aids continued turnover of the active site, allowing for a more regular binding affinity for oxygen. Results would suggest that pyruvate is inhibitory to the oxygen binding within rTAO, given the significant increase in Km upon its addition to the sample.

4.8 Summary

Sample	O2 electrode activity %	Quinol activity %	Purified activity %
T179A	28	34	7.3
D163A	31	19	2.9
R159A	24	54	1.3
Y299F	32	42	9.2
N216A	23	37	7.9
L177A	51	14	1.5
L267A	41	24	2.3

Table 4-8:- combined percentage activities of rSgAOX mutants relative to the wild types under different measurement conditions. Original data and measurement conditions can be found in the descriptions of Table 4-1,Table 4-3, and Table 4-5 respectively.

Table 4-8 shows the lack of correlation between the specific activity measurements under different conditions. Measurements made using quinol as a substrate are more indicative of the true V_{max} for each sample given that both quinol and oxygen are in excess, with measurements made on the oxygen electrode closer to conditions found within a biological system. The mutants which show a decrease in relative activity with quinol as the substrate when compared to oxygen uptake measurements (D163A, L177A and L267A) are all located within the hydrophobic cavity, and as such are liable to interfere with the substrate's ability to bind within the active site. There is potential that the L177A and L267A mutants alleviate the problems associated with the change in quinone type found within the *E. coli* membrane; if there were indeed times of growth under anoxic conditions and therefore generation of menaquinol as a substrate, the widening of the hydrophobic cavity could allow for easier access to the di-iron core for the bulkier substrate, consequently masking the reducing effects of mutation.

Interestingly, the most significant increase was R159A, which could indicate an opening of the orthogonal cavity discussed in Chapter 3. While measurements made using NADH as the substrate would be constrained to the quinol pool within the

membrane, and therefore reduced access to the second cavity, addition of quinol into solution would not be under the same limitations and could therefore dock via the second cavity. If this was the case, it would be expected that D163A would also fulfil the same trend, but instead it has shown a decrease in rate. This could potentially be due to steric bulk; an arginine to alanine mutation removes a bulky side-chain, whereas the aspartic acid mutation simply removes the carboxylic acid. Removal of the larger side-chain would allow access to the active site that could effectively mask a reduction in rate, whereas removal of the carboxylic acid destabilised R159 and the surrounding region leading to the loss of turnover.

The loss of mutant activity in the purified protein relative to the specific activities measured in membrane bound is not unprecedented; data included in the supplementary data of the TAO crystallisation paper [11] indicated all mutants retained 5% or less when compared to the wild type TAO. Further studies into the stability of the purified protein could provide answers as to the extreme reduction in specific activities measured. Circular dichroism measurements would give indications as to whether the mutations within the structure impede the proteins ability to fold or form helices.

While it has been postulated as to why each mutant would affect AOX activity, it is difficult to generate direct evidence as to whether these claims are true. The oxygen Km measurements have indicated that a number of mutations reduce the Km for oxygen, while simultaneously demonstrating a decrease in overall activity. Under the assumption that the lowered Km would correlate to an increase in binding affinity, it would suggest that these mutations either slow the rate of intermediate conversion with respect to the oxygen reduction cycle, or reduce the ability of the iron core to react with quinol. Examination of the reactivity of T179A, D163A and N216A using stop flow techniques could potentially allow for the detection of intermediates in these mutants that would otherwise not be visible in wild type due to low half lifes. Indeed, preliminary EPR measurements of the T179A mutant have revealed the build-up of a semiquinone species within the sample, but the reason for this build-up is unclear at this time.

5 Inhibition of the alternative oxidase and bc_1 complex by natural products

5.1 Introduction

The alternative pathway is well established as being resistant to inhibitors of the regular ETC, including cyanide, NO, azide and cytochrome bc_1 inhibitors such as antimycin A. Given the dependant nature of the trypanosomes on TAO, and the lack of AOX within mammalian cells, it has been identified as a potential chemotherapeutic target for human African trypanosomiasis (HAT) [83]. SHAM [97, 183], octyl gallate [94] and ascofuranone [110] have all demonstrated inhibitory properties towards the alternative oxidase, with the latter being the most potent.

Ascofuranone proves problematic from a synthetic standpoint, in that synthesis requires 11 steps, with a number of synthetic steps producing intermediates in lower than 20% yield. To improve on this, colletochlorin B was selected as a reasonable replacement, containing the pharmacophore whilst removing the problematic furanone ring and reducing the necessary synthetic steps to 4. A structure function analysis has also been performed on the necessity of the aldehyde for inhibition, alongside effects of the compound tail on inhibition of both AOX and the bc_1 complex.

Use of inhibitors towards AOX would not solely be useful for HAT treatment. The alternative pathway has been identified as a potential biological mechanism for fungicidal resistance development [123] with evidence that inhibition of the cytochrome bc_1 complex leads to an induction of AOX expression [50]. While respiration via the alternative pathway would lead to a decrease in ATP levels, it allows the cell to develop resistance to fungicides via random point mutations.

With these two main functions for inhibitors of the AOX in mind, the development of both an inhibitor that would specifically inhibit TAO for use in treatment of HAT, and a dual mode inhibitor that would inhibit both AOX and the cytochrome bc_1 complex for use as a fungicide.

5.2 Compound Synthesis

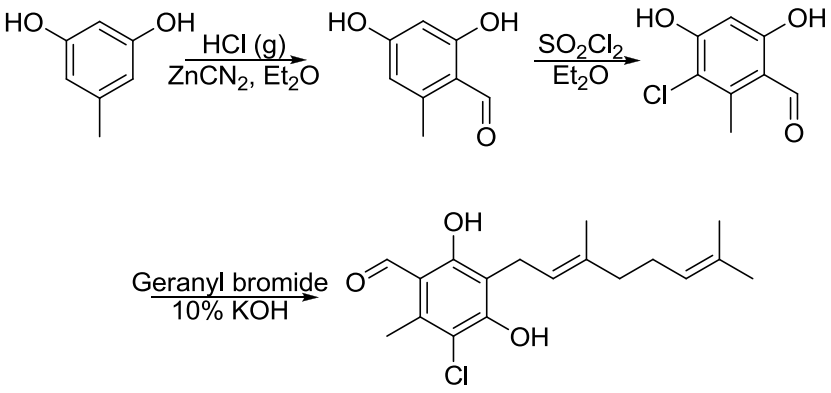

Scheme 5-1:- Mori's synthesis of colletochlorin B [118]

Synthesis of the ascofuranone derivative colletochlorin B was performed according to Mori's synthesis [118], with a few minor adjustments. In short, orcinol was formylated under Gatterman conditions [184] to obtain the aldehyde in 84% yield. Chlorination using sulfuryl chloride resulted in the desired isomer at 80% yield, which was then alkylated with geranyl bromide in 10% potassium hydroxide overnight. The compound was purified via flash chromatography using a gradient (petrol ether:ether 10:1 → 4:1), and recrystallised from chloroform to obtain colletochlorin B in 20% yield.

The use of freshly prepared geranyl bromide increased the yield from 5%, with quantitative preparation from geraniol and phosphorous tribromide. The same experimental procedure was used to synthesise colletochlorin D, substituting 3-3-dimethylallyl bromide at the final alkylation step to afford the compound in 30% yield.

Comparing TLC analysis prior to chromatography to post-column showed a marked difference between product distribution. It is likely that the acidic nature of the silica proved detrimental to compound stability, with evidence in the literature that exposure to highly acidic conditions results in chromane ring formation [115]. Attempts to isolate the degradation products were unsuccessful, with proton NMR

analysis suggesting a mixture of isomers. Neutralisation of the silica using 0.5% triethylamine prior to chromatography did not appear to improve the yield.

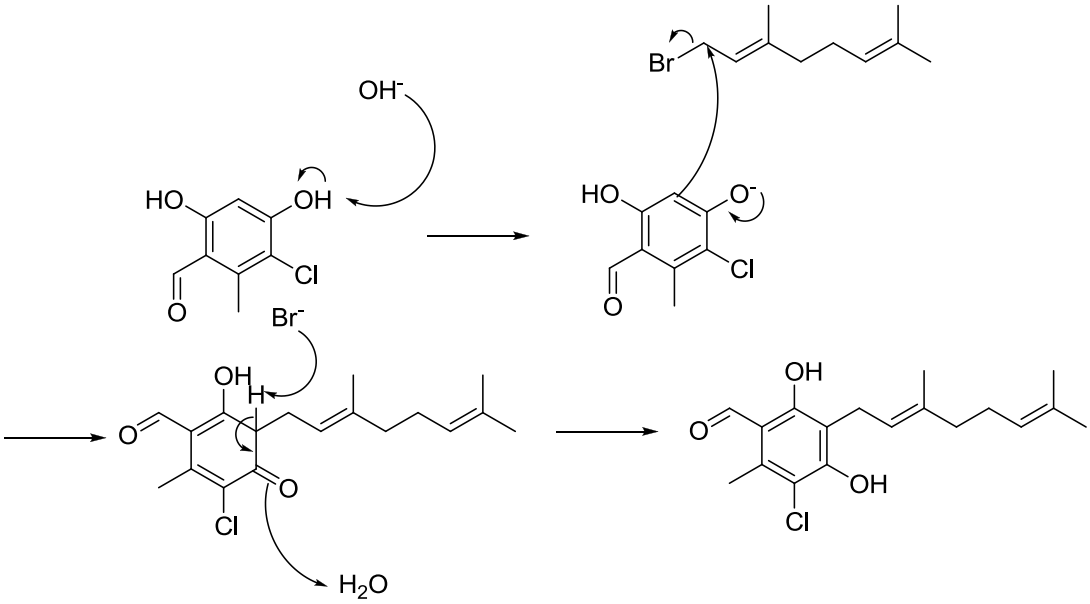

Scheme 5-2:- Alkylation step of colletochlorin B synthesis, showing the formation of the anion. A lack of driving force for alkylation to the central carbon as depicted above leads to the formation of ether via direct alkylation onto the oxygen.

A number of side products were formed during the alkylation step, which can largely be attributed to ether formation onto the phenol. Given the poor yield of the final alkylation steps a number of attempted improvements were made. Protecting group strategies using acetyl and methyl protecting groups failed to yield the desired alkylated product using both potassium hydroxide and sodium hydride. The lack of reactivity of the protected compounds suggest that the reaction proceeds via generation of a phenolic based anion prior to the push of electron density through the unsubstituted carbon, with regeneration of the aromaticity driving the reformation of the alcohol after alkylation, as depicted in Scheme 5-2.

Preparation of the acetylated compound was afforded by stirring colletochlorin B in a 1:1 mixture of acetic anhydride and pyridine to obtain the product in quantitative yields after stirring overnight. Reduction of the acetylated compound with sodium borohydride in ethanol gave a mixture of 2 compounds. Even with two distinct Rf

values (~0.6 and ~0.4) attempts to purify these compounds via flash chromatography proved unsuccessful. It is likely that these 2 compounds can be attributed to a migration of the acetyl group onto the newly formed alcohol, which would explain the lack of ability to separate the two compounds due to interconversion between species. Attempts to deprotect the compounds proved unsuccessful under mild conditions, with harsher conditions causing compound degradation.

The reduced form of colletochlorin B could be made via direct reduction using sodium borohydride in ethanol at room temperature for 1 hour. The reaction mixture was coevapourated 3 times with methanol to remove the borohydride, and purified using flash chromatography. Attempts to improve the yield of the reaction proved unfruitful, as the compound proved unstable and decomposed with both increases in heat and reaction time. Resolvating the compound also proved problematic, with low solubility in organic solvents. Attempts to dissolve the compound into organic solvents with nucleophilic character (methanol and ethanol) at 40°C produced the decomposition product, which on further examination appeared to be the addition of a methoxy group to the compound. The generation of a quinone methide *in situ* appears to be the most likely reason for compound instability, with methanol acting as a nucleophile towards the newly generated electrophilic site.

5.3 Results and discussion

Fitting of curves

Sigmoidal curves were fitted to the data according to the formula a+((b-a)/1+((x/c)^d))), where ‘a’ was the value for the bottom of the curve, ‘b’ the top (in the case of 100% inhibition for compounds 0 and 100 respectively) ‘c’ the IC_{50} value (midpoint of the curve) and d was the slope. Curves were optimised according to a least mean square fit method.

5.4 Inhibition of the alternative oxidase

5.4.1 *Arum maculatum* mitochondria – effects of inhibitors

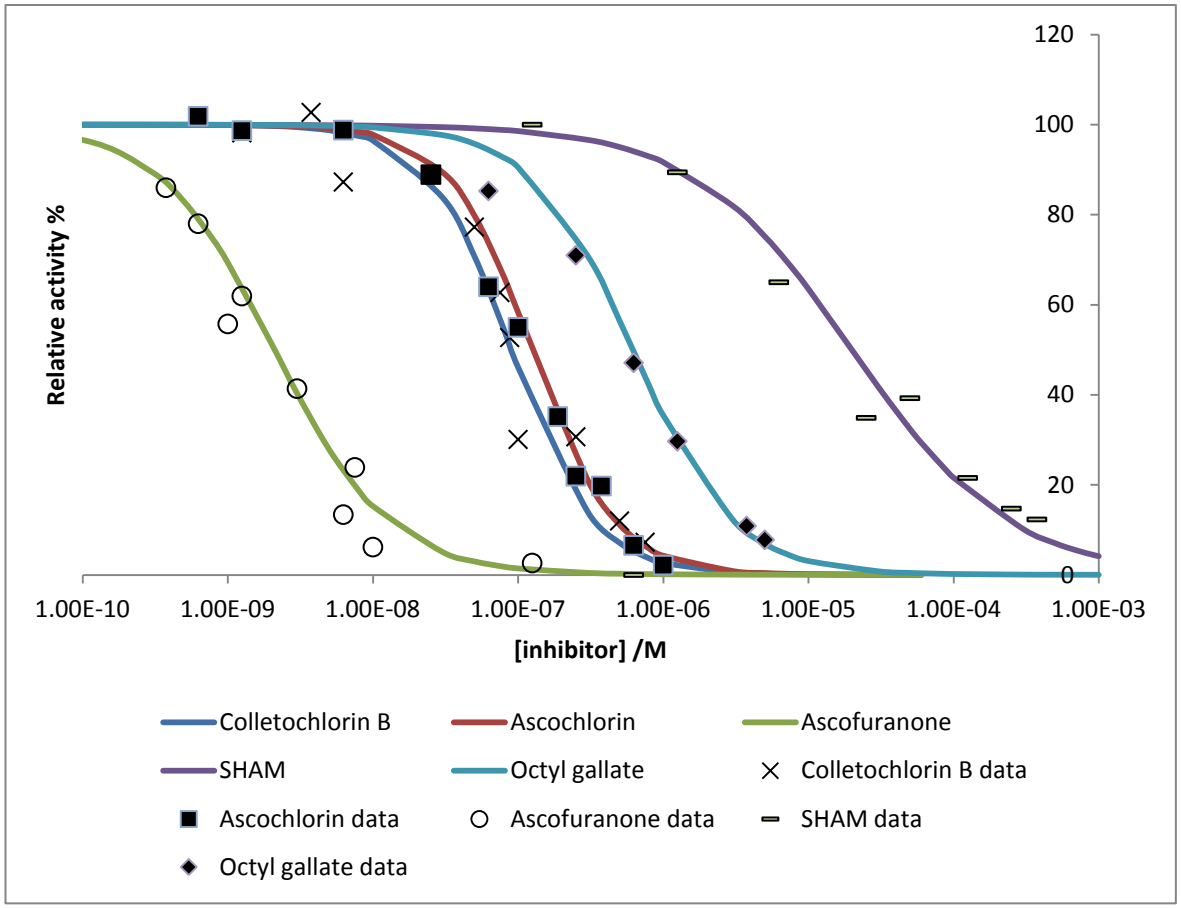

Figure 5-1 Dose response curves collected for AOX dependant respiration from *A. maculatum* mitochondria. Data was collected using an oxygen electrode, containing 400 µl plant medium A, 0.033mg mitochondrial protein, 1.25mM NADH and 4 µM Antimycin A to inhibit cytochrome bc_1 activity. IC_{50}'s for ascofuranone, ascochlorin and colletochlorin B were 9nM, 90nM and 125nM respectively. SHAM and octyl gallate added for clarity

The spadices of *Arum maculatum* were picked locally and mitochondria isolated as described in Chapter 2. NADH dependant respiration was measured using an oxygen electrode in conjunction with Antimycin A to determine the alternative pathway respiratory rate. Unlike the *E.coli* membrane bound samples described in Chapter 3, addition of excess duroquinol to the assay did not increase the respiratory activity, indicating that quinol levels were at saturation.

Data collected was normalised to an uninhibited rate of 60nmols O_2 consumed/minute. Using mitochondrial protein estimation between preparations proved problematic from a normalisation standpoint given the increasing alternative oxidase expression levels later in the season does not necessarily correlate to an increase in protein levels. Degradation between assay runs indicating a loss of activity are also not taken into account if protein levels were the sole basis for comparison between preparations.

Compound	Normalised IC_{50}
Colletochlorin B	67±17 nM
Ascofuranone	7 ± 5 nM
Ascochlorin	70 ± 18 nM
SHAM	17 µM
Octyl gallate	670 nM

Table 5-1 IC50 data collected from alternative oxidase dependant respiration in *Arum maculatum* mitochondria. Standard deviation included for inhibitors tested against more than one mitochondrial isolation. Values are averages ± standard deviation for 4 (CB) or 3 (Ascofuranone and Ascochlorin) replicants. SHAM and Octyl gallate are single experiments for comparison.

SHAM and octyl gallate are known inhibitors of the alternative oxidase [85, 94, 185, 186], showing competitive [84] and non-competitive inhibition respectively with respect to quinol. Both compounds have been demonstrated to inhibit in a non specific manner, with SHAM inhibiting tyrosinase and peroxidase [87], and octyl gallate inhibiting Δ6 desaturase [187].

Table 5-1 demonstrates that the experimental IC_{50} values determined are comparable to literature values for SHAM (40 µM against *Arabidopsis thaliana* mitochondria [84]) and octyl gallate (350nM[84]). While colletochlorin B, ascochlorin and ascofuranone contain the same pharmacophore, the IC_{50} for ascofuranone is significantly lower, suggesting that the furanone moiety aids in binding the compound to the active site. While ascochlorin also contains functionality at the end of the chain, it does not appear to affect binding in either a beneficial or detrimental manner. Azoxystrobin was also tested, but showed no

inhibition at concentrations of 500 µM, confirming that when used as a fungicide, the fungal alternative pathway will remain unhindered.

In order to ensure that inhibition was specific for the alternative oxidase, the activity of NADH dehydrogenase was measured as described in Materials and Methods. No change in DCPIP reduction rates were detected upto inhibitor concentrations of 5 µM, indicating that inhibition of the electron transport chain must be occurring at the alternative oxidase.

5.4.1.1 *Arum maculatum* mitochondria – derivatives of colletochlorin B

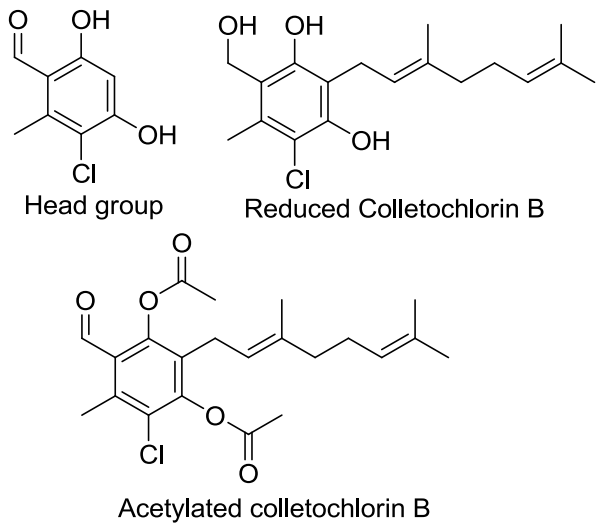

Figure 5-2:- colletochlorin B derivatives tested against *Arum maculatum* mitochondria.

Compound	IC_{50}
Colletochlorin B	67 nM
Colletochlorin D	110 nM
Reduced Colletochlorin B	4 µM
Acetylated Colletochlorin B	92 µM
Head group	28 µM

Table 5-2:- IC_{50} values for colletochlorin B derivatives against *Arum maculatum* mitochondria. Data collected using the method described in Figure 5-1, data depicted is an average of 2 preparations.

The synthesised derivatives shown in Figure 5-2 were also tested for inhibitory efficacy against *Arum maculatum* mitochondria, with results given in Table 5-2. Loss of an isoprene unit from the tail of colletochlorin B to form colletochlorin D had a relatively small effect on the inhibitory efficacy of the compound, requiring double the concentration to reach 50% inhibition. However complete removal of the tail unit increased the IC_{50} into the μM range. Given the mimetic nature of the tail to that of quinol, it is likely that it is necessary for binding site recognition and orientation within the active site. This has been demonstrated with quinol analogues in their reaction with cytochrome b_o [173], whereby reduction of the double bond reduced binding affinity for the complex. It may also be indicative that removal of the isoprenoid tail reduces the lipophilicity of the compound, preventing it from entering the cellular membrane as efficiently and therefore reaching the site of inhibition.

Acetylation of the two alcohol groups has the largest impact on inhibition. This is unsurprising given the nature of inhibitor binding discussed in Chapter 3, whereby the phenol groups anchor the inhibitor into the active site. Reduction of the aldehyde also demonstrated a large increase in IC_{50} concentration, which would suggest that it is more important for binding then the crystal structure would suggest. It is entirely possible that the decrease in compound stability is the cause of reduced inhibitory properties, with degredation of the compound prior to reaching the active site.

5.4.1.2 Trypanosomes

Compound	IC_{50} nM
Ascofuranone	1.6 ± 0.1
Colletochlorin B	2.6 ± 0.1
Benzoxiborininol	64.2 ± 0.2

Table 5-3:- IC_{50} Data collected from anti-proliferation assays against *Trypanasoma brucei brucei*. Data depicted is an average of 3 replications

The efficacy of the compounds against trypanosomes was confirmed by anti-proliferation assays performed by Dr Shane Wilkinson (Queen Mary University of London). Benzoxiborininol is currently a lead compound for the treatment of HAT [188], with an unknown mode of trypanosidal activity. This compound was tested against TAO, but was shown to not inhibit activity. Ascofuranone acts as a standard for trypanosidal activity via TAO inhibition, having already been demonstrated to be an effective treatment for infected mice [111, 112]. The data in Table 5-3 demonstrates both Colletochlorin B and Ascofuranone are effective compounds against *T. b. brucei,* and that loss of the furanone ring does not affect the compounds ability to eradicate trypanosomes.

When compared to the data in Table 5-1 the IC_{50} values for ascofuranone and colletochlorin B are much closer. This implies that either the binding site for TAO and plant AOX differ in the binding of the compounds, or that the location of the alternative oxidase within the trypanosomes is more accessible for colletochlorin B then in plant mitochondria.

5.4.1.3 AOX membrane – determination of Ki

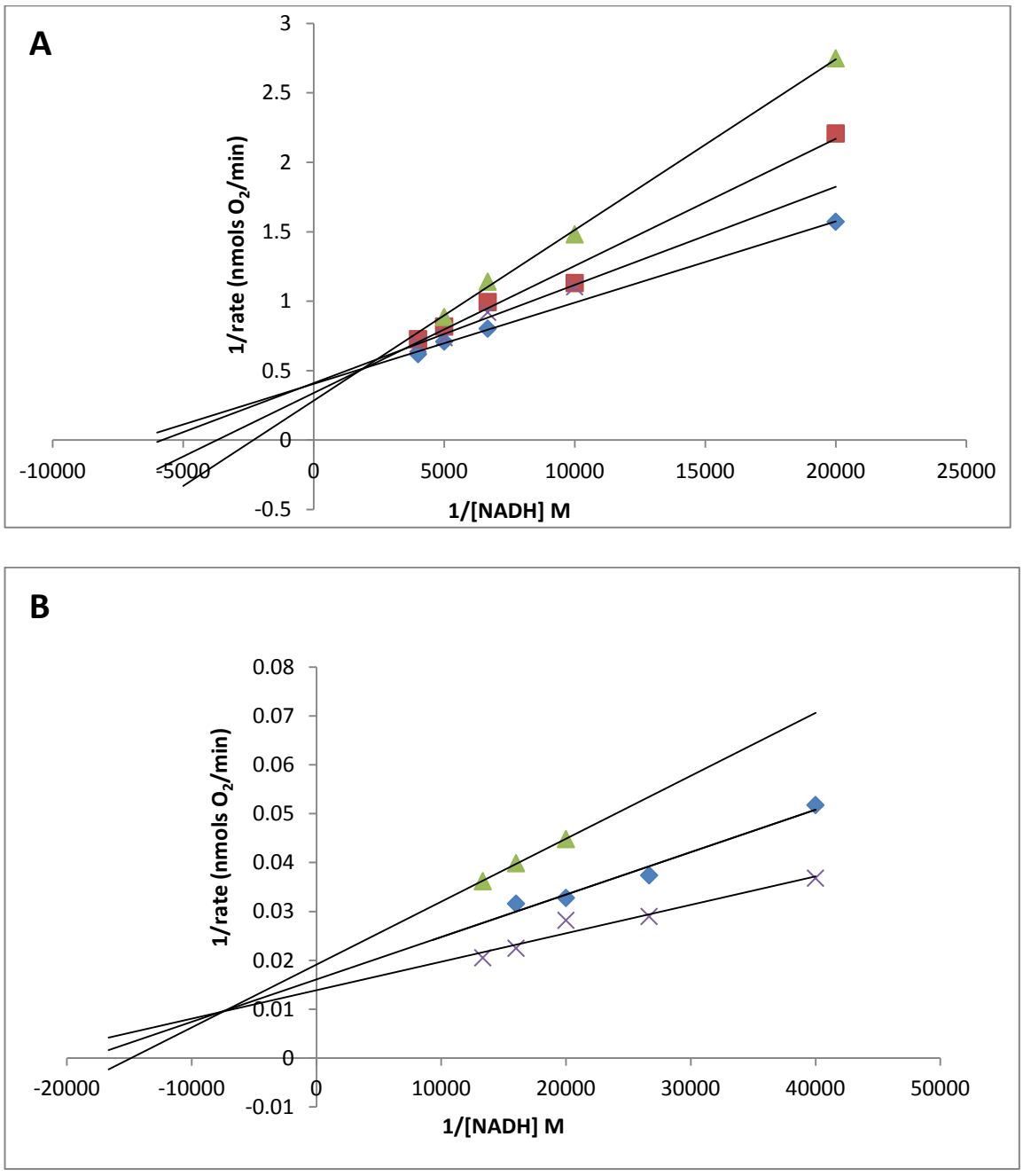

Figure 5-3:- Lineweaver Burke plots collected from membrane bound rSgAOX with varying inhibitor concentrations. Graph A inhibitor concentrations (square) 50nM CB, (triangle) 100nM CB (X) 25nM CB (diamond) no inhibitor. Graph B inhibitor concentrations (diamond) 5nM CB, (triangle) 30nM CB, (X) uninhibited

Figure 5-3 demonstrates that the inhibition profile for colletochlorin B is variable with respect to the alternative electron transport chain. NADH concentrations were decreased to ensure substrate concentration was rate limiting the production of quinol, allowing for a 1:1 conversion of NADH to quinol concentration.

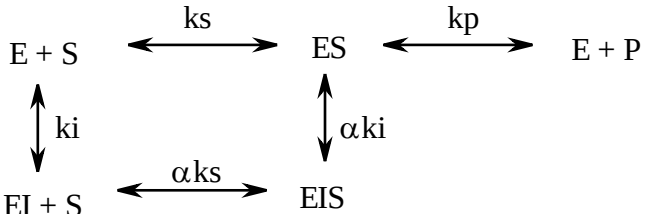

Scheme 5-3:- accepted kinetic variables for a mixed inhibition type. E, I S and P refer to enzyme, inhibitor, substrate and product respectively. Ki and ks define the constants for formation of enzyme inhibitor and enzyme substrate complexes respectively, with αki and αks allowing for cases where the enzyme inhibitor complex is able form complexes with the substrate.

Scheme 5-3 describes the kinetic variables that are part of a mixed type inhibition of an enzyme substrate complex. All details of the scheme and the following equations can be found in Atkins [189]. Each straight line generated in the double reciprocal plot is defined by the following equation:-

$$1/V = ks/V_{max}(1+ [I]/ki)1/[s] + 1/v_{max} (1+ [I]/\alpha ki)$$

Equation 1

Where V is the inhibited rate, V_{max} the uninhibited rate, [I] is the inhibitor concentration and [s] is substrate concentration. Equation 1 can further be split into two components to define the y-intercept and gradient respectively:-

$$\text{y-intercept} = 1/V_{max}\cdot\alpha ki \times 1/[I] + 1/V_{max}$$

$$\text{gradient} = ks/V_{max}\cdot ki \times 1/[I] + ks/V_{max}$$

Equation 2

Equation 2 allows for determination of ki values by plotting the gradients against inhibitor concentration, where the x intercept with be equal to –ki. While the Km values for NADH varies between samples (68µM and 150µM respectively), the Ki values are much closer in value (41nM and 61nM). This would indicate that while there are differences between preparations with respect to electron transport chain, these do not necessarily affect the binding of the inhibitor. Given the apparent problems with obtaining consistent specific activities for the membrane bound wild-type SgAOX, the variability between samples of Km_{app} is likely indicative of altered components within the quinone pool itself, with quinol and menaquinol presenting different Km_{app} towards AOX.

5.5 Cytochrome bc_1 complex

5.5.1 Inhibition of isolated potato mitochondria

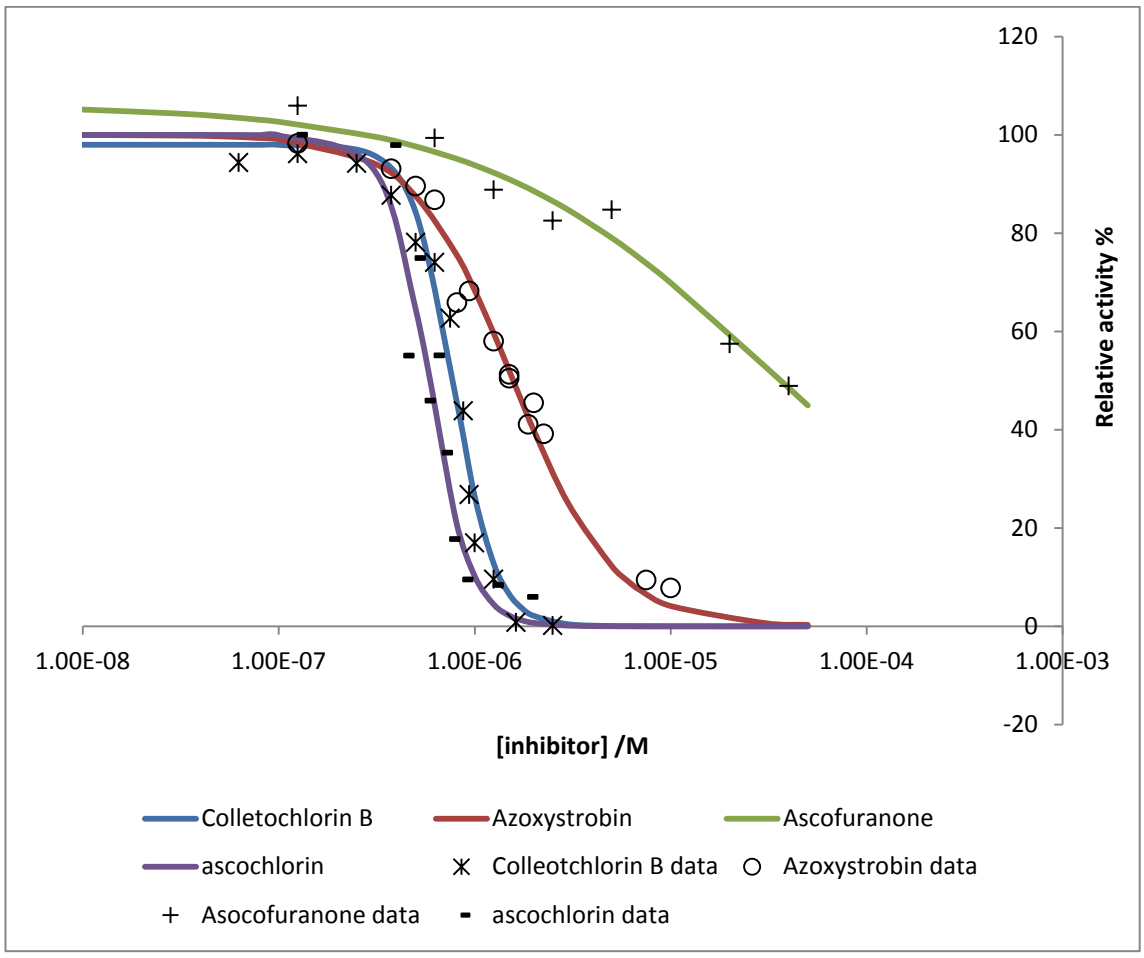

Figure 5-4 :- Dose response curves for inhibitors against potato mitochondria. Assays run in 400 µl plant medium A, containing 0.3mg mitochondrial protein, 1.25 mM NADH as substrate and 1µM CCCP to uncouple the rate from ATP synthase.

Inhibitor	IC_{50} µM	Slope
Ascochlorin	0.58	4
Colletochlorin B	0.78	4
Azoxystrobin	1.57	1.7
Ascofuranone	30	0.6

Table 5-4:- IC_{50} data collected from potato mitochondria. The slope is defined from the sigmoidal curve fitting defined in 5.3.

Mitochondria were harvested from commercial potato tubers, following the protocol outlined in chapter 2.As with the *A. maculatum* mitochondria, NADH dependant respiration was measured using an oxygen electrode. Potato mitochondria were selected due to their low levels of alternative oxidase expression within freshly sliced tuber [51] , allowing for the examination of the inhibitors on the plant cytochrome bc_1 complex.

The data in Table 5-4 demonstrates the efficacy of the compounds towards the plant bc_1 complex, using azoxystrobin as a standard. Azoxystrobin was selected due to the its position as a leading fungicide, with a mode of action that targets Qo site in the bc_1 complex [190]. As can be seen in the table, both ascochlorin and colletochlorin B show increased inhibition of the NADH dependant pathway relative to that of azoxystrobin. The data demonstrates that the furanone ring is detrimental to the inhibition of the bc1 complex, with ascofuranone requiring a higher concentration then was possible under experimental conditions used to achieve 100 % inhibition (as depicted in Figure 5-4).

One of the more interesting features of the curves shown in Figure 5-4 was the increase in Hill co-efficient for both colletochlorin B and ascochlorin relative to inhibition of the alternative oxidase. While each compound had a coefficient of ~1 for alternative oxidase titrations, colletochlorin B and ascochlorin have coefficients of 4, suggesting an increased binding affinity.

5.5.2 RAT liver

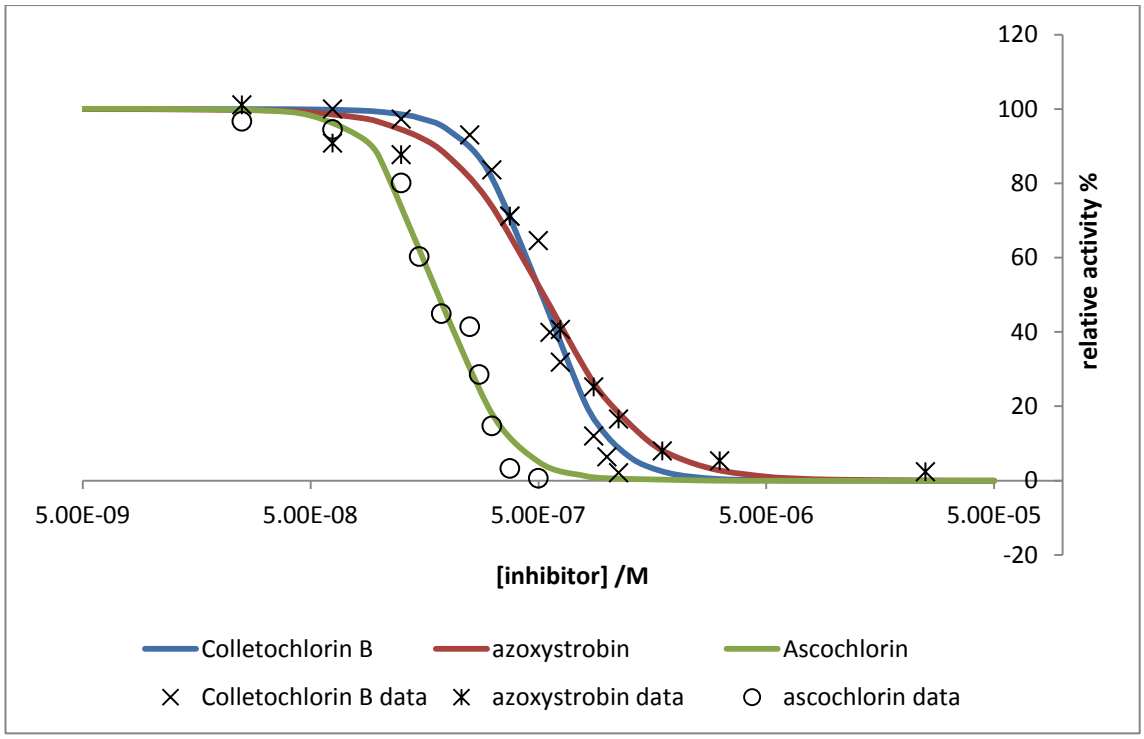

Figure 5-5:- Dose response curves for compounds tested against isolated rat liver mitochondria. Assays were run in a rank-type oxygen electrode, containing 400µl medium A, 0.9mg mitochondrial protein and 1.25mM succinate.

Compound	IC_{50} nM	Slope
Ascochlorin	208	3
Colletochlorin B	547	3
Azoxystrobin	700	2

Table 5-5 :- IC_{50} data collected from rat liver mitochondria. The slope is defined as the hill coefficient from the sigmoidal curve fitting defined in 5.3.

Additional data was collected from mitochondria harvested from rat liver due to their high concentration of the cytochrome *bc*$_1$complex, and lack of AOX allowing for definitive determination of complex III IC_{50} without potential AOX contamination. Succinate dependant respiration was measured due to the lack of external NADH

dehydrogenase in mammalian mitochondria, with an excess used to ensure continued turnover of the ETC.

The relative inhibitory profile for these 3 compounds alters with respect to the mammalian bc_1 complex. The data Table 5-5 demonstrates that the IC_{50} value for colletochlorin B is closer to that of Azoxystrobin, with ascochlorin being a superior inhibitor. The slope coefficient is shown to be superior for ascochlorin and colletochlorin B compared to azoxystrobin, indicating a difference between binding types. However values are closer, which could be due to the nature of the mitochondria within the preparation. More repeats would be necessary to confirm the validity of the data.

5.5.3 Fungal bc_1 complex

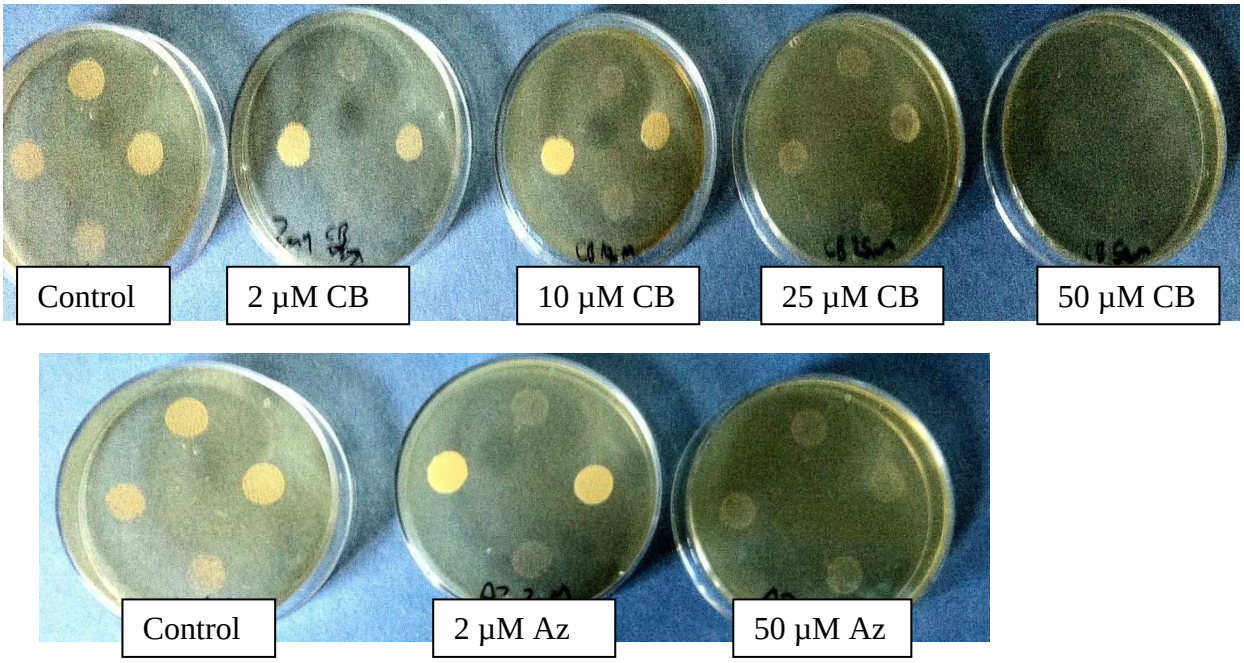

Figure 5-6:- Growth of transformed *S.cervisiae* containing colletochlorin B (CB) and azoxystrobin (AZ) in marked concentrations. Colonies clockwise from the 12 position correspond to Wild type, G143A mutant, K228M mutant and the double mutant containing both G143A and K228M mutations.

Inhibition of the fungal bc_1 complex was assayed using a plate growth monitoring system. *S.cervisiae* cell lines contained wild type cytochrome bc_1 alongside the

mutants G143A [191], K228M and a strain containing both mutants [192] were kindly provided by Dr. Brigitte Meunier (Centre de Génétique Moléculaire). The two mutants are known to decrease the fungicidal efficacy of compounds that target the Q_o (G143A) or Q_i site (K228M), allowing for qualitative assessment as to whether these mutations will affect the inhibitory properties of Colletochlorin B. Azoxystrobin is a known specific Q_o site inhibitor, so acts as a control within this experiment and demonstrates that the mutations within the Qi site do not have a translational effect through to the Q_o site.

Figure 5-6 show that both Colletochlorin B and azoxystrobin prevented growth of the wild type and K228M mutant cell lines at concentrations of 2µM, indicating that this mutation has no effect upon the inhibitory properties of either compounds. However, it can be seen the G143A mutations increased the concentration of inhibitor required to prevent cell growth, with full growth visible on the 10 µM plate, and partial growth on the 25 µM. The inhibition at 50 µM cannot be directly attributed to inhibition at the Q_o site, and could be indicative that inhibitor concentration has increased to a level where it is able to inhibit the Q_i site, although it can be inferred from these results that the primary mode of inhibition is via binding at the Q_o site and the G143A mutation reduces the binding efficacy of colletochlorin B.

5.6 Computational determination of inhibitor efficacy

Compound	Z-Score
Quinol (QH_2)	-8.2
Ascofuranone	-9.7
Azoxystrobin	-9.3
Colletochlorin B	-8.9
Colletochlorin D	-7.9
Ascochlorin	-7.6
SHAM	-7.0
Propyl gallate	-7.3
Octyl gallate	-7.5
Mesaquinone	-8.5
Acetylated	-8.1
Head group	-6.4
Reduced	-8.9

Table 5-6:- Docking results of alternative oxidase inhibitors into the hydrophobic cavity. Compounds were docked using VINA-autodock into the TAO crystal structure (PDB :3VVA). Z-score gives a fit value, whereby a more negative score indicates an increase in binding profile.

Initial docking of compounds into the TAO crystal structure was completed using the VINA docking software [193] (implemented on www.mcule.com, using VINA-Autodock) onto the crystal data containing ascofuranone derivatives (PDB code:3VVA) to ensure that the docking process would not be hindered by residue displacement. Docking was centred around the area of the hydrophobic cleft closest to the di-iron centre, and a box of 22 Å was defined as the area into which the binding ligands must fit. Poses were evaluated via both Z-score and by eye, discarding poses that were either facing the wrong direction or were binding within the di-iron centre. The validity of this docking method was confirmed using the crystal structure of TAO with colletochlorin B (PDB code: 3W54), whereby the docked inhibitor was binding to the same residues.

The position of the aldehyde does not appear important for docking purposes, but could potentially be important for the inhibitory mechanism. 180° rotation of the head group for ascofuranone gave Z-scores or 9.7 and 9.6, demonstrating no selectivity between phenolic groups from an electronic standpoint. A rotation along

the axis retains the positions of the phenol groups in the 4 and 6 positions, which would suggest that these are more important for the docking then the position of the aldehyde.

The values obtained for Z-scores roughly follow the trend for potency of inhibition, with the exception of ascochlorin. While ascochlorin contains the same pharmacophore as the other compounds, attempts to dock it into the same space proved unsuccessful. It is likely that this is a feature of computational attempts to bind the tail to residues towards the entrance of the cavity (Tail carbonyl → T186), as opposed to focusing on the binding of the head group.

While experimental evidence has demonstrated that acetylation of the colletochlorin B reduces the inhibitory properties considerably (into the micromolar range) it does not affect the docking score by the same degree. Similar results were found with azoxystrobin, whereby a score of -9.3 should make it one of the more potent inhibitors, however assays against *A. maculatum* mitochondria indicated there was no inhibition of AOX in the µM range. These results are likely due to the fact that while the compound is able to fit into the internal cavity, it is unable to pass the cavity bottleneck caused by L177 and L267 except under unfavourable conformations.

The docking process did not take into account regions which it considers ligands, such as the diiron core in AOX, and the haem groups in the bc_1 complex. As such no electronic properties of metal ions are taken into account, which would affect the ability for the compounds to bind. Removal of the di-iron centre from AOX gave the docking programme access to the carboxylate cluster to which it was preferentially binding compounds. There were similar problems encountered with the docking in the bc_1 complex, with a number of compounds binding into the large cavity where the haem would be located. As such, the results collected were unreliable and have not been included in this thesis.

5.7 Summary

The pharmacophore and function of the linker tail have recently been confirmed independently [115] with respect to the inhibition of TAO. This study indicates that

while the furanone ring is not necessary for inhibition, it aids in differentiation between AOX and the *bc*$_1$ complex. While it does increase the potency of the compound towards the plant alternative oxidase, results from this study suggest that its primary function is to prevent ascofuranone from binding to the cytochrome *bc*$_1$ complex.

Comparison of the plant AOX and TAO results suggest that there is a difference in binding sites. Using ascofuranone as the template, results from the trypanosomal assays demonstrated only a small increase in concentration required of colletochlorin B to reach the IC_{50}, while the assays completed against plant mitochondria required a 10-fold increase in concentration. These differences are unlikely to confer a difference in reactivity towards quinols, given that they are from the tail end of the compound and do not enter the active site themselves. The ascochlorin data for plant AOX is consistent with the 10-fold increase required in TAO [115]

One of the more prominent uses of inhibitors for probing enzymatic systems is that the types of inhibition give insight into the binding site, and therefore the sites of substrate interaction. While colletochlorin B gives a mixed inhibition type, this could more be a function as to how it interacts with the protein itself. Analysis of the crystal structure with ascofuranone derivatives indicate that there are no covalent bond formation, while the aldehyde resides close to the proposed redox active tyrosine. Under the same assumptions found with the quinol binding discussed in chapter 3, it would suggest that colletochlorin B interacts in a similar way to quinol, in that it is only able to bind fully when the di-iron core is in the correct configuration. The loss of inhibitory efficacy with both acetylation of the hydroxyl groups and reduction of the aldehyde would suggest that both are important for binding within the active site, with the OH group para to the aldehyde allowing the compound to act as a mimentic to the quinol.

Unfortunately colletochlorin B has been found to be lethal within the mouse model, and as such would not be suitable for treatment of HAT. This is likely due to the potency of the compound towards the cytochrome *bc*$_1$ complex, and as such ascochlorin would likely also prove fatal towards the host. This does not preclude the two compounds from use as a fungicide, given that they both have increased

inhibition of cytochrome bc_1 activity compared to azoxystrobin, while also conferring inhibitory efficacy towards alternative oxidases.

The higher slope coefficient for ascochlorin and colletochlorin B relative to azoxystrobin could prove advantageous for use as a fungicide. The tighter curve reduces concentration differences from no inhibition to no activity, reducing the likelihood of necessitating point mutations within the cytochrome bc_1 while in the field. From an evolutionary standpoint, if the protein exist in either a fully functional or inactive state, there is no selective driving force for point mutations to become a dominant species within the fungus until the respiratory chain is fully inhibited.

Unfortunately preliminary plate assays demonstrate that the common G143A mutation within the cytochrome bc_1 complex is detrimental to inhibition via colletochlorin B, but the nature of the assay system cannot demonstrate to what extent. Further testing on these mutations would prove useful insight as to whether it is as detrimental to the inhibitory properties of colletochlorin B as azoxystrobin.

6 The active site and mechanistic considerations for the alternative oxidase

6.1 Introduction

The recent success in crystallisation of the AOX [11] allows for a much more detailed investigation of the active site and highly conserved residues then has previously been possible. Structural predictions that the protein contains a non haem di-iron centre surrounded by a 4-helix bundle [134, 135] have proven to be correct, with the metal core ligated by 4 glutamates and 2 histidines. These structural features confirm the addition of AOX into the di-iron carboxylate superfamily, alongside other oxygen reductive species such as methane monooxygenase (MMO),ribonucleotide reductase (RNR) and rubrerythrin (RBR). Given the wealth of information available on these complexes, the discussion within this chapter will be focused on comparisons between AOX, MMO and RNR.

While the structures of these proteins are similar they are able to undergo very different reactions. MMO uses the oxygen to generate a high valent Fe(IV) state for the conversion of methane to methanol, a reaction that has garnered much scientific interest due to its catalytic conversion of a volatile gas into a transportable liquid at room temperature, while RNR uses the core to reduce ribonucleotides through to deoxyribonucleotides for use in DNA synthesis.

Full reduction of oxygen through to water requires 4 electrons and 4 protons. The use of a bimetallic centre allows for all 4 of the electrons to come from the metal centres themselves, from an Fe(II)/Fe(II) state to two Fe(IV) states.

This chapter contains an overview of a selection of the di-iron family and their catalytic mechanisms. Comparison of the AOX structure to those of the known proteins allows for extrapolation of regions of potential mechanistic importance, thereby facilitating a prediction of the catalytic mechanism using data previously generated alongside the data generated throughout this thesis.

6.2 Function of the di-iron core in other proteins

MMO

$$CH_4 + O_2 + NAD(P)H + H^+ \rightarrow CH_3OH + H_2O + NAD^+$$

The overall function of soluble MMO (sMMO) is to utilise molecular oxygen for conversion of a variety of hydrocarbons to alcohols, with a preference for methanol [194], with a reducing equivalent of NAD(P)H being utilised to provide the final 2 protons and electrons for completing the cycle.

The structure of sMMO consists of 3 subunits; a reductase (MMOR) a hydroxylase (MMOH) and a coupling subunit (MMOB). The di-iron core is contained within the MMOH protein arranged in an $(\alpha\beta\gamma)^2$ dimer configuration [195], and is the centre for reactivity for both oxygen and methane. More recent work on the MMOB protein suggests that it controls substrate entry into the MMOH active site, with binding of MMOB to MMOH causing conformational changes that allow access to the di-iron core for both methane and oxygen [196].

RNR

$$NADH + O_2 + H^+ NDP_{ox} + Fe^{II} \rightarrow NAD^+ + 2H_2O + NDP_{deoxy} + Fe^{III}$$

RNR catalyses the reduction of ribonucleotides to deoxyribonucleotides for use in DNA synthesis [197], using the reduction of oxygen in its metal centre to generate 2 sulphur based radicals. The structure of RNR is divided into two sections, a substrate reactive centre (R1) with an oxygen reaction bimetallic centre (R2), with the most active form being a stoichiometric cluster of subunits.

RNR can be divided into 3 main classes dependant on metal cofactors and their interaction with molecular oxygen. An extensive review on the differences between

classes from Tomter *et al.* [198] covers the differences between radical generating clusters in detail. Class 1 enzymes are the closest to AOX, since it uses a redox active tyrosine close to a metal centre. Class 1 can further be divided based on the metal cofactor in the R2 subunit, with class 1a containing 2 irons, class 1b containing both iron and manganese and class 1c with two manganese ions. The discussion of RNR will be focused on the class 1a subunit, given the similarities to AOX.

Within the class 1 enzymes, the R2 subunit is used as a radical generating cluster, utilising molecular oxygen to generate a tyrosyl radical within the iron core. The radical is transferred to subunit R1 via long range PCET to reduce a disulfide bond, which in turn acts as the reducing equivalent for ribonucleotides. The network itself consists of a tyr-asp-his-asp-tryp short range network within the R2 subunit, where transfer of the radical species is believed to be stable upon the tryptophan. The radical species is then transferred into the R1 unit via a series of tyrosines, where it is able to reduce the disulfide bond. While the transfer between subunits would be greater than the 14 Å maximal distance for electron tunnelling, docking models between the subunits suggest that there is transient movement that would shorten the distance to within electron tunnelling distance, but exact values depend on the docking procedure used. The PCET network is discussed in detail by Stubbe *et al.*[199].

Rubrerythrin

$$H_2O_2 + NAD(P)H + H^+ \rightarrow NAD^+ + H_2O$$

Rubrerythrins (RBR) are involved in the oxidative stress response in anaerobic bacteria and archae, demonstrating an ability to reduce both oxygen and hydrogen peroxide through to water [200], with increased activity towards the later. Confirmation of an oxidative stress role was shown by deactivation of RBR increasing susceptibility of *Porphyromonas gingivalis* to both oxygen and peroxide [201].

A number of structures of rubrerythrin are available, and are the most simplistic of the di-iron proteins used in this thesis. The C terminal region contains a rubredoxin like FeS_4 domain that is involved in single electron transfer, and the N terminal region is made solely of the common 4 helix bundle containing the di-iron core. Reverse RBR (revRBR) features a reversal of subunits within the structure, with the FeS_4 domain in the Nterminal region [202]. As with RBR, revRBR demonstrates a preference for H_2O_2 over O_2 [203], but also shows increased levels of activity towards oxygen compared with its RBR. The preference for H_2O_2 over O_2 has been attributed to the location of additional glutamate within the active site of the protein [200], although there is no clear reason as to why this would affect catalytic preference.

6.3 Comparisons of the oxidised forms of di-iron proteins

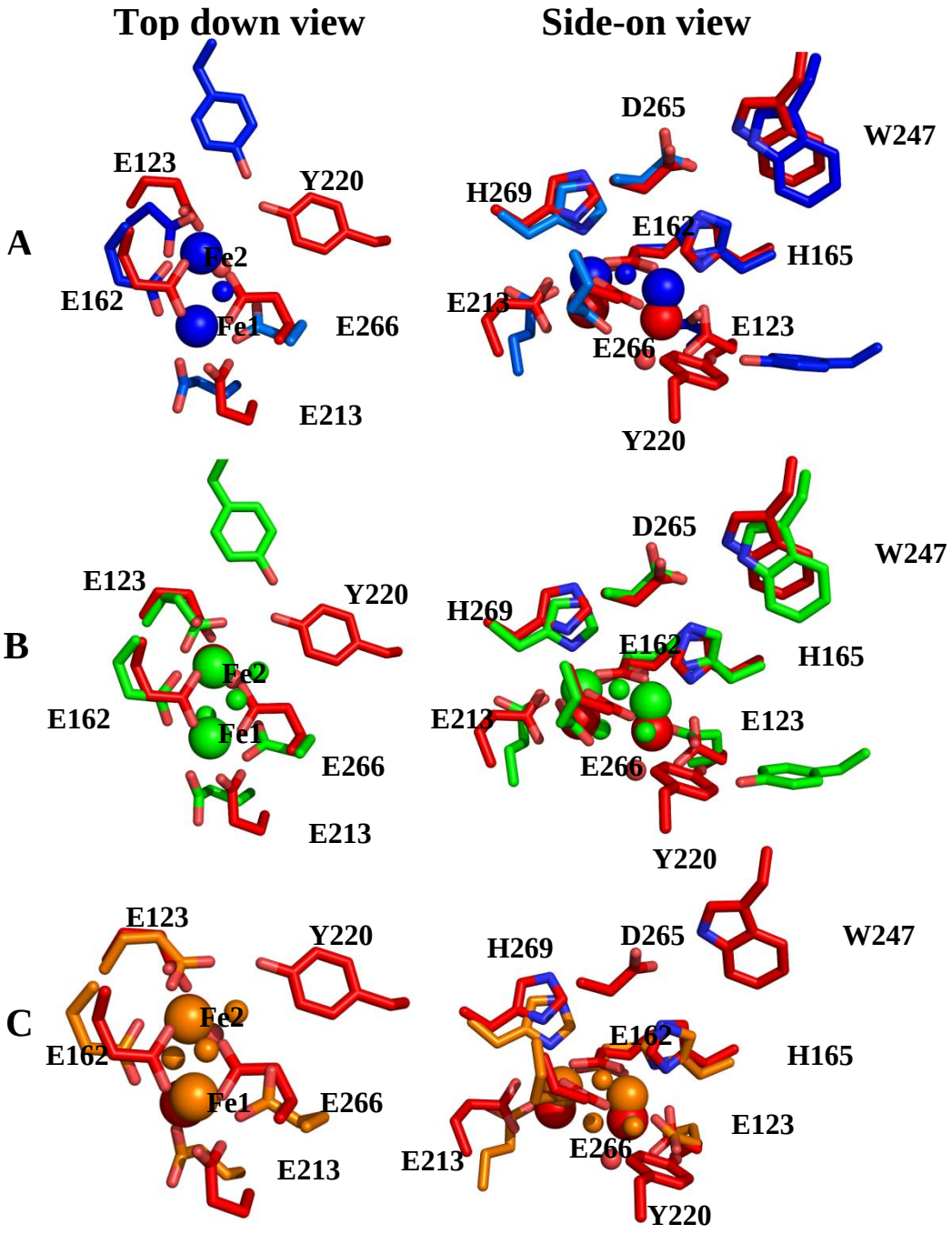

Figure 6-1:-Oxidised di-iron core of AOX aligned to; A: RNR (PDB:1RIB), B: RNR D84E (PBD:1PIU)and C : MMO (PDB: 1MTY). AOX is shown in red, RNR wild type in blue, RNR D84E in green and MMO in orange. Alignment performed according to best fit with respect to the iron binding ligands. Atoms coloured according to element, with oxygen shown in red and nitrogen in blue, with the exception of the di-iron core (large spheres) and ligating oxygens (smaller spheres), which were coloured according to crystal structure for visibility. Histidines removed from the top-down view for clarity. TAO numbering added for orientation purposes.

Iron core ligation

Monomer	E123 (Fe2/Fe2)	E162 (Fe1/Fe2)	E213 (Fe1/Fe1)	E266 (Fe1/Fe2)	H165	H269
AOX	2.2/2.0	2.5/2.3	2.3/2.5	2.0/2.1	3.3	4.4
RNR	2.2/2.5	2.0/1.8	2.1/NB	2.1/NB	2.1	2.3
RNR D84E	2.2/2.9	2.2/2.1	2.1/NB	2.0/NB	2.4	2.1
MMO	2.0/NB	2.6/2.2	2.1/NB	2.0/NB	2.2	2.1
RBR	2.1/2.3	2.0/2.2	2.2/2.2	2.1/2.0	4.1	2.2

Table 6-1:- Bond distances in Angstroms for Iron ligation sphere relative to the TAO numbering system. NB signifies no second bond towards to metal centre for that ligand.

While sequence comparison was a useful tool for identifying conserved residues within a protein family, alignment of the appropriate subunits of the di-iron family shared limited motifs. Structural alignment is a more useful tool for analysis of the protein configuration when compared to its closest relatives, with overlays of the AOX against MMO and RNR shown in Figure 6-1. While the primary ligation sphere of RNR differs by the use of a terminal bidentate aspartate ligand, a crystal structure is available of the D84E mutant, making it analogous to the other structures.

One of the most immediate features that can be seen in Table 6-1 is that AOX is the only protein where the irons are not ligated to either histidines, with the RBR ligation sphere only containing 1 histidine. What is more apparent from the overlays is that the relative positions of the irons is much lower within the active site relative to MMO and RNR, indicating that lack of ligation is not due to movement of the histidines but of the iron molecules.

One of the structural motifs discussed in Chapter 3 was the hydrogen bond network between W247, D265 and H165. This structural motif is also present RNR, where it has been demonstrated to be involved in a proton coupled electron transfer from subunit R1 into the di-iron core of R2 [199, 204]. The structural overlay shown in

Figure 6-1 shows relatively good overlap between these features in AOX and RNR, suggesting that this structural motif may play a similar role.

While it would be tempting to speculate that a similar PCET would happen within AOX, there are a number of factors that would suggest that this is not the case. Migration of the iron away from the histidine coupled with the bidentate nature of the terminal glutamate effectively breaks the chain to the tyrosine. There is also a lack of an electron hole pair that would act as a driving force for electron transfer over long distances, which in the RNR system is provided by the disulphide bond. However it has been demonstrated in the purified R2 unit that it is able to hold a radical charge [205]. The mutation of Y246 in the SgAOX system also proved non-fatal to protein activity [175] (Y299F from Chapter 4), and given the importance of the tyrosine in maintaining the position of the tryptophan it would suggest that even if this motif is present for PCET purposes it is a non-essential side reaction to normal AOX function. Removal of the tyrosine anchor point would effectively leave the tryptophan radical in limbo if it was to undergo PCET. It is also possible that the radical formation on the tryptophan is transient in nature, since in R2 there is evidence that W48+* forms and decays prior to the formation of Y* [205]. The disconnect of the histidine from the iron during the catalytic cycle would suggest that this motif is required for mediation of electron density changes during oxygen binding similar to that observed within RNR, with the iron migration preventing the generation of a tryptophan radical later in the cycle.

6.4 Potential reduced structures

Fully reduced forms of known proteins

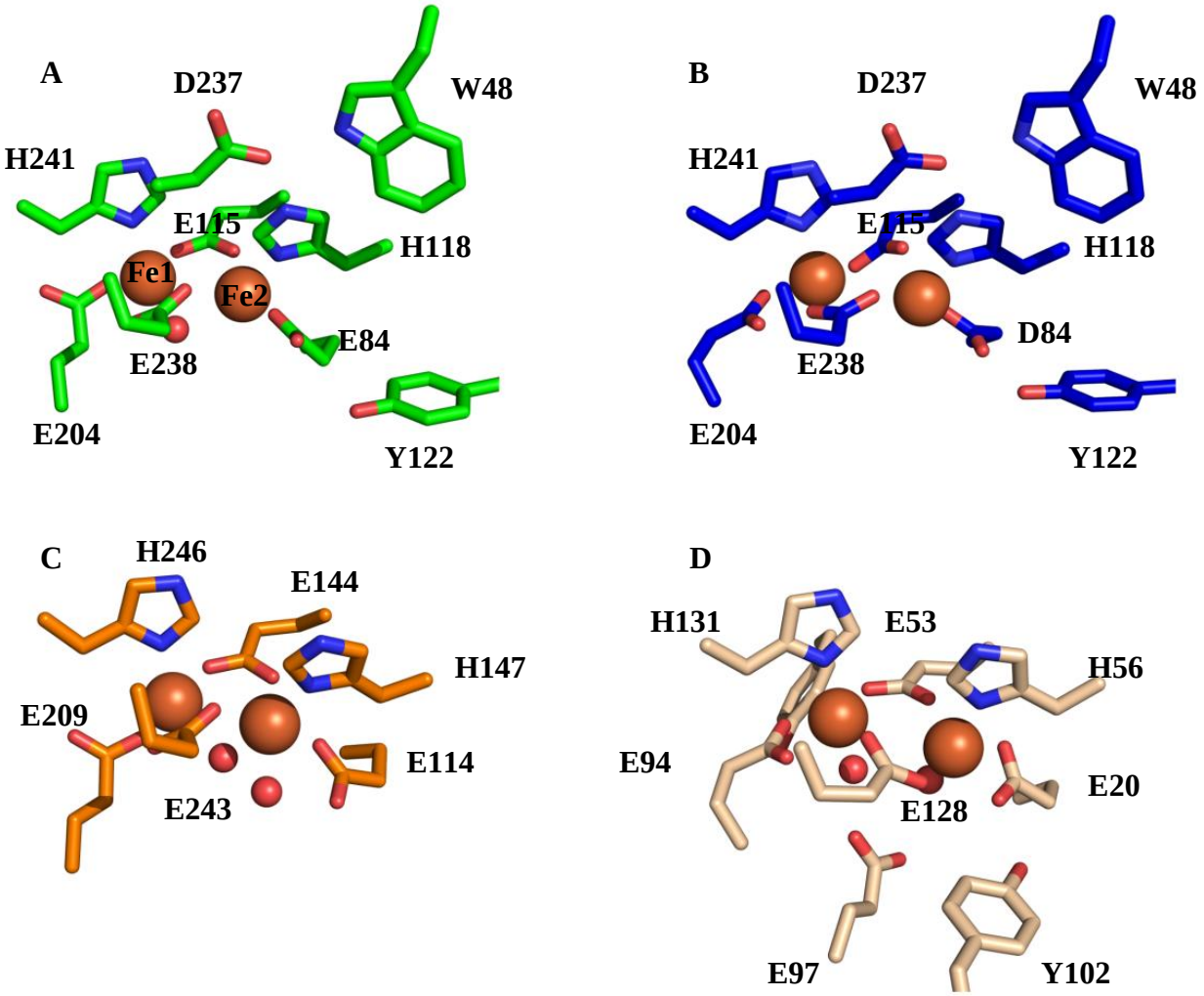

Figure 6-2:- Di-iron core of fully reduced species. A: RNR-D84E mutant (PDB: 1PIM) in green, B: RNR wild type (1R56) in blue, C: MMO (PDB:1FYZ) in orange and D: RBR (PDB:1LKO) in wheat. Heteroatoms coloured with blue being nitrogen, oxygen being red, and iron as orange spheres. Numbering indicates amino acid position in respective protein.

Figure 6-2 shows the fully reduced active sites of the di-iron carboxylate proteins discussed. While the fully reduced form of AOX is not available at present, examination of the known features available can allow for prediction of active site

configuration with respect to how they alter the structure around MMO. Alignment of the structures (not shown) revealed that the iron positions are not as variable as could be seen with the oxidised forms of the protein, with all iron atoms being ligated to their respective histidines.

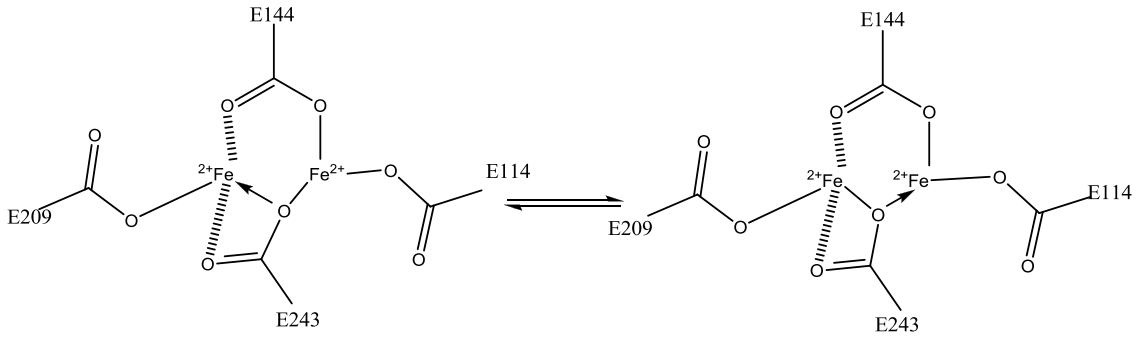

Figure 6-3:- Arrangement of carboxylates around the reduced MMO core, showing the bridging system and probable spin exchange for E243

The MMO structure shown in Figure 6-3 contains 2 bridging carboxylate ligands, with E144 bridging monodentate to each iron, whereas E243 binds in a bidentate fashion to Fe1 and a monodentate to Fe2. Both terminal carboxylates are monodentate to their respective irons, with E114 ligating to the water within the active site. The octahedral geometry around both iron cores is capped with a bridging hydroxide ion.

The RNR has significant differences from the MMO structure, in it contains two bridging ligands (E115 and E238) that are monodentate to each iron atom. E204 has also transferred to a bidentate binding mode, and D84 adopts a pseudo-bidentate binding mode, with one oxygen also in hydrogen bonding distance to the proximal tyrosine. Both irons are in a square based pyramidal geometry, with a lack of either water or hydroxide ions capping the structure.

What is interesting about the D84E mutant is that the effects of mutation are translated through the active site. Increasing the carbon chain of the carboxylate by one increases the degrees of freedom, allowing for a bidentate binding mode. The effects of this can be seen in the position of the tyrosine, whereby it no longer appears hydrogen bonded to the glutamate. E204 has adopted a monodentate binding

mode, with the bridging E238 moving to bidentate around Fe1. Addition of a hydroxide forms an octahedral complex around the iron centre, thereby adopting geometry similar to that seen in MMO.

What is apparent from the RBR structure is that the tyrosines in the secondary ligation sphere have little apparent effect on the primary ligands. While both tyrosines are within hydrogen bonding distance to their glutamate counterparts, both ligands are adopting a bidentate binding mode, demonstrating that the electronegativity of the iron atoms have a greater draw on carboxylate positions. The symmetry of the structure is also of note, with all carboxylate ligands binding in a bidentate fashion and a tyrosine found on either side of the core.

Given the lack of effect that can be seen of the tyrosine in the RBR structure, it is highly likely that the core of the fully reduced AOX protein will resemble that of the RNR-D84E mutant. Comparison between the two RNR structures presented demonstrates that the increase of the carboxylic acid by a single CH_2 unit has a greater effect on the overall architecture of the active site then the addition of the tyrosine in RBR. The PCET network is also likely to affect the electronic properties of the iron, making the D84E structure more representative then the MMO core.

Relevance to AOX

With only one oxygen visible in the active site of the crystal structure, it is more likely that there is a full 4 electron reduction of oxygen prior to addition of quinol. If the fully reduced form of the protein is closer to that or RNR, lacking the bridging hydroxide moiety, then the reduction of oxygen through to hydroxide and water still requires 3 electrons and 3 protons to reach the crystallised form. The conversion of 2 mono-dentate to bi-dentate carboxylate ligands frees two protons and allows for the metal centre to mediate oxidation states via the loss of electrons. The proposed redox active tyrosine is also liable to donate a proton and electron into the reaction, with the fourth proton either being donated through the proton bonding network, or donated via a quinol.

6.5 Mechanism of oxygen activation

6.5.1 MMO

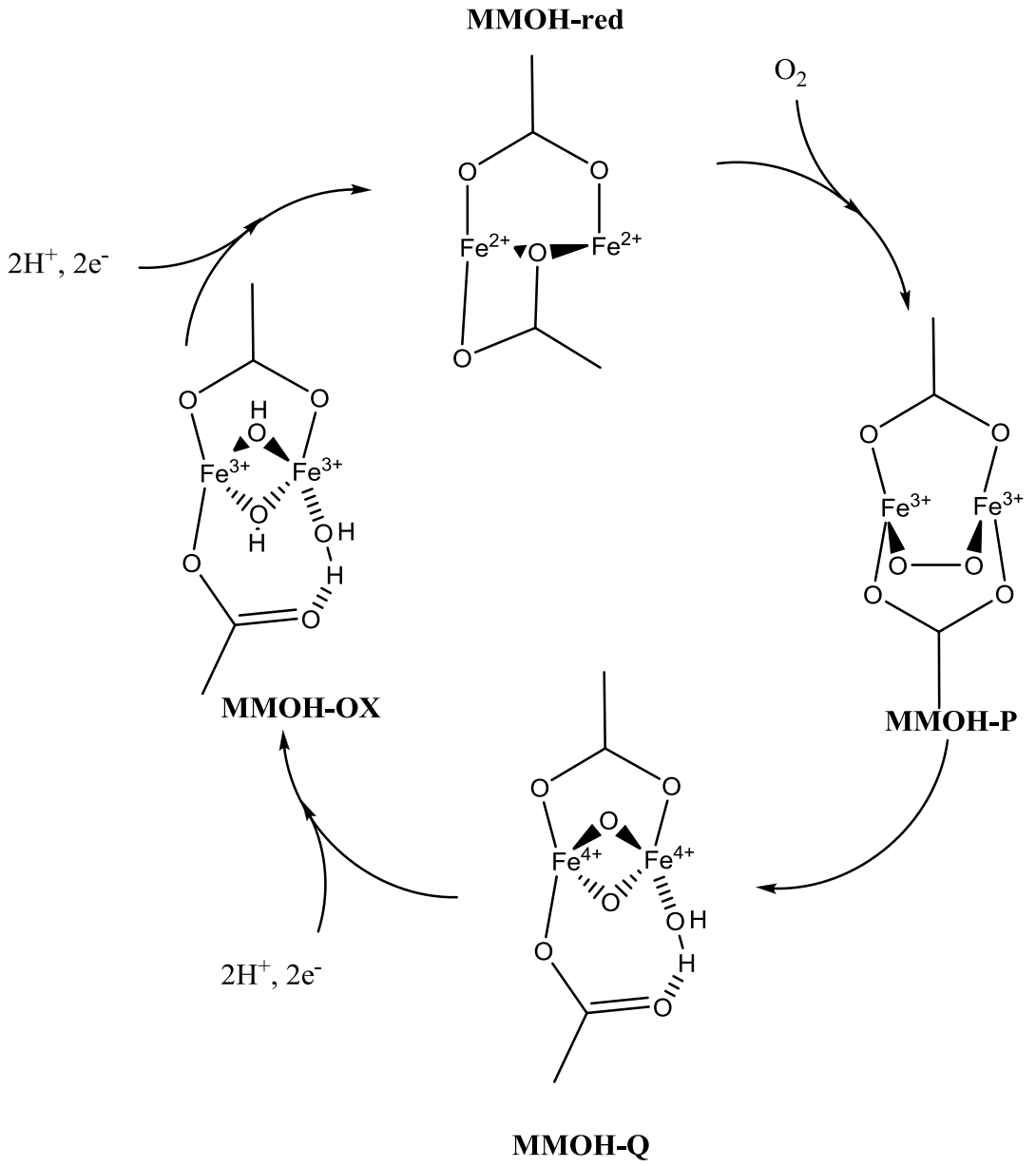

Figure 6-4:- Schematic representation of oxygen reaction cycle in soluble methane monooxygenase, adapted from [206]. Intermediates MMOH-P and MMOH-Q are predictions based on spectroscopic evidence, with MMOH-red and MMOH-OX from crystal structures 1FYZ and 1MTY respectively. Only bridging ligands shown for clarity.

The mechanism of oxygen reduction within the MMOH subunit has been examined in detail by a number of groups, with a thorough review available from Tinberg and colleagues [206].

The fully reduced species is the oxygen reactive centre, generating a cis μ-1,2 peroxodiiron(III) species (MMOH-P). MMOH-P has been well characterised, showing distinct bands at 420nm and 720nm [194] that correspond to a ligand to metal charge transfer from the peroxo species. Computational studies suggest that the initial reaction of MMOH and oxygen leads to the generation of a superoxo species [207]. MMOH-P is thought to be the methane reactive substrate, with generation of MMOH-Q being the result of a lack of hydrocarbon substrate.

MMOH-Q is the product of O-O bind cleavage, signalling the full reduction of oxygen. The structure of MMOH-Q is less defined then that of MMOH-P, with the most commonly proposed arrangement being a "diamond core" of oxygen around two Fe(IV) centres, proposed due to a short inter-iron distance of 2.46 Å and short Fe-O bonds of 1.77 Å determined via Mossbauer analysis [208]. MMOH-Q has two UV absorption peaks from stop flow spectrometry at 320nm and 420nm [209]. Interestingly computational studies of ToMOH-P in toluene monooxygenase suggest that the peroxoide species migrates from a cis μ-1,2 peroxodiiron(III) to a μ-1,2 peroxo species that interacts with a threonine within the active site, preventing its degredation to a similar Q type intermediate [210]. MMOH-Q has been demonstrated to also be a reactive species, demonstrating an ability to react with a variety of hydrocarbon substrates [194, 211].MMOH-OX is the product of reaction of either MMOH-Q or MMOH-P with methane, and is also the form of the reconstituted apo protein with Fe(III). Regeneration of the fully reduced form from MMOH-OX is facilitated via electron transfer from NAD(P)H via a thioredoxin, although and exact mechanism has not been established.

6.5.2 RNR

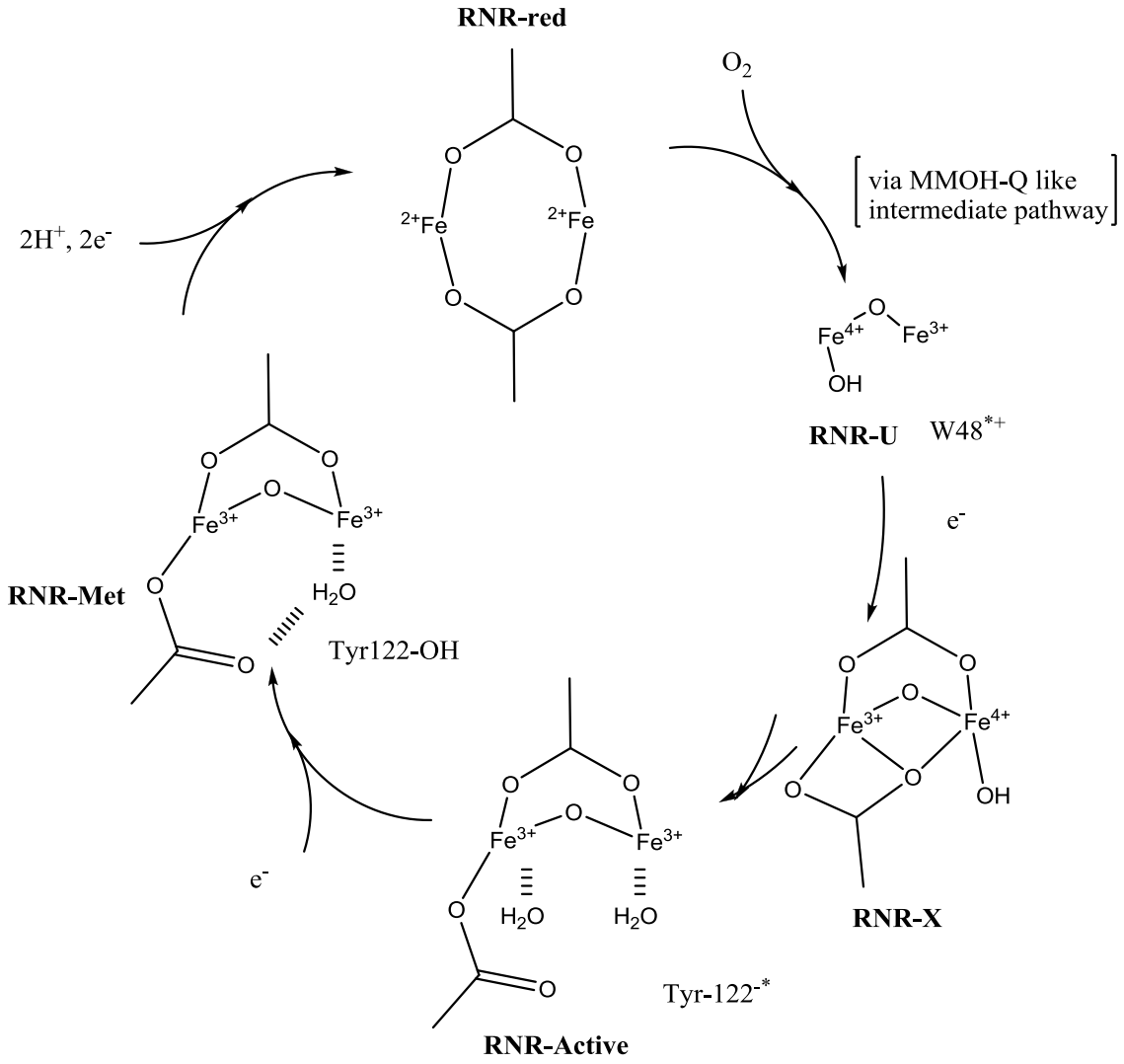

Figure 6-5:- Oxygen reductive cycle at the RNR-R2 subunit, adapted from [212]. RNR-red and RNR-active from crystal structures 1R56 and 1RIB respectively. Terminal iron binding glutamates removed for clarity.

The oxygen binding in RNR is thought to mimic that of the MMOH oxygen binding pathway, with RNR-U the intermediate generated after MMOH-P and MMOH-Q type intermediates have formed and decayed. While there is no direct evidence for this, there is indirect evidence in the form of a build up of a cis μ-1,2 peroxodiiron species in both the D84E [213] and W48F mutants [214]. Cleavage of the O-O bond to form RNR-U is thought to be a result of the electron and proton donation from W48.

RNR-U was characterised via reconstitution reactions with sub-stoichiometric amounts of iron, The electron provided for the conversion of RNR-U to RNR-X is provided by exogenous Fe(II), likely transferring directly to the W48 radical on the proteins surface [215]. The decoupling of the tryptophan radical from the di-iron centre allows for a carboxylate shift to form RNR-X, with transfer of a proton and electron from the neighbouring tyrosine allowing the active form of the protein to form. The radical formed on tyrosine is subsequently transferred via the PCET to a cysteine in R1 to catalyse the reaction with ribonucleotides. The final reducing equivalents are provided via an NAD(P)H thioredoxin system to regenerate the reduced state [216], although the exact mechanism is unknown at present.

A number of structural mutants of RNR which have been studied are relevant to AOX. The aforementioned D84E mutant led to a build-up of the cis μ-1,2 peroxodiiron species similar to the MMOH-P intermediate. One potential for this buildup is the lack of co-ordination between the tyrosine and the glutamate prevents electron transfer towards the di-iron core.

One of the more interesting mutations created was the F208Y [217]. The phenylalanine occupies the same special region as the tyrosine within AOX, conversion to tyrosine within the RNR structure generated DOPA, a meta-substituted oxygen onto the tyrosine species. While this is not directly analogous to AOX given that the RNR mutant still contained Y122, it implies that addition of the hydroxide moiety onto the phenylalanine leads to a definitive change in the reactivity of the oxygen reduction cycle in the direction of this spatial region.

6.5.3 Rubrerythrin

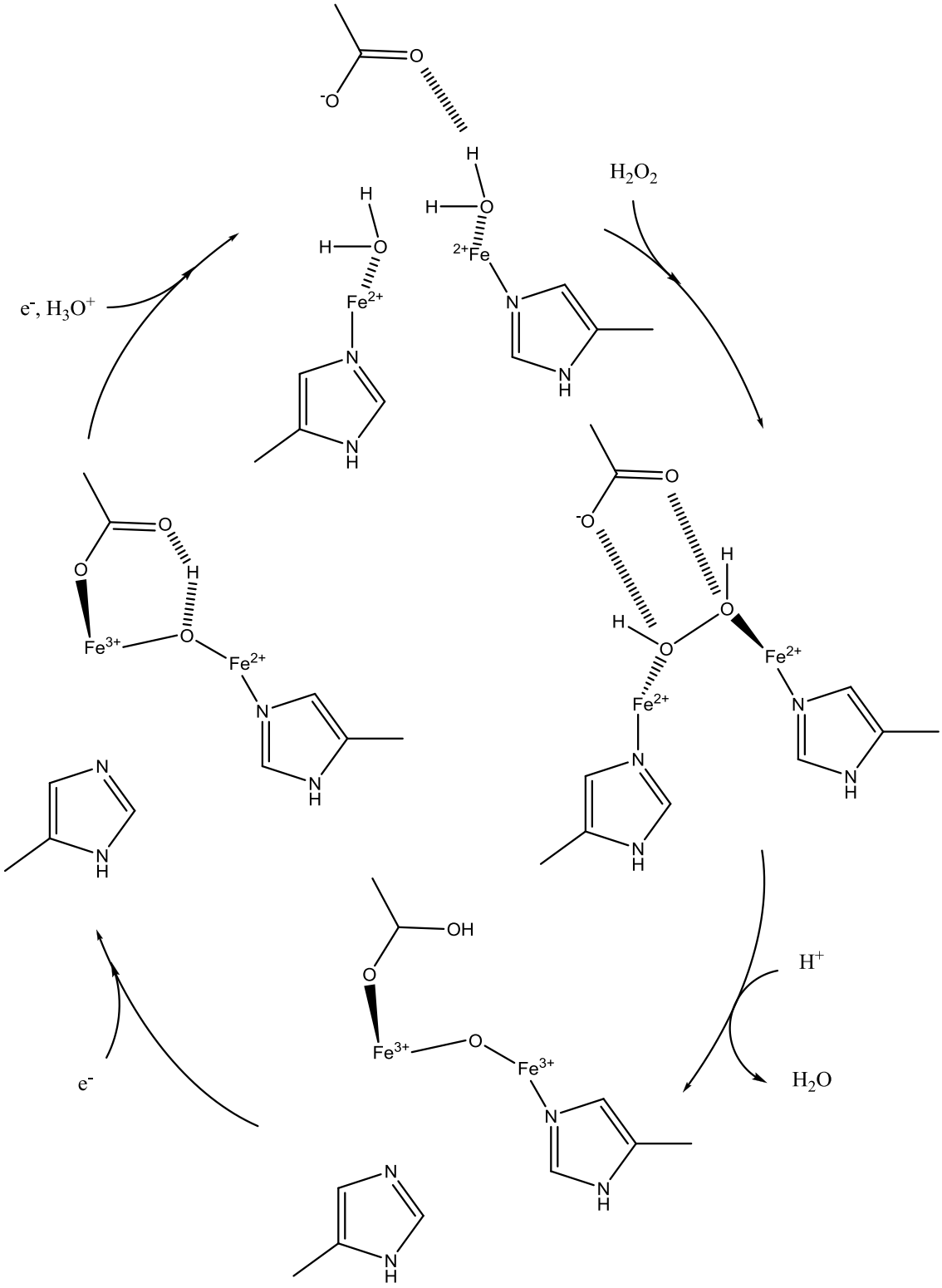

Figure 6-6:- hydrogen peroxide reduction cycle for rubrerythrin, adapted from [218]. Peroxide initially binds to the fully reduced structure, with successive electron donation from the FeS_4 liberating two molecules of Water. Iron binding glutamates have been removed for clarity.

The mechanism for oxidation of the di-iron site within rubrerythrin has been extremely well characterised via cryo-crystallographic time course studies upon a protein that is usually found active at 100°C [218]. While the mechanism studied is of hydrogen peroxide as opposed to oxygen, the migration of iron makes it an interesting case-study.

Peroxide was shown to bind in a cis μ-1,2 fashion similar to that proposed in the activation of MMOH, but due to the lack of reduction remains in the diferrous state. The co-ordinating glutamate shown in Figure 6-6 is found in the same region as the tyrosine within AOX, and has been proposed as the basis for its preferential reactivity towards peroxides over oxygen [218]. Acidification of the peroxo species leads to the loss of water and ligation of the iron to the proximal glutamate. Dillard and colleagues do not make it clear as to whether this is the formation of a formal covalent bond, and therefore reduction around the carboxylate centre, or simple co-ordination through the oxygen lone pair.

The electron donations shown on the left hand side of the diagram are from the FeS_4 via the histidine, first forming the mixed valent Fe(III)Fe(II) species before regeneration of the fully reduced state. Electrons are donated to the cluster from NAD(P)H via a rubredoxin oxidoreductase (NROR) cofactor.

The mechanism for oxygen reduction within rubrerythrin has not been studied in detail, as it is considered a side reaction for the protein. From a structural perspective, it is worth noting that there are two tyrosines in close proximity which are arranged symmetrically around the di-iron core that have not been utilised in the reaction with H_2O_2. These two tyrosines could potentially donate the two extra electrons required for the full reduction of oxygen. It could also be the case that only one of the tyrosines is used, and the second is there for redundancy purposes. Given the highly symmetric nature of the active site, there is no preferential driving force directing reaction of oxygen to either iron atom.

6.6 Proposed mechanism for reduction of oxygen via AOX

Oxygen reactive species

Parallel mode EPR has shown that the fully reduced state of plant AOX is spin coupled, with two high spin irons coupled via a hydroxo bridge [142] giving a g-value of 16.4. Electrochemical FTIR studies [219] have demonstrated that this is the oxygen reactive species, which upon oxidation undergoes a conformational change around the irons resulting in the deprotonation of at least 1 iron binding carboxylates and the loss of ligation of at least one histidine via N-(π) to the metal centre.
As previously discussed in section 6.4, the proposed fully reduced species of AOX would likely resemble that of RNR-D84E, given that ligand arrangement is the most similar to that of AOX and it contains the necessary features to agree with both EPR and FTIR data. The organisation of the ligands around the iron centre leaves one open ligation site on the underside of Fe1, allowing for initial reaction with oxygen generating a superoxo species, as has been demonstrated to be favourable in MMOH [207].

There is considerable evidence in favour of the mixed valent state that would be generated by the formation of a superoxo species. Upon oxidation of the fully reduced species of AOX1a from *Arabidopsis thaliana*, a mixed valent species was detected via EPR [139]. What sets this apart from the mixed valent species of RNR and MMOH is that it was found in the oxidative direction, as opposed to chemical reduction of Fe(III)/Fe(III) species in other di-iron systems [220, 221]. It is worth considering that this mixed valence species was stable enough to generate EPR data, and given the high reactivity of the superoxo species it would suggest that the terminal oxygen has been reduced in a manner that does not affect the oxidation state at the metal centres. The highly reactive nature of this species can be seen in the RNR-D84E/W48F double mutant, in which the lack of electron donation into the system causes hydroxylation at F208, a position which is occupied by Y220 in the AOX system.

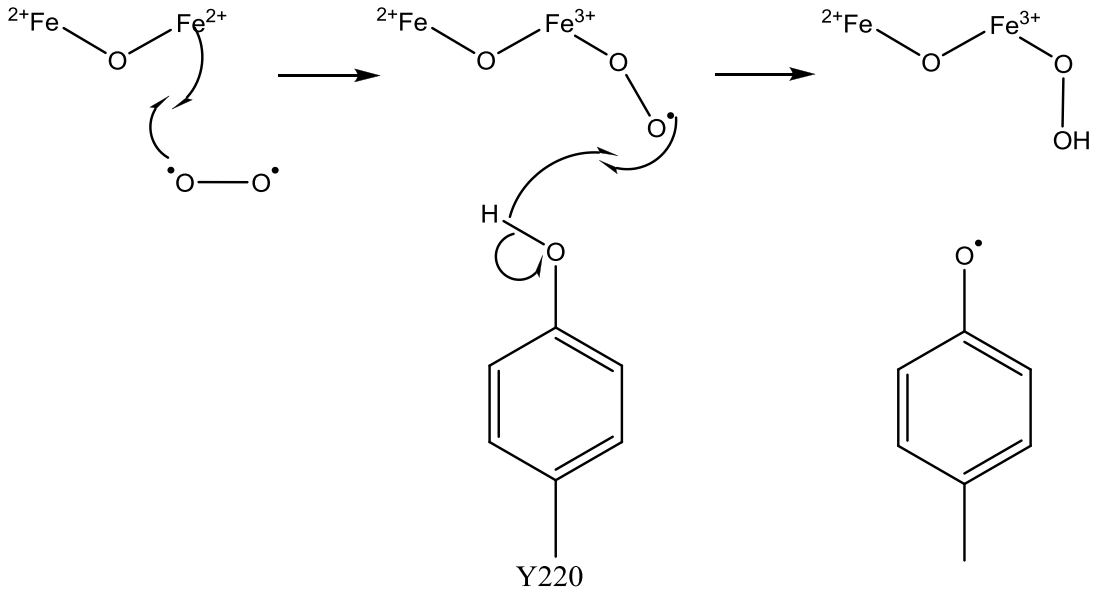

Figure 6-7:- generation of the tyrosine radical via hydrogen atom extraction after initial binding of oxygen to form the superoxo species.

An Fe(III)-O-O* superoxo species has been crystallised within dioxygenase, with bond distances of 1.99 Å (Fe-O) and 1.47 Å (O-O*) [222] . Given the Fe(1)-Tyr-O distance of 6 Å, (5 Å to the proton), a reactive distance of 1.5 Å allows for the required orbital overlap for hydrogen atom extraction as shown in Figure 6-7. $Fe(III)O_2^{\bullet -}$ has also been shown to be more reactive then its Fe(IV)=O counterpart [223], existing in the singlet state permitting for spin allowed hydrogen atom abstraction. UV-Vis experiments performed by repeated reduction by ferricyanide and reintroduction of oxygen into the sample gave rise to a characteristic signal for a tyrosine radical at 410nm, similar to that found in RNR [224]. While this would suggest that the tyrosine radical is produced upon oxidation of the di-iron centre, it does not necessarily mean that it takes place this early in the mechanism and may well be induced further into the cycle.

The newly generated Fe(III) ion would have a greater effect on the carboxylate ligating to both irons via a single oxygen, causing a carboxylate shift to a bidentate 1,1 mode. This would decrease the inter-iron distance, increasing the acidity of the bridging OH and allow for the proton transfer onto the peroxo species. The shortened inter-iron distance would allow for ligation of O1 to Fe2, allowing for cleavage of the O-O bond, and forming a diamond core similar to that seen in MMOH. Proton

transfer from the ligating carboxylate into the system would allow for the generation of Fe-O-Fe-OH, likely to be a much more stable form of the core and analogous to that observed in RNR-U.

One area that is interesting to consider is the apparent disconnection of the potential PCET at Fe1. If the generated tyrosine radical species is negatively charged as proposed, it is conceivable that the electronegativity presented is greater than that of the His-Asp-Tyrp region, causing apparent migration towards the tyrosine. For this to be the case the ligating OH would need to reside on Fe2 to prevent interaction with the tyrosine itself. It is also fully feasible from an Fe-O-Fe-OH species to generate the crystal structure under acidic conditions. Mechanistically this pathway would account for the lack of UV signals associated with the Fe(III) bridging peroxo species seen in MMOH-Q, given that it is not generated via this pathway.

Alternative route – extraction from bridging hydroxide species.

It is also feasible that a mechanism similar to that seen in MMOH is used by AOX. While the ligands around the active site would suggest that generation of a 1,2 peroxo intermediate was unlikely, the fact that its generation can be seen in the RNR D84E mutant would suggest that it is allowable, and there is indeed circumstantial evidence that would support this mechanism.

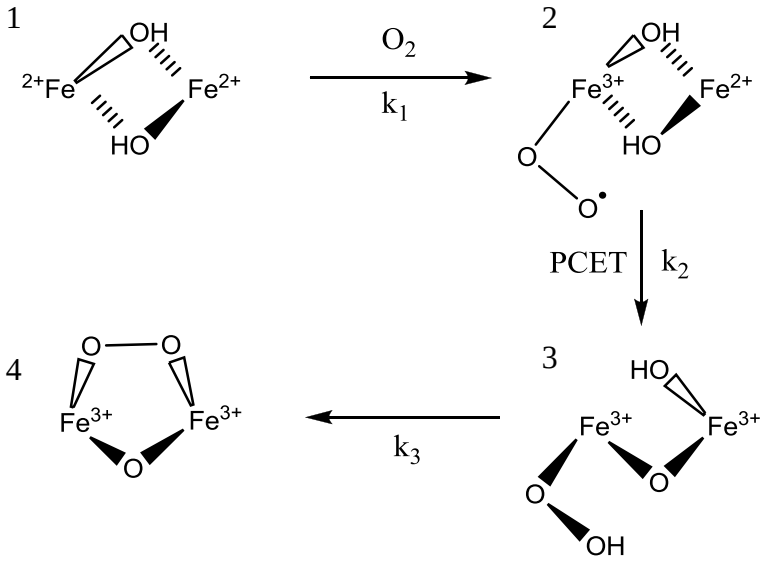

Figure 6-8:- proposed oxygen binding reaction in [Fe2(μ -OH)2(6-Me3-TPA)2], adapted from [225]. Oxygen initial binds in an end-on fashion to a single iron, before abstracting an electron and proton to form a peroxide species.

Once the superoxo has been formed a PCET similar to that seen in $[Fe_2(\mu\text{-}OH)_2(6\text{-}Me_3\text{-}TPA)_2](OTf)_2$ [225] could occur, with the proton and electron coming instead from the bridging hydroxide species. What is interesting about comparisons to this system is the apparent correlation between concentrations; the EPR data collected by Berthold [139] gave a maximal concentration of the Fe(II)/Fe(III) species of 5% of total protein, with a value of 7% calculated for the superoxo species in the model system if the rearrangement is the rate limiting factor (complex 2 in Figure 6-8). Given that this is likely to involve the movement of carboxylate ligands within the protein, it is likely that this will be the rate determining step within a protein environment.

Parallels to the ligation of oxygen within hemerythrin can be drawn with the PCET from the bridging hydroxide. Hemerythrin is one of the simplest di-iron proteins, and acts as an oxygen carrier by ligation of oxygen as a peroxide species ligated to bridging hydroxyl group[226], with no further reaction taking place. It is conceivable that donation of extra electron density from the PCET network would allow for the increased reactivity observable in the more advanced systems.

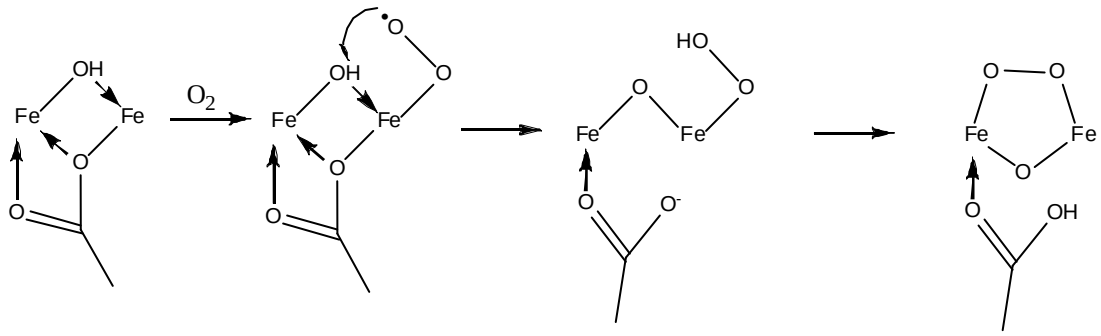

Figure 6-9: Mechanistic parallels to Figure 6-8, using a bridging carboxylate oxygen in lieu of a second bridging hydroxide species.

It is also worth considering what the identity of the bridging oxygen would be in the case of AOX; within the fully reduced species a carboxylate can clearly be seen bridging via an oxygen, and while the mechanism calls for the generation of a water molecule as a leaving group, it is more likely that protonation of the bridging carboxylate will allow it to act as a pseudo leaving group, remaining bound in via the carbonyl oxygen (depicted in Figure 6-9).

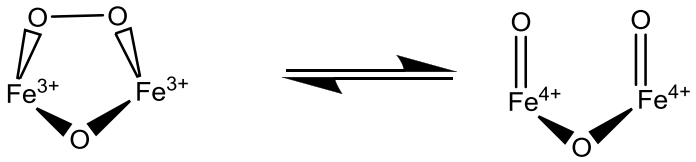

Figure 6-10: Scission of the [Fe2(μ-O)(μ O-O)] unit, adapted from [227].

The [Fe_2(μ-O) (μ O-O)] species has been demonstrated [227] to be able to undergo spontaneous rearrangement between an Fe(III)/Fe(III) species and Fe(IV)/Fe(IV) via reversible scission of the O-O bond (as shown in Figure 6-10). This reaction is dependent on surrounding acidity, with evidence that protonation of the bridging hydroxide bond increases scission rate. It is possible that the proton comes from an external source, such as via the water channel proposed in Chapter 3, or from a proximal protonated amino acid (such as the carboxylate protonated within the

previous step). The reaction could also be accelerated due to mechanical constraints on the active site; if the bridging species in the protein case is a carboxylate ligand, the increased energy provided by a ligand in a now unfavourable position may force equilibria to the Fe(IV)/Fe(IV) species.

From this species, there are a number of ligand rearrangements that are necessary to reach the oxidised form seen in the crystal structure which are not available from model ligand systems. The bridging species would need to migrate to a more favoured 1,1 bridging mode, which would vacate a binding site for the terminal glutamic acid to switch from a monodentate to a bidentate binding mode, providing a proton to the active site. This carboxylate shift also has an effect upon the pKa values of H269; examination of the pKa values using PropKa [174] show that removal of the carboxylate interactions reduce the pKa from ~10.4 to 5.9, with rotational movement allowing for further reduction to 1.7, allowing for a reasonably concerted pathway for proton transfer from solvent to hisitidine, followed by delivery to the di-iron core at the correct time. A proton and electron are also still available from the tyrosine, although attempting to facilitate transfer without the length provided by the peroxo unit would prove difficult unless the transfer occurs via one of the carboxylate ligands.

6.7 Reductive direction from crystal structure

Reduction with Quinol

Given the generation of water as part of the catalytic cycle, and evidence of the interaction between water and quinol in the cytochrome bc_1 complex [228], there is also the possibility that the transfer of protons is mediated by water generation prior to quinol acceptance into the active site.

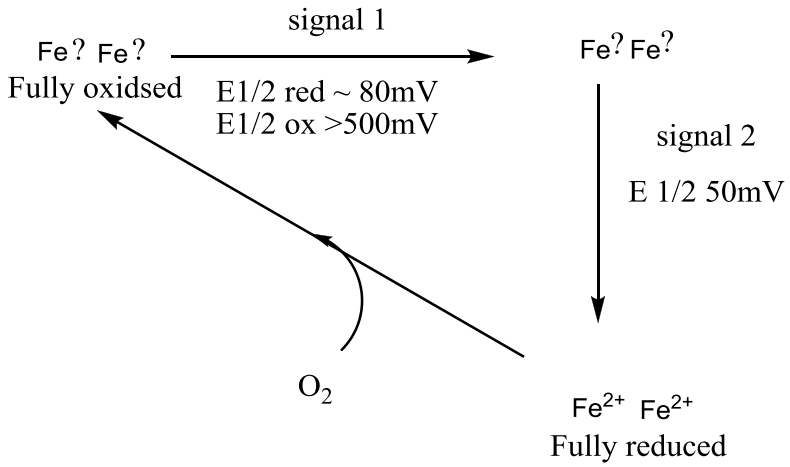

Figure 6-11:- electrochemical studies adapted from [219]. Redox potentials in both oxidative and reductive direction quoted for signal 1, with signal 2 operating under standard reversible redox conditions.

Electrochemical work performed by Maréchal et.al. [219] gives insight into the reduction steps of the fully oxidised species and is shown in Figure 6-11. Under the assumption that the two 2 electron transfer steps would correlate to two quinols, this gives two distinct intermediates that would react with quinol sequentially rather than necessitating two quinol binding sites for concurrent reactivity. The FTIR work from the paper also gave indications as to ligation sphere modifications upon reduction, with signal 1 indicating a protonation of one carboxylate ligand and the ligation of iron to histidine.

It is tempting to speculate that quenching of the tyrosyl radical would explain the electrochemical work performed. The high voltage necessary to reoxidise signal I (<500mM) coupled with the low midpoint potential in the reductive direction would be within the remit of tyrosine radical generation at pH7 (~750mV [229]). Use of the tyrosine radical would also be advantageous with respect to oxidation of the quinol, as generation of the QH* species would allow for energetically favourable decomposition of the semiquinone species to quinone with a much lower redox potential then via other oxidative pathways. Use of the tyrosine as an effective activator would also compensate for the lack of polar amino acids within the site, effectively allowing direct reduction at the iron site. Quenching of the tyrosyl radical would also rationalise the ligation of histidine seen in signal 1; if the previous

assumption that iron migration is caused by spin coupling between the iron and the tyrosine radical is correct, then quenching of the radical would decouple the spin and allow for ligation of histidine within the active site.

One of the interesting questions would be whether the crystal structure is the primary quinol reactive species, or whether it is a stable degradation product of a more reactive core. The FTIR studies suggest that the fully oxidised core is able to decompose over time to form "signal 1", but given that this could still be reduced via electrochemical means it suggests that the sources of electrons and protons are from an internal source/solvent that can be regenerated. The instability of the primary reactive core can be seen in MMO, where MMO-P will decompose to MMO-Q upon lack of substrate.

Without a structure of the semi-reduced species, any predictions for the reactivity of the second equivalent of quinol would be speculative at best. Given that the initial 2 electron reduction involves a movement of iron and protonation of a carboxylate, the large overall shift in ligand location could open up a second binding site that is impossible to predict. It is fully possible that the second binding cavity discussed in Chapter 3 is opened up, and if this is indeed accompanied by a roll on helix 1 then it may open additional options for reactivity. It is of course fully possible that the second equivalent uses the same tyrosine, with the iron migration opening room within the active site to allow for hydrogen abstraction by the iron to initiate the reaction with quinol.

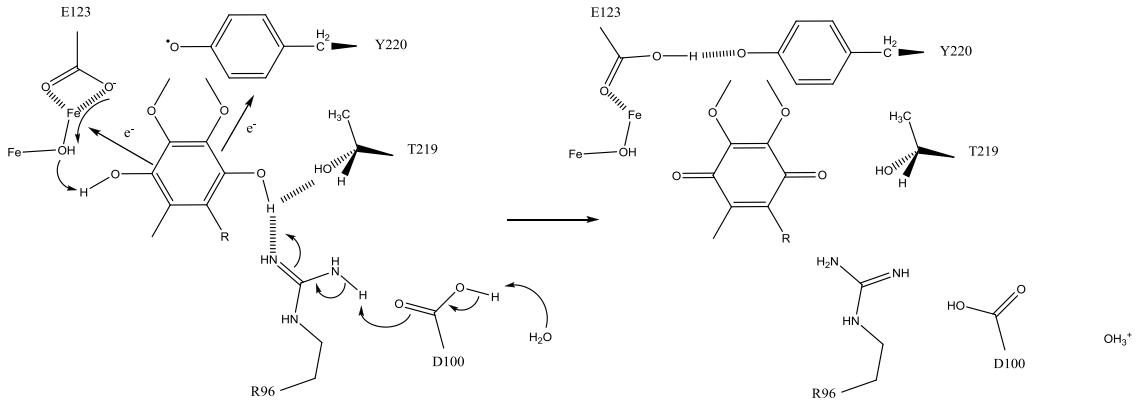

Figure 6-12:- potential quinol reduction mechanism based on the docked quinol species. Proton translocation towards the solvent facilitated via R96 and D100, with the second proton entering the di-iron active site, with a potential final resting place between E123 and Y220. Electrons transferred to the di-iron core and tyrosine respectively.

Using the docking of quinol from Chapter 3 as a model system, it would suggest that the reaction with quinol would only facilitate the transfer of 1 proton towards the iron core, with the proton likely being transferred to solvent via R118, D100 and R96, with schematic representation shown in Figure 6-12. If this is the case for both molecules of quinol, then there must be an outside source of protons that would balance the reaction stoichiometry. The water channels highlighted in Chapter 3 could facilitate the proton transfer, with the PCET network solvent accessible could potentially allow for a tryptophan radical quench to be separated from its reprotonation. Only additional experimentation will determine whether these protons are used during the oxygen reduction or quinol oxidation part of the cycle.

6.8 Summary

A number of oxidative pathways have been proposed based on other di-iron proteins that have been studied extensively by other groups. While they are presented as separate mechanisms, they share a number of intermediates and it is likely that the true oxidative pathway is a combination of the two.

The use of the PCET network has also not been used within the mechanism, as I believe that this is used to mediate the oxidative burst upon the single electron binding of oxygen, and that while the oxidation states of the metals have been stated to change, in actuality it is likely that the increase in oxidation state is buffered by the use of a tryptophan radical via this network. There is also the potential for a second transfer event from W65, which could explain the generation of a resting state from the fully oxidised form that was seen in [219]. If a proton is transferred from this region, the proximity to solvent could potentially allow it to be quenched without need for a “return trip” from the di-iron core.

A number of experiments could be performed to clarify the oxidative pathway of AOX. Stop flow spectrometry has revealed a number of salient features of the MMOH-P and RNR intermediates, and while AOX has no known UV-VIS features, use of the stop flow would shed light on whether oxidation goes via a P-type intermediate or via another pathway. It would also be interesting to determine

exactly how early in the oxidative cycle the tyrosine radical is formed, and whether a tryptophan radical is indeed generated.

The reductive pathway has also been given some consideration, but given the unpredictable nature of quinols and the transient nature of the active site upon reduction a full mechanistic prediction is impossible at this time. Docking studies that have been performed would suggest a non-concerted mechanism would take place, with 2 electrons and 1 proton being used by the protein per quinol molecule, with the remaining proton being transferred to solvent. If this is the case, then the oxygen reduction part of the cycle should demonstrate a dependency upon solvent acidity, as protons must be supplied during this part of the cycle to satisfy the reaction stoichiometry.

7 Summary

The work presented within Chapter 3 is a reasonable starting point for the examination of key residues within AOX and their potential functions within the protein. What was clear is that a considerable number of the fully conserved residues are for structural purposes but may also offer a dual role that will be difficult to probe solely using site directed mutagenesis based techniques. One region not fully explored is the nature of residues that are conserved within family groups, i.e. amino acids that are fully conserved solely across the plant species, but lack conservation within the trypanosomal or fungal variants. Examination of these residues may well give more insight into regions that are responsible for allosteric activation, specifically with respect to pyruvate activation within the plant AOX. Another comparison not fully drawn was contrasting AOX to its other di-iron ancestors, especially with respect to the PCET network. Given this region is responsible for transferring electrons from the di-iron core in RNR [199] and towards the di-iron core from an FeS_4 cluster in RBR [218],this may shed light on the nature of the network, allowing us to discern whether it has a genuine function within the protein, or an ancestral artefact that is not detrimental to the overall catalytic cycle.

While the catalytic cycle proposed within Chapter 6 has a scientific grounding within the current evidence available for AOX, there are a number of available pathways for the initial oxygen binding and cleavage that it is impossible to determine between with the currently accumulated data. One of the major problems that needs to be addressed with purified AOX is its lack of solubility above 5 mg ml^{-1}. This makes the use of analytical techniques such as stop flow and EPR unreliable due to the low concentration of sample. Given the transient nature of the tryptophan based radical within RNR [205], stop flow techniques would be necessary to confirm that the PCET network is part of the regular pathway.

There is also a distinct possibility that the correct pathway cannot be determined without the use of computational methods. Given the distinct differences between sMMOH and ToMOH [210] that were caused by a change as subtle as adding a polar contact into the active site, the difference in positions of the tyrosine between RNR and AOX could potentially alter the reaction mechanism more than has been predicted within this thesis. Further mutagenesis studies within the pocket would

allow for dissemination as to whether the main determinant on altered reactivity is due to the position of the tyrosine, the use of an iron binding aspartic acid as opposed to a glutatmic acid, or a subtle combination of the two. It is fully plausible that the tyrosine position within AOX is to allow for improved reaction kinetics with respect to quinol, which has been taken into account with the initiation of reactivity between substrate and protein being due to a tyrosine based radical.

The analysis from Chapter 3 also allows for the development of a better class of inhibitors for AOX. Given that there is full conservation within the quinol binding pocket of the polar residues, namely R96, R118, T219,Y220 (TAO numbering), a scaffold can be designed that would fit within these residues, but would not necessarily interact within the cytochrome bc_1 Q_i or Q_o sites to allow for increased specificity over that demonstrated with colletochlorin B. Mutagenesis studies presented within this thesis and in the literature [138, 145, 230] have demonstrated that the aforementioned residues are critical for continued turnover of the protein, therefore making resistance due to a single point mutation of these residues an unlikely outcome.

The differences determined within Chapter 5 in inhibition of the cytochrome bc_1 complex with respect to ascofuranone and colletochlorin B, presumably due to unfavourable interactions between the furanone moiety and the binding pocket, open up the possibility that altering functionality of the tail would improve specificity of the compound. The ability to design a suitably functionalised tail for this purpose while still remaining cost effective would likely require a different synthetic route that would allow for an increased yield for the alkylation step. While work is available within the literature as to the affects of tail functionality on inhibition of TAO [115], the same compounds were not tested against the cytochrome bc_1 complex, and may well improve specificity.

A second route that could be utilised for specific inhibitor design could be taken from the catalytic cycle itself. Given the high likelihood of a tyrosine radical within the binding pocket, the addition of a radical leaving group onto the compound could potentially allow for the design of a suicide inhibitor that would permanently reside within the active site. This would also prove advantageous with respect to specificity; given that current predictions for the quinol reaction mechanism within

the Q_o site suggest that removal of protons and electrons occur as separate events, rather than the hydrogen atom extraction that has been postulated here.

8 References

1. Nicholls, D.G. and S.J. Ferguson, *Bioenergetics 4*. [Fourth edition] ed. 2013. xiv, 419 pages.
2. Kim, B.H., *Bacterial physiology and metabolism*. 2007, Cambridge: Cambridge University Press. xxii, 529 p.
3. Rich, P.R., *The molecular machinery of Keilin's respiratory chain.* Biochem Soc Trans, 2003. **31**(Pt 6): p. 1095-105.
4. Porter, R.K. and M.D. Brand, *Mitochondrial Proton Conductance and H+/O Ratio Are Independent of Electron-Transport Rate in Isolated Hepatocytes.* Biochemical Journal, 1995. **310**: p. 379-382.
5. Mitchell, P., *Coupling of phosphorylation to electron and hydrogen transfer by a chemi-osmotic type of mechanism.* Nature, 1961. **191**: p. 144-8.
6. Efremov, R.G., R. Baradaran, and L.A. Sazanov, *The architecture of respiratory complex I.* Nature, 2010. **465**(7297): p. 441-U61.
7. Ren, A.M., K.R. Rajashankar, and D.J. Patel, *Fluoride ion encapsulation by Mg2+ ions and phosphates in a fluoride riboswitch.* Nature, 2012. **486**(7401): p. 85-U1501.
8. Zhang, Z.L., et al., *Electron transfer by domain movement in cytochrome bc(1).* Nature, 1998. **392**(6677): p. 677-684.
9. Yoshikawa, S., et al., *Redox-coupled crystal structural changes in bovine heart cytochrome c oxidase.* Science, 1998. **280**(5370): p. 1723-1729.
10. Iwata, M., et al., *The structure of the yeast NADH dehydrogenase (Ndi1) reveals overlapping binding sites for water- and lipid-soluble substrates.* Proceedings of the National Academy of Sciences of the United States of America, 2012. **109**(38): p. 15247-15252.
11. Shiba, T., et al., *Structure of the trypanosome cyanide-insensitive alternative oxidase.* Proceedings of the National Academy of Sciences of the United States of America, 2013. **110**(12): p. 4580-5.
12. Rastogi, V.K. and M.E. Girvin, *Structural changes linked to proton translocation by subunit c of the ATP synthase.* Nature, 1999. **402**(6759): p. 263-268.
13. Gibbons, C., et al., *The structure of the central stalk in bovine F-1-ATPase at 2.4 angstrom resolution.* Nature Structural Biology, 2000. **7**(11): p. 1055-1061.
14. Wilkens, S., et al., *Structural characterization of the interaction of the delta and alpha subunits of the Escherichia coli F1F0-ATP synthase by NMR spectroscopy.* Biochemistry, 2005. **44**(35): p. 11786-11794.
15. Moore, A.L., et al., *Unraveling the heater: new insights into the structure of the alternative oxidase.* Annu Rev Plant Biol, 2013. **64**: p. 637-63.
16. Brandt, U., *A two-state stabilization-change mechanism for proton-pumping complex I.* Biochim Biophys Acta, 2011. **1807**(10): p. 1364-9.
17. Efremov, R.G. and L.A. Sazanov, *Structure of the membrane domain of respiratory complex I.* Nature, 2011. **476**(7361): p. 414-U62.
18. Brandt, U., *Energy converting NADH:quinone oxidoreductase (complex I).* Annu Rev Biochem, 2006. **75**: p. 69-92.
19. Sazanov, L.A. and P. Hinchliffe, *Structure of the hydrophilic domain of respiratory complex I from Thermus thermophilus.* Science, 2006. **311**(5766): p. 1430-6.

20. Sazanov, L.A., *Respiratory complex I: mechanistic and structural insights provided by the crystal structure of the hydrophilic domain.* Biochemistry, 2007. **46**(9): p. 2275-88.
21. Hirst, J., *Towards the molecular mechanism of respiratory complex I.* Biochemical Journal, 2010. **425**: p. 327-339.
22. Iverson, T.M., *Catalytic mechanisms of complex II enzymes: A structural perspective.* Biochim Biophys Acta, 2013. **1827**(5): p. 648-57.
23. Crofts, A.R., et al., *Mechanism of ubiquinol oxidation by the bc(1) complex: Different domains of the quinol binding pocket and their role in the mechanism and binding of inhibitors.* Biochemistry, 1999. **38**(48): p. 15807-15826.
24. Crofts, A.R., *The cytochrome bc(1) complex: Function in the context of structure.* Annual Review of Physiology, 2004. **66**: p. 689-733.
25. Cooley, J.W., *A structural model for across membrane coupling between the Q(o) and Q(l) active sites of cytochrome bc(1).* Biochimica Et Biophysica Acta-Bioenergetics, 2010. **1797**(12): p. 1842-1848.
26. Swierczek, M., et al., *An Electronic Bus Bar Lies in the Core of Cytochrome bc(1).* Science, 2010. **329**(5990): p. 451-454.
27. Gorbikova, E.A., M. Wikstrom, and M.I. Verkhovsky, *The protonation state of the cross-linked tyrosine during the catalytic cycle of cytochrome c oxidase.* Journal of Biological Chemistry, 2008. **283**(50): p. 34907-12.
28. Gorbikova, E.A., et al., *The proton donor for O-O bond scission by cytochrome c oxidase.* Proceedings of the National Academy of Sciences of the United States of America, 2008. **105**(31): p. 10733-7.
29. Kaila, V.R.I., M.I. Verkhovsky, and M. Wikstrom, *Proton-Coupled Electron Transfer in Cytochrome Oxidase.* Chemical Reviews, 2010. **110**(12): p. 7062-7081.
30. James, W.O. and D.C. Elliott, *Cyanide-Resistant Mitochondria from the Spadix of an Arum.* Nature, 1955. **175**(4445): p. 89-89.
31. Millar, A.H. and D.A. Day, *Nitric oxide inhibits the cytochrome oxidase but not the alternative oxidase of plant mitochondria.* Febs Letters, 1996. **398**(2-3): p. 155-158.
32. Rich, P.R. and A.L. Moore, *The involvement of the protonmotive ubiquinone cycle in the respiratory chain of higher plants and its relation to the branchpoint of the alternate pathway.* Febs Letters, 1976. **65**(3): p. 339-44.
33. Storey, B.T., *Respiratory Chain of Plant Mitochondria: XVIII. Point of Interaction of the Alternate Oxidase with the Respiratory Chain.* Plant Physiology, 1976. **58**(4): p. 521-5.
34. Huq, S. and J.M. Palmer, *Superoxide and Hydrogen-Peroxide Production in Cyanide Resistant Arum-Maculatum Mitochondria.* Plant Science Letters, 1978. **11**(3-4): p. 351-358.
35. Moore, A.L., W.D. Bonner, and P.R. Rich, *Determination of Proton-Motive Force during Cyanide-Insensitive Respiration in Plant-Mitochondria.* Archives of Biochemistry and Biophysics, 1978. **186**(2): p. 298-306.
36. Douce, R., C.A. Mannella, and W.D. Bonner, Jr., *The external NADH dehydrogenases of intact plant mitochondria.* Biochim Biophys Acta, 1973. **292**(1): p. 105-16.
37. Eubel, H., L. Jansch, and H.P. Braun, *New insights into the respiratory chain of plant mitochondria. Supercomplexes and a unique composition of complex II.* Plant Physiology, 2003. **133**(1): p. 274-286.

38. Sunderhaus, S., et al., *Supramolecular structure of the OXPHOS system in highly thermogenic tissue of Arum maculatum.* Plant Physiology and Biochemistry, 2010. **48**(4): p. 265-272.
39. Kakizaki, Y., A.L. Moore, and K. Ito, *Different molecular bases underlie the mitochondrial respiratory activity in the homoeothermic spadices of Symplocarpus renifolius and the transiently thermogenic appendices of Arum maculatum.* Biochemical Journal, 2012. **445**: p. 237-246.
40. Vanlerberghe, G.C., *Alternative Oxidase: A Mitochondrial Respiratory Pathway to Maintain Metabolic and Signaling Homeostasis during Abiotic and Biotic Stress in Plants.* Int J Mol Sci, 2013. **14**(4): p. 6805-47.
41. Millar, A.H., et al., *Organization and Regulation of Mitochondrial Respiration in Plants.* Annual Review of Plant Biology, 2011. **62**: p. 79-104.
42. McDonald, A.E., S.M. Sieger, and G.C. Vanlerberghe, *Methods and approaches to study plant mitochondrial alternative oxidase.* Physiol Plant, 2002. **116**(2): p. 135-143.
43. Meeuse, B.J.D., *Thermogenic respiration in aroids.* Annu Rev Plant physio, 1975. **26**: p. 117-126.
44. Seymour, R.S., M. Gibernau, and K. Ito, *Thermogenesis and respiration of inflorescences of the dead horse arum Helicodiceros muscivorus, a pseudo-thermoregulatory aroid associated with fly pollination.* Functional Ecology, 2003. **17**(6): p. 886-894.
45. Seymour, R.S., *Scaling of heat production by thermogenic flowers: limits to floral size and maximum rate of respiration.* Plant Cell Environ, 2010. **33**(9): p. 1474-85.
46. Miller, R.E., et al., *In the heat of the night - alternative pathway respiration drives thermogenesis in Philodendron bipinnatifidum.* New Phytologist, 2011. **189**(4): p. 1013-1026.
47. Grant, N.M., et al., *Synchronicity of thermogenic activity, alternative pathway respiratory flux, AOX protein content, and carbohydrates in receptacle tissues of sacred lotus during floral development.* J Exp Bot, 2008. **59**(3): p. 705-14.
48. Affourtit, C., et al., *Functional expression of the plant alternative oxidase affects growth of the yeast Schizosaccharomyces pombe.* Journal of Biological Chemistry, 1999. **274**(10): p. 6212-6218.
49. Moore, A.L., et al., *Function of the alternative oxidase: is it still a scavenger?* Trends in Plant Science, 2002. **7**(11): p. 478-481.
50. Kaneko, I. and H. Ishii, *Effect of azoxystrobin on activities of antioxidant enzymes and alternative oxidase in wheat head blight pathogens Fusarium graminearum and Microdochium nivale.* Journal of General Plant Pathology, 2009. **75**(5): p. 388-398.
51. Hiser, C. and L. McIntosh, *Alternative Oxidase of Potato Is an Integral Membrane Protein Synthesized de Novo during Aging of Tuber Slices.* Plant Physiology, 1990. **93**(1): p. 312-8.
52. Murphy, M.P., *How mitochondria produce reactive oxygen species.* Biochemical Journal, 2009. **417**: p. 1-13.
53. Harman, D., *The biologic clock: the mitochondria?* J Am Geriatr Soc, 1972. **20**(4): p. 145-7.
54. Hirst, J., M.S. King, and K.R. Pryde, *The production of reactive oxygen species by complex I.* Biochemical Society Transactions, 2008. **36**: p. 976-980.

55. Adam-Vizi, V. and C. Chinopoulos, *Bioenergetics and the formation of mitochondrial reactive oxygen species.* Trends in Pharmacological Sciences, 2006. **27**(12): p. 639-645.
56. Kudin, A.P., et al., *Characterization of superoxide-producing sites in isolated brain mitochondria.* Journal of Biological Chemistry, 2004. **279**(6): p. 4127-4135.
57. Votyakova, T.V. and I.J. Reynolds, *Delta psi(m)-dependent and -independent production of reactive oxygen species by rat brain mitochondria.* Journal of Neurochemistry, 2001. **79**(2): p. 266-277.
58. Cadenas, E., et al., *Production of Superoxide Radicals and Hydrogen-Peroxide by Nadh-Ubiquinone Reductase and Ubiquinol-Cytochrome C Reductase from Beef-Heart Mitochondria.* Archives of Biochemistry and Biophysics, 1977. **180**(2): p. 248-257.
59. Maxwell, D.P., Y. Wang, and L. McIntosh, *The alternative oxidase lowers mitochondrial reactive oxygen production in plant cells.* Proceedings of the National Academy of Sciences of the United States of America, 1999. **96**(14): p. 8271-6.
60. Day, D.A., et al., *Regulation of Alternative Pathway Activity in Plant-Mitochondria - Deviations from Q-Pool Behavior during Oxidation of Nadh and Quinols.* Plant Physiology, 1991. **95**(3): p. 948-953.
61. Dry, I.B., et al., *Regulation of Alternative Pathway Activity in Plant-Mitochondria - Nonlinear Relationship between Electron Flux and the Redox Poise of the Quinone Pool.* Archives of Biochemistry and Biophysics, 1989. **273**(1): p. 148-157.
62. Raha, S. and B.H. Robinson, *Mitochondria, oxygen free radicals, disease and ageing.* Trends Biochem Sci, 2000. **25**(10): p. 502-8.
63. Gupta, K.J., A. Zabalza, and J.T. van Dongen, *Regulation of respiration when the oxygen availability changes.* Physiologia Plantarum, 2009. **137**(4): p. 383-391.
64. Ribas-Carbo, M., et al., *The Reaction of the Plant Mitochondrial Cyanide-Resistant Alternative Oxidase with Oxygen.* Biochimica Et Biophysica Acta-Bioenergetics, 1994. **1188**(3): p. 205-212.
65. Millar, A.H., F.J. Bergersen, and D.A. Day, *Oxygen-Affinity of Terminal Oxidases in Soybean Mitochondria.* Plant Physiology and Biochemistry, 1994. **32**(6): p. 847-852.
66. Weisiger, R.A. and I. Fridovich, *Superoxide dismutase. Organelle specificity.* Journal of Biological Chemistry, 1973. **248**(10): p. 3582-92.
67. Wagner, A.M. and A.L. Moore, *Structure and function of the plant alternative oxidase: Its putative role in the oxygen defence mechanism.* Bioscience Reports, 1997. **17**(3): p. 319-333.
68. Popov, V.N., et al., *Inhibition of the alternative oxidase stimulates H2O2 production in plant mitochondria.* Febs Letters, 1997. **415**(1): p. 87-90.
69. Millar, A.H., et al., *Organic acid activation of the alternative oxidase of plant mitochondria.* Febs Letters, 1993. **329**(3): p. 259-62.
70. Hoefnagel, M.H.N., et al., *Substrate kinetics of the plant mitochondrial alternative oxidase and the effects of pyruvate.* Plant Physiology, 1997. **115**(3): p. 1145-1153.
71. Feasey, N., Wansbrough-Jones,M., Mabey, D.C.W., Solomon A.W., *Neglected tropical diseases.* Br. Med. Bull., 2010. **93**: p. 179-200.

72. *Fact sheet N°259: Trypanosomiasis, Human African (sleeping sickness)*, in *WHO Media centre*. 2012.
73. Vickerman, K., *Developmental cycles and biology of pathogenic trypanosomes.* Br Med Bull, 1985. **41**(2): p. 105-14.
74. Nok, A.J., *Arsenicals (melarsoprol), pentamidine and suramin in the treatment of human African trypanosomiasis.* Parasitology Research, 2003. **90**(1): p. 71-9.
75. Barrett, M.P., *Problems for the chemotherapy of human African trypanosomiasis.* Curr Opin Infect Dis, 2000. **13**(6): p. 647-651.
76. Milord, F., et al., *Efficacy and toxicity of eflornithine for treatment of Trypanosoma brucei gambiense sleeping sickness.* Lancet, 1992. **340**(8820): p. 652-5.
77. Mccann, P.P. and A.E. Pegg, *Ornithine Decarboxylase as an Enzyme Target for Therapy.* Pharmacology & Therapeutics, 1992. **54**(2): p. 195-215.
78. Burri, C., et al., *Efficacy of new, concise schedule for melarsoprol in treatment of sleeping sickness caused by Trypanosoma brucei gambiense: a randomised trial.* Lancet, 2000. **355**(9213): p. 1419-25.
79. Priotto, G., et al., *Nifurtimox-eflornithine combination therapy for second-stage African Trypanosoma brucei gambiense trypanosomiasis: a multicentre, randomised, phase III, non-inferiority trial.* Lancet, 2009. **374**(9683): p. 56-64.
80. Grant, P.T., J.R. Sargent, and J.F. Ryley, *Respiratory systems in the Trypanosomidae.* Biochem J, 1961. **81**: p. 200-6.
81. Bienen, E.J., et al., *Non-cytochrome mediated mitochondrial ATP production in bloodstream form Trypanosoma brucei brucei.* Eur J Biochem, 1993. **216**(1): p. 75-80.
82. Clarkson, A.B., Jr., et al., *Respiration of bloodstream forms of the parasite Trypanosoma brucei brucei is dependent on a plant-like alternative oxidase.* Journal of Biological Chemistry, 1989. **264**(30): p. 17770-6.
83. Nihei, C., Y. Fukai, and K. Kita, *Trypanosome alternative oxidase as a target of chemotherapy.* Biochimica Et Biophysica Acta-Molecular Basis of Disease, 2002. **1587**(2-3): p. 234-239.
84. Berthold, D.A., *Isolation of mutants of the Arabidopsis thaliana alternative oxidase (ubiquinol : oxygen oxidoreductase) resistant to salicylhydroxamic acid.* Biochimica Et Biophysica Acta-Bioenergetics, 1998. **1364**(1): p. 73-83.
85. Kay, C.J. and J.M. Palmer, *Solubilization of the Alternative Oxidase of Cuckoo-Pint (Arum-Maculatum) Mitochondria - Stimulation by High-Concentrations of Ions and Effects of Specific Inhibitors.* Biochemical Journal, 1985. **228**(2): p. 309-318.
86. Schonbau.Gr, et al., *Specific Inhibition of Cyanide-Insensitive Respiratory Pathway in Plant Mitochondria by Hydroxamic Acids.* Plant Physiology, 1971. **47**(1): p. 124-&.
87. Rich, P.R., et al., *Studies on Mechanism of Inhibition of Redox Enzymes by Substituted Hydroxamic Acids.* Biochimica Et Biophysica Acta, 1978. **525**(2): p. 325-337.
88. Opperdoes, F.R., et al., *Trypanosoma brucei: an evaluation of salicylhydroxamic acid as a trypanocidal drug.* Exp Parasitol, 1976. **40**(2): p. 198-205.

89. Vandermeer, C., et al., *Pitfalls of Salicylhydroxamic Acid Plus Glycerol Treatment of T-Vivax Infected Goats.* Tropenmedizin Und Parasitologie, 1980. **31**(3): p. 275-282.
90. Evans, D.A., C.J. Brightman, and M.F. Holland, *Salicylhydroxamic-acid/glycerol in experimental trypanosomiasis.* Lancet, 1977. **2**(8041): p. 769.
91. Van Der Meer, C. and J.A. Versluijs-Broers, *Trypanosoma brucei: trypanocidal effect of salicylhydroxamic acid plus glycerol in infected rats.* Exp Parasitol, 1979. **48**(1): p. 126-34.
92. Clarkson, A.B., et al., *Trypanosoma-Brucei-Brucei - a Systematic Screening for Alternatives to the Salicylhydroxamic Acid Glycerol Combination.* Molecular and Biochemical Parasitology, 1981. **3**(5): p. 271-291.
93. Grady, R.W., E.J. Bienen, and A.B. Clarkson, *P-Alkyloxybenzhydroxamic Acids, Effective Inhibitors of the Trypanosome Glycerol-3-Phosphate Oxidase.* Molecular and Biochemical Parasitology, 1986. **19**(3): p. 231-240.
94. Grady, R.W., E.J. Bienen, and A.B. Clarkson, Jr., *Esters of 3,4-dihydroxybenzoic acid, highly effective inhibitors of the sn-glycerol-3-phosphate oxidase of Trypanosoma brucei brucei.* Molecular and Biochemical Parasitology, 1986. **21**(1): p. 55-63.
95. Grady, R.W., et al., *N-n-alkyl-3,4-dihydroxybenzamides as inhibitors of the trypanosome alternative oxidase: activity in vitro and in vivo.* Antimicrob Agents Chemother, 1993. **37**(5): p. 1082-5.
96. Pollakis, G., et al., *Competition between Inhibitors of the Trypanosome Alternative Oxidase (Tao) and Reduced Coenzyme Q(9).* Biochemical Pharmacology, 1995. **50**(8): p. 1207-1210.
97. Ott, R., et al., *Novel inhibitors of the trypanosome alternative oxidase inhibit Trypanosoma brucei brucei growth and respiration.* Acta Tropica, 2006. **100**(3): p. 172-184.
98. Janes, H.W. and S.C. Wiest, *Inhibition of O2 Consumption Resistant to Cyanide and Its Development by N-Propyl Gallate and Salicylhydroxamic Acid.* Plant Physiology, 1982. **70**(3): p. 853-857.
99. Siedow, J.N. and D.M. Bickett, *Structural features required for inhibition of cyanide-insensitive electron transfer by propyl gallate.* Arch Biochem Biophys, 1981. **207**(1): p. 32-9.
100. Sasaki, H., et al., *Ascofuranone, a New Antibiotic from Ascochyta-Viciae.* Tetrahedron Letters, 1972(25): p. 2541-&.
101. Sasaki, H., et al., *Isolation and Structure of Ascofuranone and Ascofranol, Antibiotics with Hypolipidemic Activity.* Journal of Antibiotics, 1973. **26**(11): p. 676-680.
102. Sawada, M., et al., *Hypolipidemic Property of Ascofuranone.* Journal of Antibiotics, 1973. **26**(11): p. 681-686.
103. Hosokawa, T., et al., *Alteration of Cholesterol-Metabolism by 4-0-Methylascochlorin in Rats.* Lipids, 1981. **16**(6): p. 433-438.
104. Magae, J., et al., *Antitumor protective property of an isoprenoid antibiotic, ascofuranone.* J Antibiot (Tokyo), 1982. **35**(11): p. 1547-52.
105. Magae, J., et al., *Antitumor and Antimetastatic Activity of an Antibiotic, Ascofuranone, and Activation of Phagocytes.* Journal of Antibiotics, 1988. **41**(7): p. 959-965.

106. Hosokawa, T., K. Ando, and G. Tamura, *An Ascochlorin Derivative, as-6, Reduces Insulin Resistance in the Genetically-Obese Diabetic Mouse, Db Db.* Diabetes, 1985. **34**(3): p. 267-274.
107. Hosokawa, T., K. Ando, and G. Tamura, *Structural and Functional Abnormalities in the Adipocyte Plasma-Membrane from Db/Db Mouse, and the Effect on the Abnormalities of Oral Treatment with as-6.* Biochemical and Biophysical Research Communications, 1984. **125**(1): p. 64-69.
108. Coleman, J.J., et al., *Antifungal Activity of Microbial Secondary Metabolites.* Plos One, 2011. **6**(9).
109. Kawaguchi, M., et al., *A new ascochlorin derivative from Cylindrocarpon sp. FKI-4602.* J Antibiot (Tokyo), 2013. **66**(1): p. 23-9.
110. Minagawa, N., et al., *An antibiotic, ascofuranone, specifically inhibits respiration and in vitro growth of long slender bloodstream forms of Trypanosoma brucei brucei.* Molecular and Biochemical Parasitology, 1996. **81**(2): p. 127-136.
111. Yabu, Y., et al., *Chemotherapeutic efficacy of ascofuranone in Trypanosoma vivax-infected mice without glycerol.* Parasitology International, 2006. **55**(1): p. 39-43.
112. Yabu, Y., *Oral and intraperitoneal treatment of Trypanosoma brucei brucei with a combination of ascofuranone and glyercol in mice.* Parasitology International, 1998. **47**: p. 131-137.
113. Berry, E.A., et al., *Ascochlorin is a novel, specific inhibitor of the mitochondrial cytochrome bc1 complex.* Biochim Biophys Acta, 2010. **1797**(3): p. 360-70.
114. Mogi, T., et al., *Antibiotics LL-Z1272 identified as novel inhibitors discriminating bacterial and mitochondrial quinol oxidases.* Biochim Biophys Acta, 2009. **1787**(2): p. 129-33.
115. Saimoto, H., et al., *Pharmacophore identification of ascofuranone, potent inhibitor of cyanide-insensitive alternative oxidase of Trypanosoma brucei.* Journal of Biochemistry, 2013. **153**(3): p. 267-273.
116. Joullie, M., *A simple total synthesis of (+-)-ascofuranone.* Tetrahedron Letters, 1984. **25**(35): p. 3795-3796.
117. Guthrie, A.E., J.E. Semple, and M.M. Joullie, *Synthetic Studies of Fungal Metabolites - Ascofuranone and Colletochlorin-D.* Journal of Organic Chemistry, 1982. **47**(12): p. 2369-2376.
118. Mori, K. and T. Fujioka, *Synthetic Microbial Chemistry .4. Synthesis of (+/-)-Ascochlorin, (+/-)-Ascofuranone and Ll-Z1272-Alpha.* Tetrahedron, 1984. **40**(14): p. 2711-2720.
119. Mori, K. and S. Takechi, *Synthetic Microbial Chemistry .10. Synthesis of the Natural Enantiomers of Ascochlorin, Ascofuranone and Ascofuranol.* Tetrahedron, 1985. **41**(15): p. 3049-3062.
120. Saimoto, H., Y. Kusano, and T. Hiyama, *A Mild Procedure for Hydrolysis of Alkoxymethyl Aryl Ethers to Give Hydroxyarenes - a Rational Synthesis of Ascofuranone.* Tetrahedron Letters, 1986. **27**(14): p. 1607-1610.
121. Saimoto, H. and T. Hiyama, *A General Highly Efficient Access to Prenylated Phenolic Natural-Products - Synthesis of Colletochlorin-B and Colletochlorin-D.* Tetrahedron Letters, 1986. **27**(5): p. 597-600.
122. Saimoto, H., et al., *A General-Approach for the Synthesis of Phenolic Natural-Products - Facile Syntheses of Grifolin and Colletochlorin-B and*

Colletochlorin-D. Bulletin of the Chemical Society of Japan, 1994. **67**(4): p. 1178-1185.
123. Ziogas, B.N., B.C. Baldwin, and J.E. Young, *Alternative respiration: A biochemical mechanism of resistance to azoxystrobin (ICIA 5504) in Septoria tritici.* Pesticide Science, 1997. **50**(1): p. 28-34.
124. Clough, J.M., *The Strobilurins, Oudemansins, and Myxothiazols, Fungicidal Derivatives of Beta-Methoxyacrylic Acid.* Natural Product Reports, 1993. **10**(6): p. 565-574.
125. Huh, W.K. and S.O. Kang, *Characterization of the gene family encoding alternative oxidase from Candida albicans.* Biochemical Journal, 2001. **356**: p. 595-604.
126. Minagawa, N. and A. Yoshimoto, *The induction of cyanide-resistant respiration in Hansenula anomala.* J Biochem, 1987. **101**(5): p. 1141-6.
127. Lambowit.Am and C.W. Slayman, *Cyanide-Resistant Respiration in Neurospora-Crassa.* Journal of Bacteriology, 1971. **108**(3): p. 1087-&.
128. Murphy, A.D. and N. Lang-Unnasch, *Alternative oxidase inhibitors potentiate the activity of atovaquone against Plasmodium falciparum.* Antimicrobial Agents and Chemotherapy, 1999. **43**(3): p. 651-654.
129. Avila-Adame, C. and W. Koller, *Disruption of the alternative oxidase gene in Magnaporthe grisea and its impact on host infection.* Molecular Plant-Microbe Interactions, 2002. **15**(5): p. 493-500.
130. Wood, P.M. and D.W. Hollomon, *A critical evaluation of the role of alternative oxidase in the performance of strobilurin and related fungicides acting at the Q(o) site of Complex III.* Pest Management Science, 2003. **59**(5): p. 499-511.
131. Vincelli, P. and E. Dixon, *Resistance to Q(o)I (strobilurin-like) fungicides in isolates of Pyricularia grisea from perennial ryegrass.* Plant Disease, 2002. **86**(3): p. 235-240.
132. Fisher, N., et al., *Modeling the Qo site of crop pathogens in Saccharomyces cerevisiae cytochrome b.* Eur J Biochem, 2004. **271**(11): p. 2264-71.
133. Chin, K.M., et al., *Characterizing resistance risk of Erysiphe graminis f.sp tritici to strobilurins.* Crop Protection, 2001. **20**(2): p. 87-96.
134. Moore, A.L., A.L. Umbach, and J.N. Siedow, *Structure-Function-Relationships of the Alternative Oxidase of Plant-Mitochondria - a Model of the Active-Site.* Journal of Bioenergetics and Biomembranes, 1995. **27**(4): p. 367-377.
135. Siedow, J.N., A.L. Umbach, and A.L. Moore, *The Active-Site of the Cyanide-Resistant Oxidase from Plant-Mitochondria Contains a Binuclear Iron Center.* Febs Letters, 1995. **362**(1): p. 10-14.
136. Andersson, M.E. and P. Nordlund, *A revised model of the active site of alternative oxidase.* Febs Letters, 1999. **449**(1): p. 17-22.
137. Berthold, D.A., M.E. Andersson, and P. Nordlund, *New insight into the structure and function of the alternative oxidase.* Biochimica Et Biophysica Acta-Bioenergetics, 2000. **1460**(2-3): p. 241-254.
138. Albury, M.S., et al., *Structure of the plant alternative oxidase. Site-directed mutagenesis provides new information on the active site and membrane topology.* Journal of Biological Chemistry, 2002. **277**(2): p. 1190-4.
139. Berthold, D.A., et al., *EPR studies of the mitochondrial alternative oxidase. Evidence for a diiron carboxylate center.* Journal of Biological Chemistry, 2002. **277**(46): p. 43608-14.

140. Ajayi, W.U., M. Chaudhuri, and G.C. Hill, *Site-directed mutagenesis reveals the essentiality of the conserved residues in the putative diiron active site of the trypanosome alternative oxidase.* Journal of Biological Chemistry, 2002. **277**(10): p. 8187-93.
141. Nakamura, K., et al., *Mutational analysis of the Trypanosoma vivax alternative oxidase: The E(X)(6)Y Motif is conserved in both mitochondrial alternative oxidase and plastid terminal oxidase and is indispensable for enzyme activity.* Biochemical and Biophysical Research Communications, 2005. **334**(2): p. 593-600.
142. Moore, A.L., et al., *Compelling EPR evidence that the alternative oxidase is a diiron carboxylate protein.* Biochimica Et Biophysica Acta-Bioenergetics, 2008. **1777**(4): p. 327-330.
143. Solomon, E.I., et al., *Geometric and electronic structure/function correlations in non-heme iron enzymes.* Chemical Reviews, 2000. **100**(1): p. 235-349.
144. McDonald, A.E., *Alternative oxidase: what information can protein sequence comparisons give us?* Physiol Plant, 2009. **137**(4): p. 328-41.
145. Albury, M.S., C. Elliott, and A.L. Moore, *Ubiquinol-binding site in the alternative oxidase Mutagenesis reveals features important for substrate binding and inhibition.* Biochimica Et Biophysica Acta-Bioenergetics, 2010. **1797**(12): p. 1933-1939.
146. Fisher, N. and P.R. Rich, *A motif for quinone binding sites in respiratory and photosynthetic systems.* J Mol Biol, 2000. **296**(4): p. 1153-62.
147. Rhoads, D.M., et al., *Regulation of the cyanide-resistant alternative oxidase of plant mitochondria. Identification of the cysteine residue involved in alpha-keto acid stimulation and intersubunit disulfide bond formation.* Journal of Biological Chemistry, 1998. **273**(46): p. 30750-6.
148. Umbach, A.L. and J.N. Siedow, *Covalent and Noncovalent Dimers of the Cyanide-Resistant Alternative Oxidase Protein in Higher Plant Mitochondria and Their Relationship to Enzyme Activity.* Plant Physiology, 1993. **103**(3): p. 845-854.
149. Vanlerberghe, G.C., et al., *Alternative Oxidase Activity in Tobacco Leaf Mitochondria (Dependence on Tricarboxylic Acid Cycle-Mediated Redox Regulation and Pyruvate Activation).* Plant Physiology, 1995. **109**(2): p. 353-361.
150. Gelhaye, E., et al., *A specific form of thioredoxin h occurs in plant mitochondria and regulates the alternative oxidase.* Proceedings of the National Academy of Sciences of the United States of America, 2004. **101**(40): p. 14545-50.
151. Umbach, A.L. and J.N. Siedow, *The reaction of the soybean cotyledon mitochondrial cyanide-resistant oxidase with sulfhydryl reagents suggests that alpha-keto acid activation involves the formation of a thiohemiacetal.* Journal of Biological Chemistry, 1996. **271**(40): p. 25019-26.
152. Umbach, A.L., et al., *Activation of the plant mitochondrial alternative oxidase: insights from site-directed mutagenesis.* Biochim Biophys Acta, 2002. **1554**(1-2): p. 118-28.
153. Djajanegara, I., et al., *A single amino acid change in the plant alternative oxidase alters the specificity of organic acid activation.* Febs Letters, 1999. **454**(3): p. 220-4.

154. Carre, J.E., C. Affourtit, and A.L. Moore, *Interaction of purified alternative oxidase from thermogenic Arum maculatum with pyruvate.* Febs Letters, 2011. **585**(2): p. 397-401.
155. Holtzapffel, R.C., et al., *A tomato alternative oxidase protein with altered regulatory properties.* Biochim Biophys Acta, 2003. **1606**(1-3): p. 153-62.
156. Vanlerberghe, G.C., L. McIntosh, and J.Y. Yip, *Molecular localization of a redox-modulated process regulating plant mitochondrial electron transport.* Plant Cell, 1998. **10**(9): p. 1551-60.
157. Crichton, P.G., et al., *Constitutive activity of Sauromatum guttatum alternative oxidase in Schizosaccharomyces pombe implicates residues in addition to conserved cysteines in alpha-keto acid activation.* Febs Letters, 2005. **579**(2): p. 331-336.
158. Ito, K., et al., *Identification of a gene for pyruvate-insensitive mitochondrial alternative oxidase expressed in the thermogenic appendices in Arum maculatum.* Plant Physiology, 2011. **157**(4): p. 1721-32.
159. Umbach, A.L. and J.N. Siedow, *The cyanide-resistant alternative oxidases from the fungi Pichia stipitis and Neurospora crassa are monomeric and lack regulatory features of the plant enzyme.* Arch Biochem Biophys, 2000. **378**(2): p. 234-45.
160. Fukai, Y., et al., *Overproduction of highly active trypanosome alternative oxidase in Escherichia coli heme-deficient mutant.* Parasitology International, 2003. **52**(3): p. 237-41.
161. Elliott, C., *The overexpression, purification and crystalisation of the Alternative oxidase*. 2013, University of Sussex.
162. Mandel, M. and A. Higa, *Calcium-Dependent Bacteriophage DNA Infection.* Journal of Molecular Biology, 1970. **53**(1): p. 159-&.
163. Kido, Y., et al., *Purification and kinetic characterization of recombinant alternative oxidase from Trypanosoma brucei brucei.* Biochim Biophys Acta, 2010. **1797**(4): p. 443-50.
164. Elthon, T.E., R.L. Nickels, and L. McIntosh, *Monoclonal antibodies to the alternative oxidase of higher plant mitochondria.* Plant Physiology, 1989. **89**(4): p. 1311-7.
165. Whittington, D.A. and S.J. Lippard, *Crystal structures of the soluble methane monooxygenase hydroxylase from Methylococcus capsulatus (Bath) demonstrating geometrical variability at the dinuclear iron active site.* J Am Chem Soc, 2001. **123**(5): p. 827-38.
166. Rosenzweig, A.C., et al., *Crystal structures of the methane monooxygenase hydroxylase from Methylococcus capsulatus (Bath): implications for substrate gating and component interactions.* Proteins, 1997. **29**(2): p. 141-52.
167. Voegtli, W.C., et al., *Variable coordination geometries at the diiron(II) active site of ribonucleotide reductase R2.* J Am Chem Soc, 2003. **125**(51): p. 15822-30.
168. Nordlund, P. and H. Eklund, *Structure and function of the Escherichia coli ribonucleotide reductase protein R2.* J Mol Biol, 1993. **232**(1): p. 123-64.
169. Voegtli, W.C., et al., *Crystal structure of the ribonucleotide reductase R2 mutant that accumulates a mu-1,2-peroxodiiron(III) intermediate during oxygen activation.* Journal of the American Chemical Society, 2000. **122**(14): p. 3255-3261.

170. Esser, L., et al., *Crystallographic studies of quinol oxidation site inhibitors: A modified classification of inhibitors for the cytochrome bc(1) complex.* Journal of Molecular Biology, 2004. **341**(1): p. 281-302.
171. Jin, S., et al., *X-ray crystal structures of reduced rubrerythrin and its azide adduct: a structure-based mechanism for a non-heme diiron peroxidase.* J Am Chem Soc, 2002. **124**(33): p. 9845-55.
172. Chovancova, E., et al., *CAVER 3.0: a tool for the analysis of transport pathways in dynamic protein structures.* PLoS Comput Biol, 2012. **8**(10): p. e1002708.
173. Sakamoto, K., et al., *Probing substrate binding site of the Escherichia coli quinol oxidases using synthetic ubiquinol analogues.* Journal of Biological Chemistry, 1996. **271**(47): p. 29897-902.
174. Li, H., A.D. Robertson, and J.H. Jensen, *Very fast empirical prediction and rationalization of protein pKa values.* Proteins, 2005. **61**(4): p. 704-21.
175. Crichton, P.G., et al., *Mutagenesis of the Sauromatum guttatum alternative oxidase reveals features important for oxygen binding and catalysis.* Biochim Biophys Acta, 2010. **1797**(6-7): p. 732-7.
176. Kita, K., K. Konishi, and Y. Anraku, *Terminal oxidases of Escherichia coli aerobic respiratory chain. I. Purification and properties of cytochrome b562-o complex from cells in the early exponential phase of aerobic growth.* Journal of Biological Chemistry, 1984. **259**(5): p. 3368-74.
177. Reid, G.A. and W.J. Ingledew, *Characterization and phenotypic control of the cytochrome content of Escherichia coli.* Biochem J, 1979. **182**(2): p. 465-72.
178. Suzuki, T., et al., *Molecular cloning and characterization of Trypanosoma vivax alternative oxidase (AOX) gene, a target of the trypanocide ascofuranone.* Parasitology International, 2004. **53**(3): p. 235-45.
179. Bekker, M., et al., *Changes in the redox state and composition of the quinone pool of Escherichia coli during aerobic batch-culture growth.* Microbiology, 2007. **153**(Pt 6): p. 1974-80.
180. Chaudhuri, M., et al., *The trypanosome alternative oxidase exists as a monomer in Trypanosoma brucei mitochondria.* Parasitology Research, 2005. **96**(3): p. 178-83.
181. Millar, A.H., et al., *Expression and kinetics of the mitochondrial alternative oxidase in nitrogen-fixing nodules of soybean roots.* Plant Cell and Environment, 1997. **20**(10): p. 1273-1282.
182. Chaudhuri, M., R. Sharan, and G.C. Hill, *Trypanosome alternative oxidase is regulated post-transcriptionally at the level of RNA stability.* J Eukaryot Microbiol, 2002. **49**(4): p. 263-9.
183. Helfert, S., et al., *Roles of triosephosphate isomerase and aerobic metabolism in Trypanosoma brucei.* Biochem J, 2001. **357**(Pt 1): p. 117-25.
184. Adams, R. and I. Levine, *Simplification of the Gattermann synthesis of hydroxy aldehydes.* Journal of the American Chemical Society, 1923. **45**: p. 2373-2377.
185. Cottingham, I.R. and A.L. Moore, *Ubiquinone Pool Behavior in Plant-Mitochondria.* Biochimica Et Biophysica Acta, 1983. **724**(2): p. 191-200.
186. Berthold, D.A., *Isolation of mutants of the Arabidopsis thaliana alternative oxidase (ubiquinol:oxygen oxidoreductase) resistant to salicylhydroxamic acid.* Biochim Biophys Acta, 1998. **1364**(1): p. 73-83.

187. Kawashima, H., et al., *Inhibitory effects of alkyl gallate and its derivatives on fatty acid desaturation.* Biochimica Et Biophysica Acta-Lipids and Lipid Metabolism, 1996. **1299**(1): p. 34-38.
188. Jacobs, R.T., et al., *SCYX-7158, an orally-active benzoxaborole for the treatment of stage 2 human African trypanosomiasis.* PLoS Negl Trop Dis, 2011. **5**(6): p. e1151.
189. Atkins, P.W. and J. De Paula, *Physical chemistry for the life sciences*. 2006, Oxford: Oxford University Press.
190. Godwin, J.R., et al., *Icia5504 - a Novel, Broad-Spectrum, Systemic Beta-Methoxyacrylate Fungicide.* Brighton Crop Protection Conference : Pests and Diseases - 1992, Vols 1-3, 1992: p. 435-442.
191. Fisher, N. and B. Meunier, *Re-examination of inhibitor resistance conferred by Q(o)-site mutations in cytochrome b using yeast as a model system.* Pest Management Science, 2005. **61**(10): p. 973-978.
192. Vallieres, C., et al., *HDQ, a Potent Inhibitor of Plasmodium falciparum Proliferation, Binds to the Quinone Reduction Site of the Cytochrome bc(1) Complex.* Antimicrobial Agents and Chemotherapy, 2012. **56**(7): p. 3739-3747.
193. Seeliger, D. and B.L. de Groot, *Ligand docking and binding site analysis with PyMOL and Autodock/Vina.* Journal of Computer-Aided Molecular Design, 2010. **24**(5): p. 417-422.
194. Valentine, A.M., S.S. Stahl, and S.J. Lippard, *Mechanistic studies of the reaction of reduced methane monooxygenase hydroxylase with dioxygen and substrates.* Journal of the American Chemical Society, 1999. **121**(16): p. 3876-3887.
195. Rosenzweig, A.C., et al., *Crystal-Structure of a Bacterial Nonheme Iron Hydroxylase That Catalyzes the Biological Oxidation of Methane.* Nature, 1993. **366**(6455): p. 537-543.
196. Lee, S.J., et al., *Control of substrate access to the active site in methane monooxygenase.* Nature, 2013. **494**(7437): p. 380-384.
197. Reichard, P., *From Rna to DNA, Why So Many Ribonucleotide Reductases.* Science, 1993. **260**(5115): p. 1773-1777.
198. Tomter, A.B., et al., *Ribonucleotide reductase class I with different radical generating clusters.* Coordination Chemistry Reviews, 2013. **257**(1): p. 3-26.
199. Stubbe, J., et al., *Radical initiation in the class I ribonucleotide reductase: long-range proton-coupled electron transfer?* Chemical Reviews, 2003. **103**(6): p. 2167-201.
200. Coulter, E.D., et al., *Rubrerythrin-catalyzed substrate oxidation by dioxygen and hydrogen peroxide.* Inorganica Chimica Acta, 2000. **297**(1-2): p. 231-241.
201. Sztukowska, M., et al., *Role of rubrerythrin in the oxidative stress response of Porphyromonas gingivalis.* Molecular Microbiology, 2002. **44**(2): p. 479-488.
202. May, A., et al., *A rubrerythrin-like oxidative stress protein of Clostridium acetobutylicum is encoded by a duplicated gene and identical to the heat shock protein Hsp21.* Fems Microbiology Letters, 2004. **238**(1): p. 249-254.
203. Riebe, O., et al., *Pathway for H2O2 and O-2 detoxification in Clostridium acetobutylicum.* Microbiology-Sgm, 2009. **155**: p. 16-24.

204. Chang, M.C., et al., *Turning on ribonucleotide reductase by light-initiated amino acid radical generation.* Proceedings of the National Academy of Sciences of the United States of America, 2004. **101**(18): p. 6882-7.
205. Saleh, L. and J.M. Bollinger, Jr., *Cation mediation of radical transfer between Trp48 and Tyr356 during O2 activation by protein R2 of Escherichia coli ribonucleotide reductase: relevance to R1-R2 radical transfer in nucleotide reduction?* Biochemistry, 2006. **45**(29): p. 8823-30.
206. Tinberg, C.E. and S.J. Lippard, *Dioxygen Activation in Soluble Methane Monooxygenase.* Accounts of Chemical Research, 2011. **44**(4): p. 280-288.
207. Gherman, B.F., et al., *Dioxygen activation in methane monooxygenase: A theoretical study.* Journal of the American Chemical Society, 2004. **126**(9): p. 2978-2990.
208. Shu, L., et al., *An Fe2IVO2 diamond core structure for the key intermediate Q of methane monooxygenase.* Science, 1997. **275**(5299): p. 515-8.
209. Tinberg, C.E. and S.J. Lippard, *Revisiting the Mechanism of Dioxygen Activation in Soluble Methane Monooxygenase from M. capsulatus (Bath): Evidence for a Multi-Step, Proton-Dependent Reaction Pathway.* Biochemistry, 2009. **48**(51): p. 12145-12158.
210. Bochevarov, A.D., et al., *Insights into the Different Dioxygen Activation Pathways of Methane and Toluene Monooxygenase Hydroxylases.* Journal of the American Chemical Society, 2011. **133**(19): p. 7384-7397.
211. Ambundo, E.A., R.A. Friesner, and S.J. Lippard, *Reactions of methane monooxygenase intermediate Q with derivatized methanes.* Journal of the American Chemical Society, 2002. **124**(30): p. 8770-8771.
212. Kolberg, M., et al., *Structure, function, and mechanism of ribonucleotide reductases.* Biochimica Et Biophysica Acta-Proteins and Proteomics, 2004. **1699**(1-2): p. 1-34.
213. Bollinger, J.M., et al., *Engineering the diiron site of Escherichia coli ribonucleotide reductase protein R2 to accumulate an intermediate similar to H-peroxo, the putative peroxodiiron(III) complex from the methane monooxygenase catalytic cycle.* Journal of the American Chemical Society, 1998. **120**(5): p. 1094-1095.
214. Baldwin, J., et al., *Rational reprogramming of the R2 subunit of Escherichia coli ribonucleotide reductase into a self-hydroxylating monooxygenase.* J Am Chem Soc, 2001. **123**(29): p. 7017-30.
215. Baldwin, J., et al., *Mechanism of rapid electron transfer during oxygen activation in the R2 subunit of Escherichia coli ribonucleotide reductase. 1. Evidence for a transient tryptophan radical.* Journal of the American Chemical Society, 2000. **122**(49): p. 12195-12206.
216. Avval, F.Z. and A. Holmgren, *Molecular Mechanisms of Thioredoxin and Glutaredoxin as Hydrogen Donors for Mammalian S Phase Ribonucleotide Reductase.* Journal of Biological Chemistry, 2009. **284**(13): p. 8233-8240.
217. Aberg, A., et al., *Autocatalytic Generation of Dopa in the Engineered Protein-R2 F208y from Escherichia-Coli Ribonucleotide Reductase and Crystal-Structure of the Dopa-208 Protein.* Biochemistry, 1993. **32**(37): p. 9845-9850.
218. Dillard, B.D., et al., *A cryo-crystallographic time course for peroxide reduction by rubrerythrin from Pyrococcus furiosus.* Journal of Biological Inorganic Chemistry, 2011. **16**(6): p. 949-959.

219. Marechal, A., et al., *Three Redox States of Trypanosoma brucei Alternative Oxidase Identified by Infrared Spectroscopy and Electrochemistry.* Journal of Biological Chemistry, 2009. **284**(46): p. 31827-31833.
220. Atta, M., et al., *Epr Studies of Mixed-Valent [(Fefeiii)-Fe-Ii] Clusters Formed in the R2 Subunit of Ribonucleotide Reductase from Mouse or Herpes-Simplex Virus - Mild Chemical-Reduction of the Diferric Centers.* Journal of the American Chemical Society, 1994. **116**(14): p. 6429-6430.
221. Hendrich, M.P., et al., *Integer-Spin Epr Studies of the Fully Reduced Methane Monooxygenase Hydroxylase Component.* Journal of the American Chemical Society, 1990. **112**(15): p. 5861-5865.
222. Kovaleva, E.G. and J.D. Lipscomb, *Crystal structures of Fe2+ dioxygenase superoxo, alkylperoxo, and bound product intermediates.* Science, 2007. **316**(5823): p. 453-457.
223. Cho, K.B., et al., *Nonheme iron-oxo and -superoxo reactivities: O2 binding and spin inversion probability matter.* Chem Commun (Camb), 2012. **48**(16): p. 2189-91.
224. Atkin, C.L., et al., *Iron and Free-Radical in Ribonucleotide Reductase - Exchange of Iron and Mossbauer-Spectroscopy of Protein-B2 Subunit of Escherichia-Coli Enzyme.* Journal of Biological Chemistry, 1973. **248**(21): p. 7464-7472.
225. Shan, X. and L. Que, Jr., *Intermediates in the oxygenation of a nonheme diiron(II) complex, including the first evidence for a bound superoxo species.* Proceedings of the National Academy of Sciences of the United States of America, 2005. **102**(15): p. 5340-5.
226. Holmes, M.A., et al., *Structures of deoxy and oxy hemerythrin at 2.0 A resolution.* J Mol Biol, 1991. **218**(3): p. 583-93.
227. Kodera, M., et al., *Reversible O-O Bond Scission of Peroxodiiron(III) to High-Spin Oxodiiron(IV) in Dioxygen Activation of a Diiron Center with a Bis-tpa Dinucleating Ligand as a Soluble Methane Monooxygenase Model.* Journal of the American Chemical Society, 2012. **134**(32): p. 13236-13239.
228. Postila, P.A., et al., *Key role of water in proton transfer at the Qo-site of the cytochrome bc1 complex predicted by atomistic molecular dynamics simulations.* Biochim Biophys Acta, 2013. **1827**(6): p. 761-8.
229. Tommos, C., et al., *De novo proteins as models of radical enzymes.* Biochemistry, 1999. **38**(29): p. 9495-507.
230. Young, L., et al., *Probing the ubiquinol-binding site of recombinant Sauromatum guttatum alternative oxidase expressed in E. coli membranes through site-directed mutagenesis.* Biochim Biophys Acta, 2014.

9 Appendix I

^{1}H and ^{13}C NMR for synthesised compounds. Assignments can be found in Chapter 2.

2,4-dihydroxy-5-methyl-benzaldehyde (1)

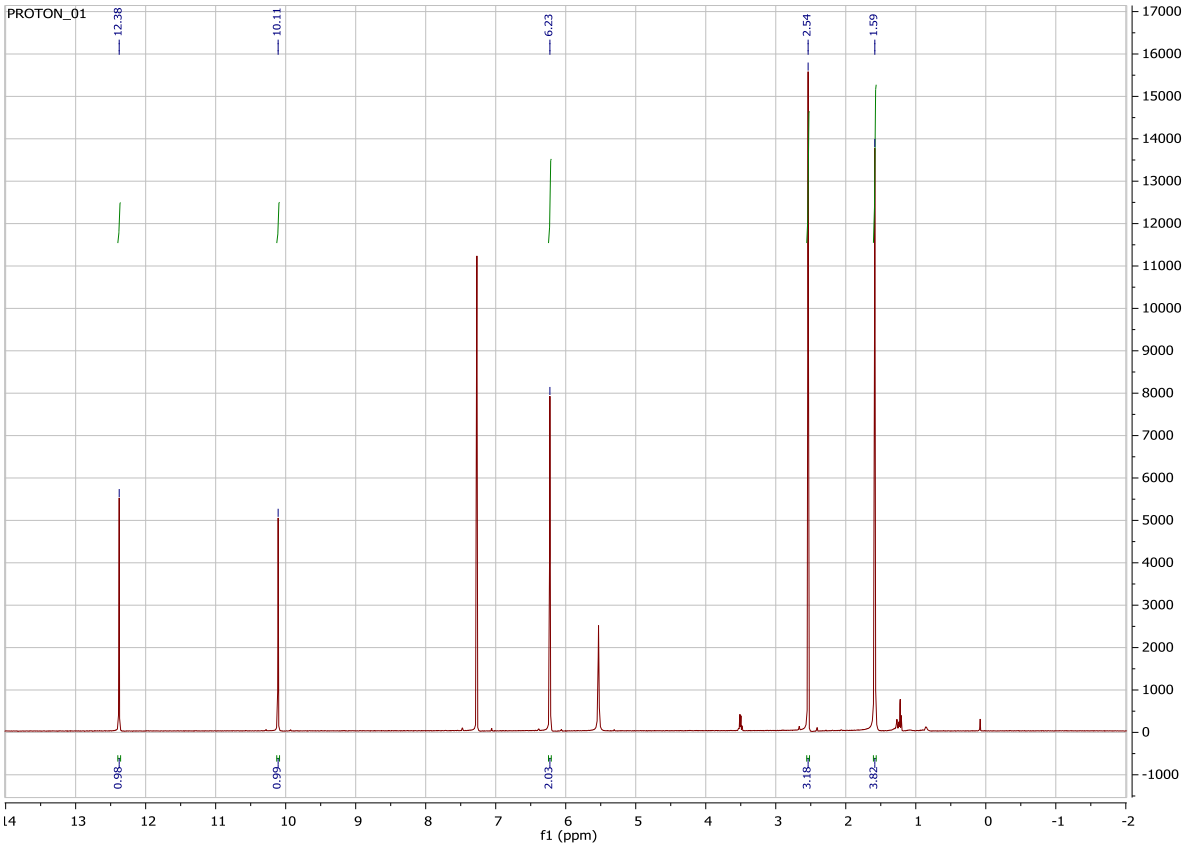

3-chloro-4,6-dihydroxy-2-methyl-benzaldehyde (2)

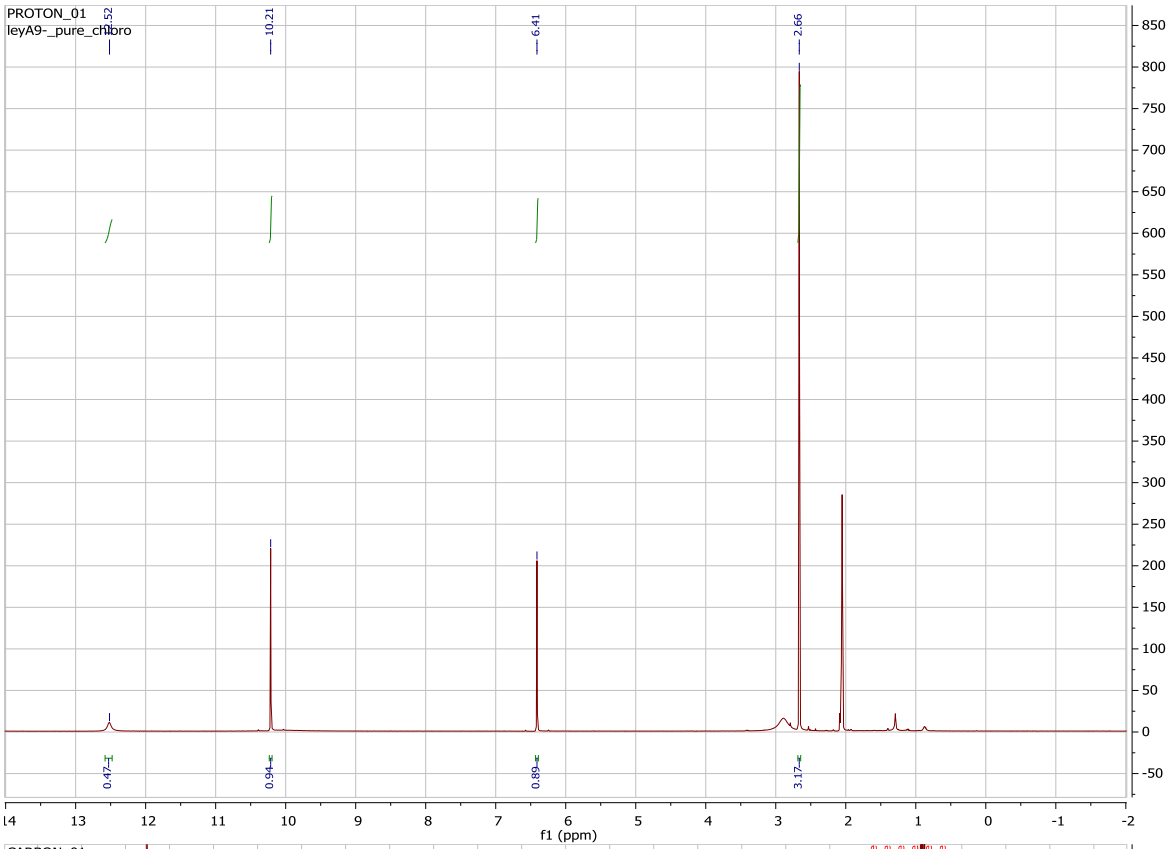

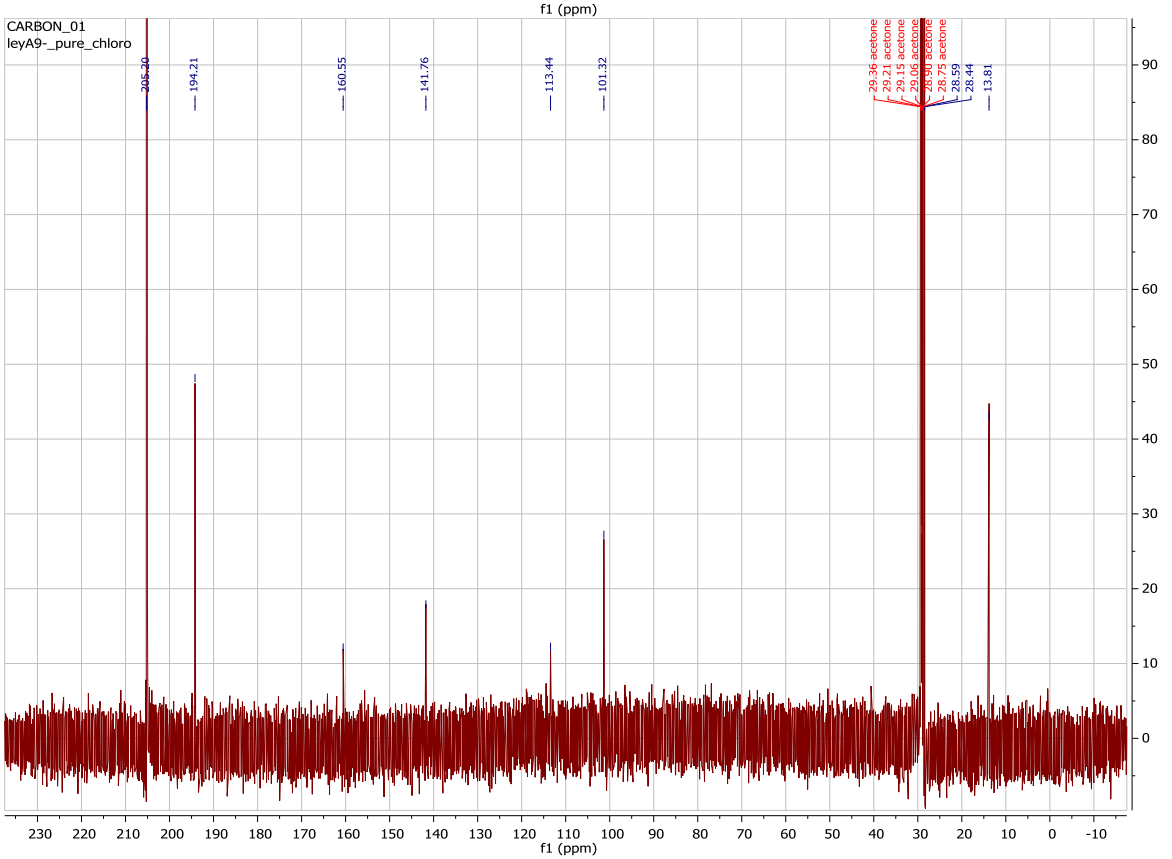

(E)-3-chloro-5-(3,7-dimethylocta-2,6-dienyl)-4,6-dihydroxy-2-ethylbenzaldehyde (4)

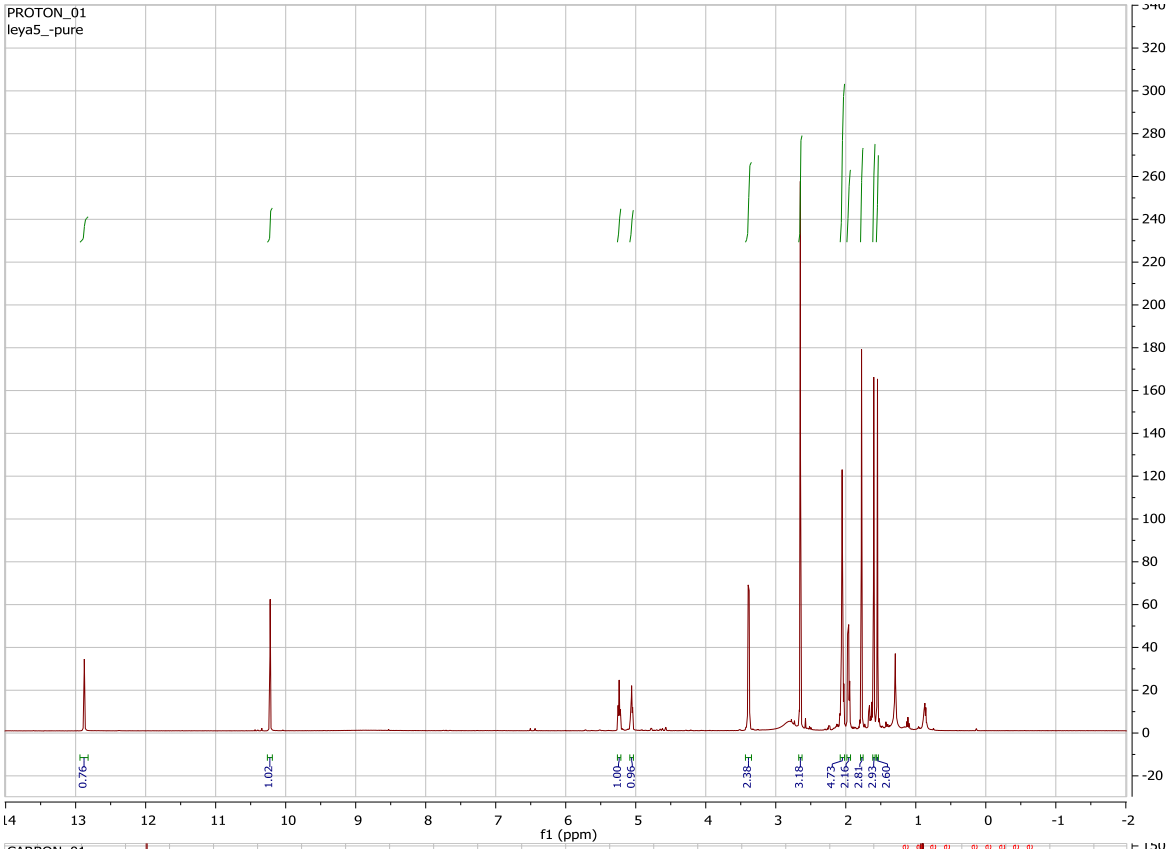

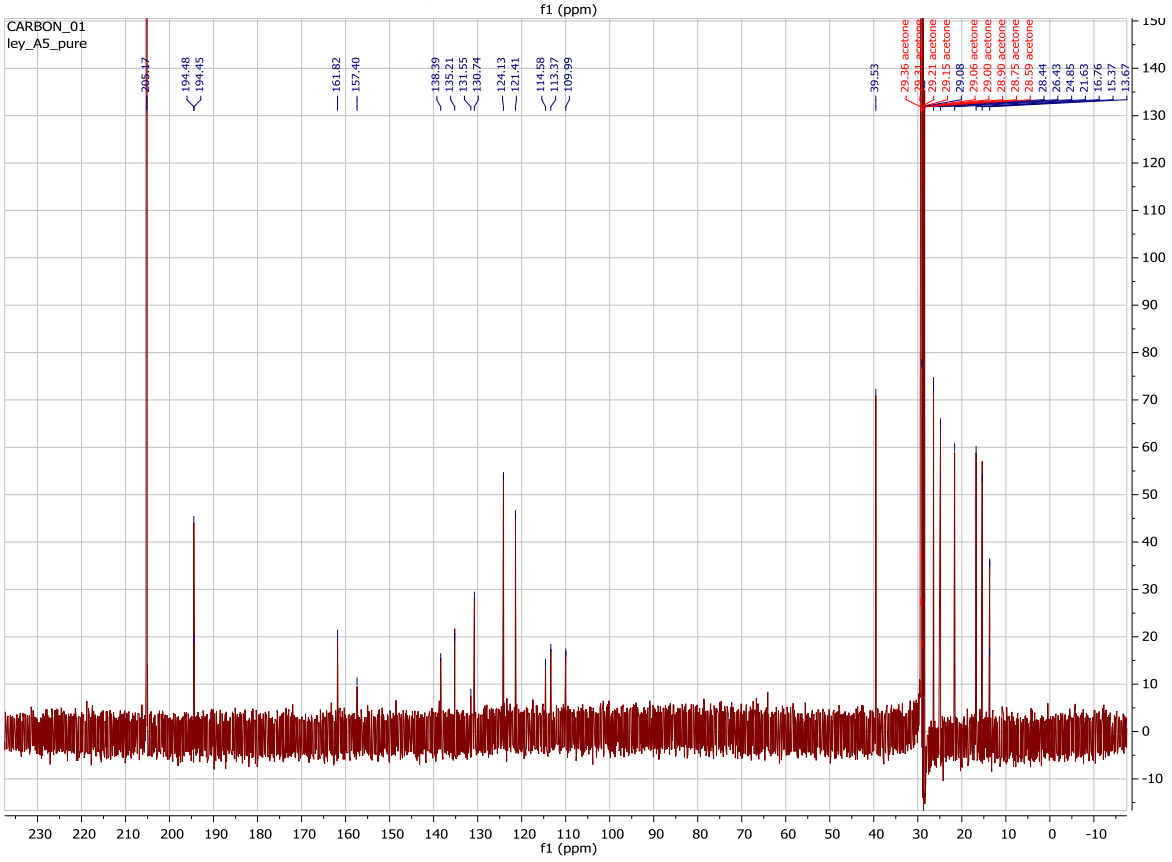

(E)-4-chloro-2-(3,7-dimethylocta-2,6-dienyl)-6-formyl-5-methyl-1,3-phenylene diacetate (Acetylated) (5)

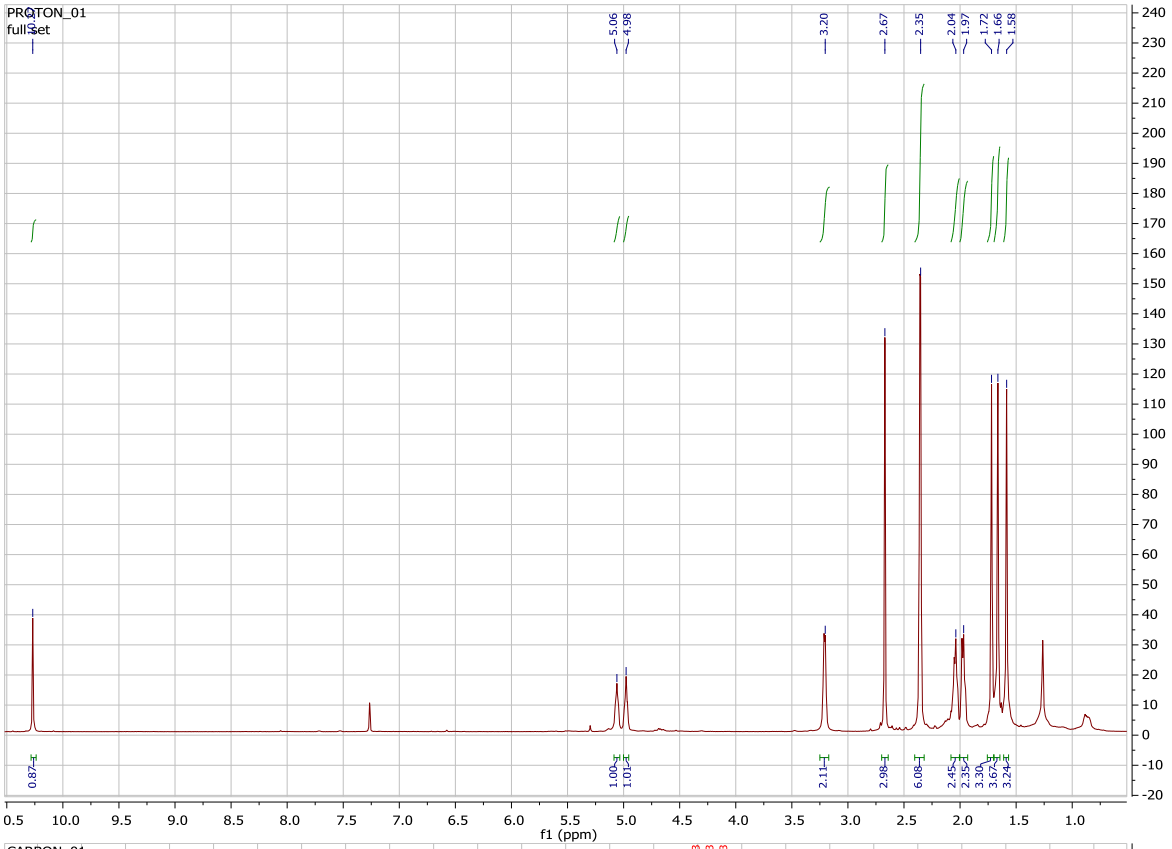

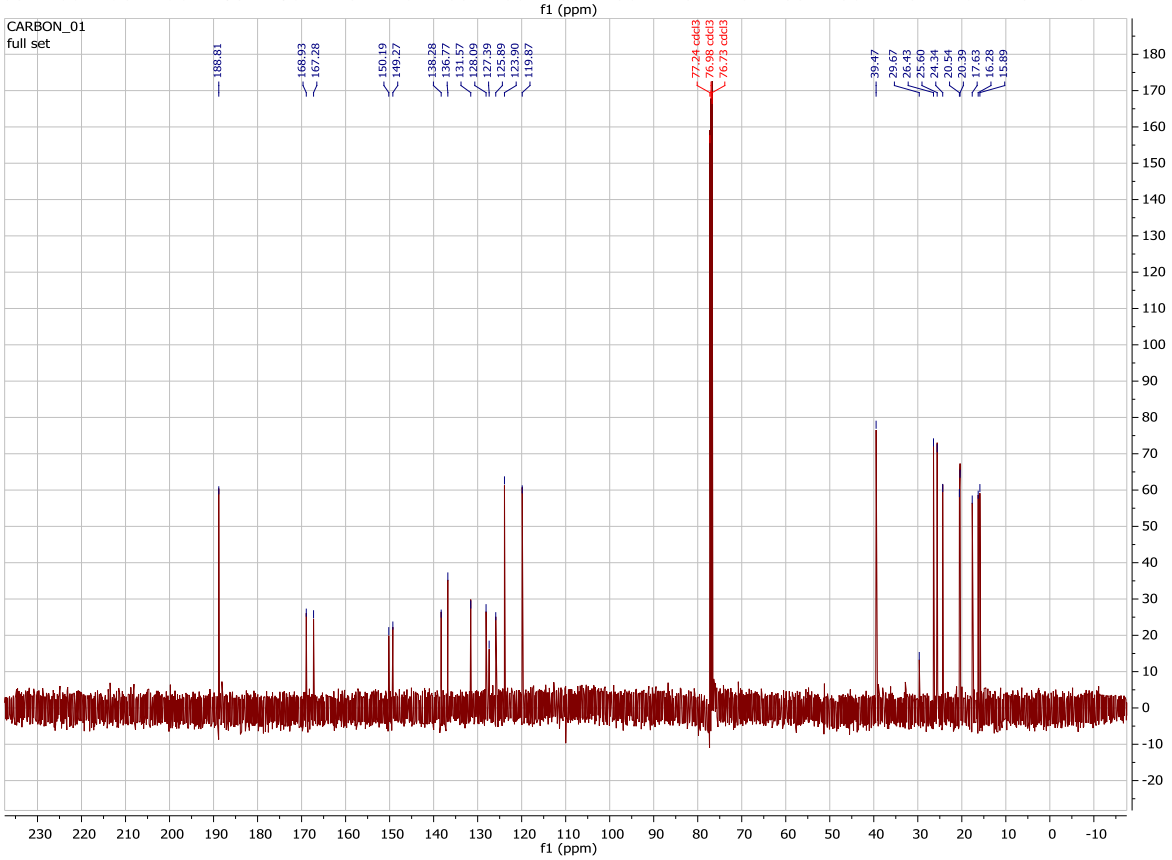

(E)-4-chloro-2-(3,7-dimethylocta-2,6-dienyl)-6-(hydroxymethyl)-5-methylbenzene-1,3-diol –reduced colletochlorin B (6)

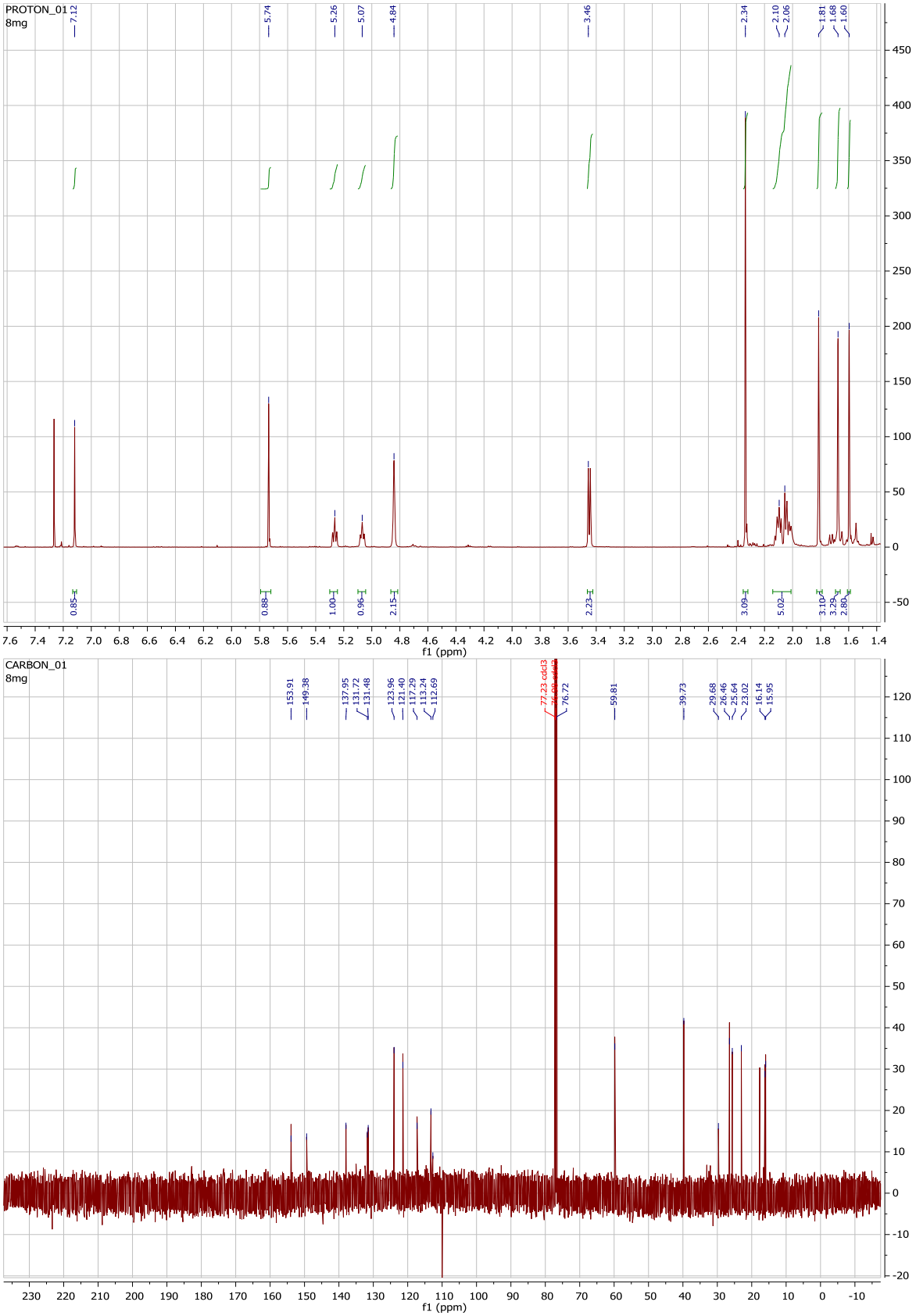

3-chloro-4,6-dimethoxy-2-methylbenzaldehyde (7)